Title
Design, Fabrication and Characterization of Thin Film Structures Through Oxidation Kinetics

Author
Diaz Leon, Juan Jose

Publication Date
2017

Peer reviewed|Thesis/dissertation

UNIVERSITY OF CALIFORNIA
SANTA CRUZ

DESIGN, FABRICATION AND CHARACTERIZATION OF THIN FILM STRUCTURES THROUGH OXIDATION KINETICS

A dissertation submitted in partial satisfaction
of the requirements for the degree of

DOCTOR OF PHILOSOPHY

in

ELECTRICAL ENGINEERING

by

Juan Jose Diaz Leon

June 2017

The Dissertation of Juan Jose Diaz Leon
is approved:

Professor Nobuhiko P. Kobayashi, Chair

Professor Joel Kubby

Dr. Andrew Phillips

_____
Tyrus Miller
Vice Provost and Dean of Graduate Studies

Table of Contents

List of Figures

List of Tables

Abstract

DESIGN, FABRICATION AND CHARACTERIZATION OF THIN FILM STRUCTURES THROUGH OXIDATION KINETICS

by

Juan Jose Diaz Leon

Materials science and engineering is devoted to the understanding of the physics and chemistry of materials at the mesoscale and to applying that knowledge into real-life applications. In this work, different oxide materials and different oxidation methods are studied from a materials science point of view and for specific applications. First, the deposition of complex metal oxides is explored for solar energy concentration. This requires a number of multi-cation oxide structures such as thin-film dielectric barriers, low loss waveguides or the use of continuously graded composition oxides for antireflection coatings and light concentration. Then, oxidation via Joule heating is used for the self-alignment of a selector on top of a memristor structure on a nanovia. Simulations are used to explore the necessary voltage for the insulator-to-metal transition temperature of NbO_2 using finite element analysis, followed by the fabrication and the characterization of such a device. Finally, long-term copper oxidation at room temperature and pressure is studied using optical techniques. Alternative characterization techniques are used to confirm the growth rate and phase change, and an application of copper oxide as a volatile conductive bridge is shown. All these examples show how the combination of novel simulation, fabrication and characterization techniques can be used to understand physical mechanisms and enable disruptive technologies in fields such as solar cells, light emitting diodes, photodetectors or memory devices.

To my family, and my friends – for all those that continuously help me pursue my dreams and overcome challenging times along the way.

To Alicia – thank you for all our conversations about science, research and life. You are the ultimate partner in scientific crime.

To nature – without countless hikes, runs, bike rides and surf sessions I would not be here today. I hope that we can all take care of it and enjoy it forever.

Acknowledgements

This PhD has been possible only partly because of myself. Many actors along the way have helped me thrive and learn to be humble, face problems and be able to solve them efficiently. My advisor, Prof. Nobuhiko P. Kobayashi, has constantly helped me think outside the box by giving me freedom while encouraging me to look at problems from a different point of view. Nobby has taught me how much ideas are worth, and what it takes to efficiently make research happen with a finite set of tools and knowledge. I was lucky enough to work with Prof. Joel Kubby on my master's thesis for a year before I started my PhD. Joel and Oscar Azucena in the adaptive optics lab showed me how to combine hands-on research and computational techniques. I have learned from Dr. Andrew Phillips how important it is to follow the scientific method and to keep a sincere interest in every piece of research that comes my way. I am lucky to have been able to publish research with Drew on the latter part of my PhD. I am grateful to have Nobby, Joel and Drew as my PhD defense committee.

During my PhD, I have collaborated with many scientists from whom I have learned more than I could imagine. During my two summer internships and my two year collaboration with Lawrence Livermore National Laboratory, I worked with Drs. Josh Kuntz, Tiziana Bond, Anna Hiszpanski and Eyal Feigenbaum on the design of optical structures for hierarchical arrays for antireflection coatings and on the development of subwavelength plasmonic structures for optoelectronics. From them, I learned the value of hard work and how a collaborative environment is paramount for the success of complex scientific endeavors. I have collaborated and learned from many other scientists. To name a few, Ernest Demaray from Demaray LLC, Robert Cormia from Foothill College, Michael Oye from NASA Ames, Stanley Williams from HP Labs or Sharka Prokes from NRL, Gary Tompa from SMI have all been collaborators in projects leading to journal publications and/or conference presentations.

I am especially grateful to all the NECTAR members I have been working with on a day-to-day basis. Dr. Junce Zhang and Dr. David Fryauf taught me how to work in a laboratory environment while being best friends. In the latter part of my PhD, David and I have maintained a close personal and professional relationship that has helped each other become better scientists while maintaining a fun life. Together, we have made so many mistakes that some of them turned out to be worth exploring.

1. Introduction

During my PhD at UC Santa Cruz, I have worked on different projects studying the photonic, electronic and optoelectronic properties of materials. Fluctuation of funding during my graduate years has allowed me to do research on different endeavors with a common denominator: materials for photonics, electronics and optoelectronics. In this thesis, I encompass my work related to oxidation kinetics, the study of different oxides and their evolution when exposed to physical and/or chemical changes. Thermodynamics of oxide and oxide structures have been largely studied, and supported with experimental verification.[1,2] The process of how these oxides evolve from phase to phase – oxidation kinetics – was first studied by Cabrera and Mott[3] but, to this day, they are still not fully understood.[1,4,5]. The introduction of numerical simulations along with the ever increasing computing power enables us today to study and predict oxidation kinetics, introducing a better way to study these phenomena and compare it with experimental results.[5,6] Furthermore, it is now being explored how to better use this phase evolution for device design; examples include nonlinear I-V devices such as memristors or volatile conductive bridges.[6,7] In this work, we explore several different novel oxide compounds for an array of applications.[8–11]. All this work has been published in journal publications and/or presented in conferences – please refer to the references throughout the manuscript.

In Chapter 2, we explore how to use multi-cation oxides for solar energy applications. This work was an ARPA-E funded project called “Sun to fibers” or S2F. The S2F project consisted of a passive device that would enable the concentration of solar light coming from a parabolic mirror into an optical fiber.[12] This ambitious project was focused on the design of an adaptive optical coupler (AOC) consisting of 5 different steps: (1) capturing light from a parabolic mirror, (2) an antireflection coating to (3) couple light with minimal loss into a (4) waveguide that would transport and (5) perform mode size conversion to

match the numerical aperture of an optical fiber, all with minimal loss. Steps (2) to (5) required design of optical structures in the wave optics range and the fabrication and characterization of optical materials that would present minimal loss for light coupling, transport and mode size conversion. Continuously graded antireflection coatings were developed with a refractive index starting at n=1.45 (silica, λ= 633 nm) and going all the way to n=2.3 using different profiles (linear or sine squared). Evanescent coupling was used to couple incoming light from the top surface of a waveguide into a coupled mode. Waveguides of different refractive indices (with n at the core varying from n~1.6 to n~2.1 at λ=633 nm) were deposited and characterized. Mode size conversion was designed using OptiBPM showing how when the refractive index in all 3-axis was continuously graded, conversion loss decreased drastically. Multiple research projects related to the S2F project[10–12] with an emphasis on materials engineering are presented in this chapter.

In Chapter 3, a complex selector-memristor structure is built using oxidation kinetics. Memristors, called the fourth two-terminal device, are passive electrical elements, able to retain different resistive values without any power applied to them. First theorized by Leon Chua in 1971[13] and demonstrated by Stanley Williams in HP Labs in 2008,[14] memristors are meant to revolutionize computing, by enabling fast, low-power memory storage and adaptive computational systems.[7,15] The memristors fabricated by Williams[14] are based on nanodevices where, depending on the voltage applied between their electrodes, the stoichiometry is modified achieving high- or low- current when a positive or negative voltage is applied. Once this stoichiometry is fixed, the resistive value is retained without having to maintain a voltage between the electrodes and can simply be probed indefinitely with a “read” voltage.[14] When multiple memristors are interconnected in a crossbar array, selecting a particular memristor becomes challenging due to sneak-path currents. [16–18] These sneak path currents are due to the linear I-V response of traditional memristive structures. Selectors are highly nonlinear I-V devices that can

mitigate sneak path currents, enabling the integration of memristors in a crossbar array. However, the addition of yet another device in a crossbar array adds complexity to the structure. In this project, niobium was deposited on a tantalum oxide memristor. Through COMSOL simulations, it was envisioned that Joule heating (increasing the temperature of a structure by flowing electrical current through it) could be used to build a niobium oxide selector on top of an existing memristor structure without further fabrication steps. The device was then fabricated and characterized, confirming the ability of electrothermal heating and oxidation kinetics as drivers for the development of new devices.[9,19]

In Chapter 4, the oxidation of copper at room temperature and standard pressure in an ambient environment is studied. Copper oxide is one of the most studied metal oxides.[20] It can be beneficial (copper oxide is used for solar cells, gas sensors or as a catalyst[21,22]) or problematic, hindering the conductivity of copper metal. At room temperature and pressure, copper develops into two stable phases: Cu_2O (cuprous oxide) and CuO (cupric oxide). Interestingly, copper oxide growth is an ionic process, where copper cations tunnel through oxygen vacancies to the surface of the existing oxide. Cabrera and Mott[3] showed an inverse-logarithmic growth rate for copper oxide at room temperature. Keeping track of oxide thickness and composition over time is complicated, due to the thin nature of this oxide (<10 nm) and the slow growth it presents after the initial thickness (months).[8,23] In this work, we show how reflectometry-ellipsometry (RE) can be used to measure growth rate and phase composition of copper oxide over time.[8] RE is a simple optical technique that requires no vacuum and can be done over large areas. Using RE, two different thin-film copper samples are analyzed over the course of 253 days. Results are confirmed with other standard thin film measurement techniques such as x-ray photoelectron spectroscopy (XPS). Atomic force microscopy (AFM) and x-ray diffraction (XRD) are also used to further investigate the interdependence between

initial copper roughness and crystalline grain size with growth rate and composition (Cu_2O and CuO content over time) of the resulting oxide layer.

Other work during my PhD but unrelated to oxide kinetics includes nanowires for thermoelectrics,[24] hierarchical antireflection coatings based on moth-eye structures,[25] subwavelength transparent conductive nanolattices for optoelectronics and corrosion protection of astronomical mirror coatings.[26]

1.1 References

(1) Seybolt, A. U. Oxidation of metals. *Adv. Phys.* **1963**, *12* (45), 1–43 DOI: 10.1080/00018736300101253.

(2) Darken, L. S.; Gurry, R. W. The system iron-oxygen. II. Equilibrium and thermodynamics of liquid oxide and other phases. *J. Am. Chem. Soc.* **1946**, *68* (1), 798–819 DOI: 10.1021/ja01209a030.

(3) Cabrera, N.; Mott, N. F. Theory of the oxidation of metals. *Reports Prog. Phys.* **1949**, *12* (1), 163 DOI: 10.1017/CBO9781107415324.004.

(4) Ghez, R. On the Mott-Cabrera oxidation rate equation and the inverse-logarithmic law. *J. Chem. Phys.* **1973**, *58* (5), 1838 DOI: 10.1063/1.1679440.

(5) Genreith-Schriever, A. R.; De Souza, R. A. Field-enhanced ion transport in solids: Reexamination with molecular dynamics simulations. *Phys. Rev. B* **2016**, *94* (22), 224304 DOI: 10.1103/PhysRevB.94.224304.

(6) Waser, R.; Dittmann, R.; Staikov, C.; Szot, K. Redox-based resistive switching memories nanoionic mechanisms, prospects, and challenges. *Adv. Mater.* **2009**, *21* (25–26), 2632–2663 DOI: 10.1002/adma.200900375.

(7) Ha, S. D.; Ramanathan, S. Adaptive oxide electronics: A review. *J. Appl. Phys.* **2011**, *110* (7) DOI: 10.1063/1.3640806.

(8) Diaz Leon, J. J.; Fryauf, D. M.; Cormia, R. D.; Zhang, M. X. M.; Samuels, K.; Williams, R. S.; Kobayashi, N. P. Reflectometry-Ellipsometry Reveals Thickness, Growth Rate, and Phase Composition in Oxidation of Copper. *ACS Appl. Mater. Interfaces* **2016**, *8* (34), 22337–22344 DOI: 10.1021/acsami.6b06626.

(9) Díaz León, J. J.; Norris, K. J.; Sevic, J. F.; Kobayashi, N. P. Integration of a niobium oxide selector on a tantalum oxide memristor by local oxidation using Joule heating. *Proc. SPIE* **2016**, *9924* DOI: 10.1117/12.2239609.

(10) Diaz Leon, J. J.; Garrett, M. P.; Fryauf, D. M.; Zhang, J.; Norris, K. J.; Prokes, S. M.; Kobayashi, N. P. Transparent, high refractive index oxides: Control of the nanostructure of titanium hafnium oxide alloys by variation of the ion energy during reactive magnetron sputtering deposition. *MRS Online Proc. Libr. Arch.* **2015**, *1805*.

(11) Diaz Leon, J. J.; Garrett, M. P.; Zhang, J.; Kobayashi, N. P. Aluminum titanium oxide alloys : Deposition of amorphous , transparent , corrosion-resistant films by pulsed DC reactive magnetron sputtering with RF substrate bias. *Mater. Sci. Semicond. Process.* **2015**, *36*, 96–102 DOI: 10.1016/j.mssp.2015.03.039.

(12) Díaz León, J. J.; Garrett, M. P.; Zhang, J.; Han, K.; Demaray, R. E.; Anderson, R. W.; Lewandowski, A.; Bottenberg, W.; Kobayashi, N. P. Sun to fibers (S2F): massively scalable collection and transmission of concentrated solar light for efficient energy conversion and storage ; 2014; Vol. 9175, p 91750A–91750A–9.

(13) Chua, L. O. Memristor—The Missing Circuit Element. *IEEE Trans. Circuit Theory* **1971**, *18* (5), 507–519.

(14) Strukov, D. B.; Snider, G. S.; Stewart, D. R.; Williams, R. S. The missing memristor found. *Nature* **2008**, *453* (May), 80–83 DOI: 10.1038/nature08166.

(15) Yang, J. J.; Strukov, D. B.; Stewart, D. R. Memristive devices for computing. *Nat. Nanotechnol.* **2013**, *8* (1), 13–24 DOI: 10.1038/nnano.2012.240.

(16) Joshua Yang, J.; Zhang, M. X.; Pickett, M. D.; Miao, F.; Paul Strachan, J.; Li, W. Di; Yi, W.; Ohlberg, D. A. A.; Joon Choi, B.; Wu, W.; et al. Engineering nonlinearity into memristors for passive crossbar applications. *Appl. Phys. Lett.* **2012**, *100* (11), 98–102 DOI: 10.1063/1.3693392.

(17) Burr, G. W.; Shenoy, R. S.; Virwani, K.; Narayanan, P.; Padilla, A. Access devices for 3D crosspoint memory. *J. Vac. Sci. Technol. B* **2014**, *32* (4), 40802-1–23 DOI: 10.1116/1.4889999.

(18) Linn, E.; Rosezin, R.; Kügeler, C.; Waser, R. Complementary resistive switches for passive nanocrossbar memories. *Nat. Mater.* **2010**, *9* (5), 403–406 DOI: 10.1038/nmat2748.

(19) Diaz Leon, J. J.; Norris, K. J.; Yang, J. J.; Sevic, J. F.; Kobayashi, N. P. A niobium oxide-tantalum oxide selector-memristor self-aligned nanostack. *Appl. Phys. Lett.* **2017**, *110* (10), 103102 DOI: 10.1063/1.4977945.

(20) Gattinoni, C.; Michaelides, A. Atomistic details of oxide surfaces and surface oxidation: the example of copper and its oxides. *Surf. Sci. Rep.* **2015**, *70* (3), 424–447 DOI: 10.1016/j.surfrep.2015.07.001.

(21) Zoolfakar, A. S.; Rani, R. A.; Morfa, A. J.; O'Mullane, A. P.; Kalantar-zadeh, K. Nanostructured copper oxide semiconductors: a perspective on materials, synthesis methods and applications. *J. Mater. Chem. C* **2014**, *2* (27), 5247 DOI: 10.1039/c4tc00345d.

(22) Prasad, R.; Singh, P. A novel route of single step reactive calcination of copper salts far below their decomposition temperatures for synthesis of highly active catalysts. *Catal. Sci. Technol.* **2013**, No. 1, 3326–3334 DOI: 10.1039/C3CY00626C.

(23) Platzman, I.; Brener, R.; Haick, H.; Tannenbaum, R. Oxidation of Polycrystalline Copper Thin Films at Ambient Conditions. *J. Phys. Chem. C* **2008**, *112* (4), 1101–1108 DOI: 10.1021/jp076981k.

(24) Diaz Leon, J. J.; Norris, K. J.; Hartnett, R. J.; Garrett, M. P.; Tompa, G. S.; Kobayashi, N. Nonlinear current–voltage characteristics based on semiconductor nanowire networks enable a new concept in thermoelectric device optimization. *Appl. Phys. A* **2016**, *128* (8), 1–9.

(25) Diaz Leon, J. J.; Hiszpanski, A. M.; Bond, T. C.; Kuntz, J. D. Design Rules for Tailoring Antireflection Properties of Hierarchical Optical Structures. *Adv. Opt. Mater.* **2017**, *1700080*, 1700080 DOI: 10.1002/adom.201700080.

(26) Fryauf, D. M.; Diaz Leon, J. J.; Phillips, A. C.; Kobayashi, N. P. Silver Film Surface Modification by Ion Bombardment Decreases Surface Plasmon Resonance Absorption. *ACS Appl. Mater. Interfaces* **2017**, acsami.7b01603 DOI: 10.1021/acsami.7b01603.

2. Multi-cation oxides for solar energy applications

In this chapter, different thin film structures will be shown for a common purpose, the fabrication of a novel device for solar energy concentration, called the sun to fiber optical coupler (S2F). First, an overview of the project will be given, followed by several examples of multi-cation oxides fabricated and studied for this purpose.

2.1 Sun to Fibers (S2F): Massively Scalable Collection and Transmission of Concentrated Solar Light for Efficient Energy Conversion and Storage

2.1.1 Abstract

Concentrated solar energy has proven to be an efficient approach for both solar thermal energy applications and photovoltaics. Here, we propose a passive optical device, the Adiabatic Optical Coupler (AOC), that efficiently couples concentrated solar light from a primary solar concentrator into an optical fiber, enabling light collection and energy conversion/storage to be geographically separated, thus maximizing the overall system efficiency. The AOC offers secondary concentration of concentrated solar light through an adiabatic optical mode conversion process. Solar light, highly focused by this two stage concentrator, is delivered by optical fiber to either be subsequently converted to electricity or thermally stored. The ability to transport high energy light flux eliminates the need for high temperature working fluids in solar-thermal systems. In order to design the AOC and related peripherals, we used various modeling tools to cover different optical regimes at macroscopic and microscopic scales. We demonstrated a set of optical thin films with spatially varied refractive index up to 3 and negligible optical absorption by using a proprietary sputtering technique to fabricate the AOC. We further studied the films using experimental measurements and theoretical analysis to optimize their optical

properties. Preliminary cost analysis suggests that solar thermal power generation systems that employ our S2F concept could offer the cost and efficiency required to achieve the 2020 SunShot initiative levelized cost of electricity (LCOE) target. Success of this endeavor could change the energy conversion paradigm, and allow massively scalable concentrated solar energy utilization.

2.1.2 Introduction

Solar energy is a free and virtually endless power source. There have been many different approaches to harnessing the sun's energy and converting it into electricity, heat or chemical fuel[1,2]. The Sunshot Vision Study from 2012 envisions a reduction of 75% in the price of solar technologies between 2010 and 2020 to be able to produce 14% of the U.S. electricity demand by 2030 and 27% by 2050[3].

Photovoltaics (PV) – Figure 2-1a - is a mature technology, but several limitations have made the renewable energies world look for different solutions, such as thermoelectrics or concentrated solar power (CSP)[2]. CSP (Figure 2-1b) has been used since the early 1900's to generate steam, but not for electricity generation purposes in the United States until the early 1980's[4,5]. Nevertheless, CSP has proven to be efficient for utility-scale sunlight collection, as we can see on the several different setups deployed both overseas and in the U.S.A.

The price for PV has fallen dramatically since it was deployed. However, it cannot accommodate for the grid peak use, nor provide energy when the sun is not shining, unless intermediate electrical energy storage is designed at the electrical grid level. Additionally, PV produces DC electricity, so it needs to be transformed to AC to be tied into the grid. In contrast, CSP can provide energy for more hours per day due to its ability to store energy as heat. However, most of the CSP systems are not scalable. Water cooling is an issue, so dry or hybrid cooling must be enabled for this technology to

succeed. Furthermore, land area is another factor to take into account both in PV and CSP[3] .

Some other solutions have been implemented with little success. Stirling engines (Figure 2-1c), for example, can be mounted into a solar dish with great conversion efficiency. However, this system is incompatible with thermal storage, and has a high cost, making it a weak alternative to PV[5].

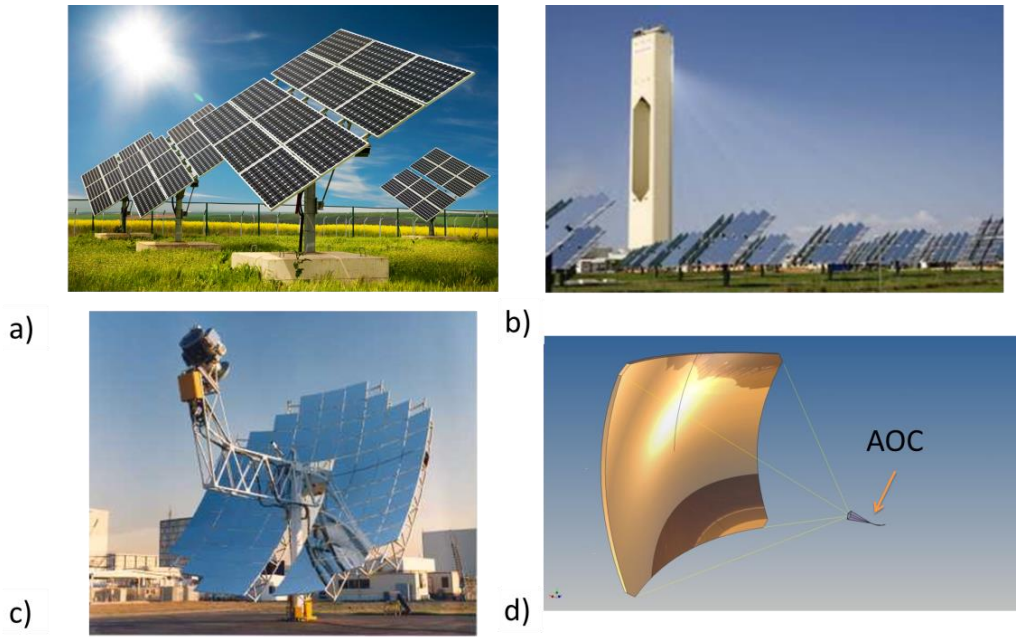

Figure 2-1. a) Photovoltaic cells, Arameh Solar b) PS10 solar thermal power plant, Abengoa c) Stirling engine, Planta Solar de Almeria (PSA) d) Adiabatic Optical Coupler (AOC).

By splitting collection, transmission and conversion of optical light into three different building blocks, we can then optimize all of them separately, increasing the overall efficiency of the system. Here, we focus on the collection and secondary concentration of concentrated sunlight from a parabolic mirror and the coupling of that light into an optical fiber, for transmission to a final conversion or storage. If we were able to eliminate the mismatch in etendue that exists between the light from a concentrating parabolic mirror

(high numerical aperture, NA) and the optical fiber (low NA), we would then be able to efficiently transmit the light through an optical fiber, with no intermediate losses associated with energy conversion, but only with the loss associated with the fiber transport (Figure 2-1d). In other words, we would capture light and deliver light with high energy at the end of the system while maintaining low working temperature.

Our approach for solar energy conversion is a device called the Adiabatic Optical Coupler (AOC). The purpose of the AOC is to efficiently guide sunlight into an optical fiber, for use away from the point of collection. If all the necessary conditions are met, the AOC will be able to provide 90% efficient coupling of the incoming sunlight from a parabolic mirror into a low NA optical fiber. The rest of the energy will be reflected back, lost due to mode size conversion, scattered inside the thin film structure or absorbed by the films. For this, we rely on the unique deposition capabilities of binary and ternary metal oxides that have continuous variation on the refractive index both axially and laterally.

2.1.3 The adiabatic optical coupler (AOC)

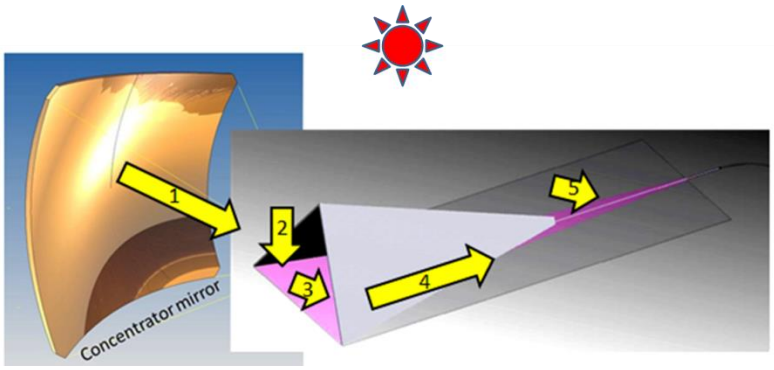

Figure 2-2. Five-step coupling in the AOC.

The design of the AOC is based on five different steps that are covered in this section: 1) Light coming from a parabolic mirror is captured into 2) a broadband, wide angle

antireflection coating, which will then carry the incoming concentrated light to 3) couple it to a waveguide, which will 4) transport the light along the film to finally 5) perform mode size conversion (MSC) of the incoming concentrated light, and deliver it to the optical fiber with minimum loss. Figure 2-2 shows a schematic of the system.

2.1.3.1 Efficient capture of broadband, wide angle light from a parabolic mirror

The first step of the AOC is to capture the concentrated light from the parabolic mirror efficiently. Consequently, a so-called “dog house” was designed, composed of a waveguide structure with an antireflective coating that will utilize all the light, and two mirrors in a triangular fashion on top to help direct all the rays into the waveguide. A 3D model is shown in Figure 2-3a.

The distribution of the angles impinging the waveguide is a matter of special importance to maximize the efficiency of the coupler. SolTrace[6] was used to calculate the spatial distribution flux of light in the structure. Figure 2-3b shows the normalized angular distribution of the angles hitting the waveguide including multiple reflections within the system. Over 90% of the incoming rays are in the 0-70 degree range (from the normal). Figure 2-3c represents the absorbed flux intensity of the internal faces of the mirrors and the waveguide surface of the AOC. These results imply that 0-70 degree angle with high flux intensity will hit the waveguide surface - the antireflective coating - to be subsequently coupled into the waveguide. An antireflective coating that maximizes this range is described next.

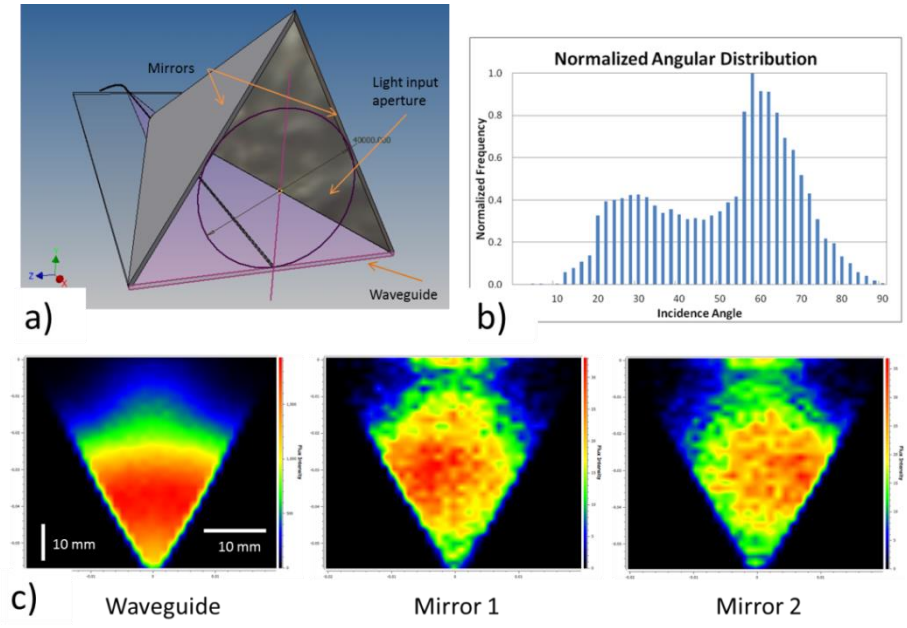

Figure 2-3. Step 1 – Capture sunlight from the parabolic mirror. a) AOC 3D model b) Normalized angular distribution from normal after one bounce c) Flux intensity of the internal faces of the waveguide and mirrors inside the AOC.

2.1.3.2 Antireflective coating (ARC)

In order to accommodate for variable-angle and a wide range of wavelengths impinging the AOC from the concentrator mirror, it was necessary to design an antireflective coating to get most of the incident light into the waveguide. Graded index antireflective coatings have been studied for a long time[7–9], but achieving a deposition technique with enough uniformity and resolution has been a major obstacle preventing their implementation. Sputtering, used with conditions that will be discussed later, has the ability to deposit a continuously graded index profile with a wide refractive range and low optical attenuation.

Graded index theory requires complex computer-aided solvers, because of the special boundary conditions that arise in these films. The Transfer Matrix Method (TMM) is a good approach for 1D graded index systems[7]. Simulation of a sine to the fourth profile with a refractive index starting at 1.38 and going up to 2, to match the substrate, was performed using TMM. Figure 2-4a shows the refractive index profile of the structure.

Figure 2-4b shows the very low reflectivity for 400-1200 nm light in the 0-60 degree angle range.

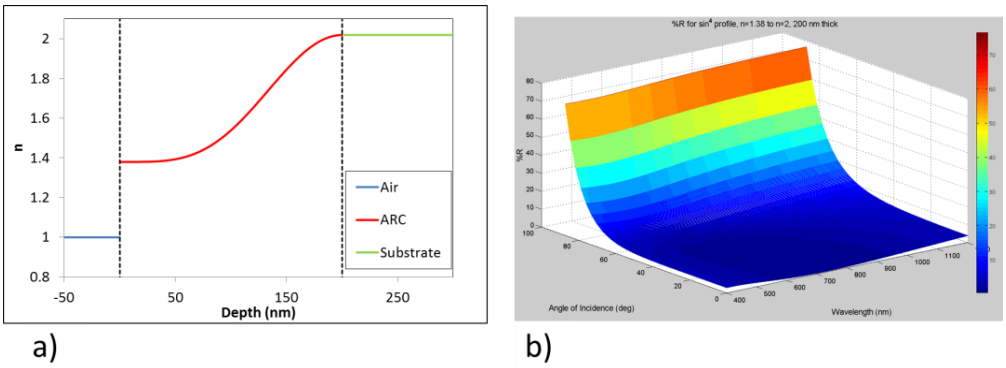

Figure 2-4. Step 2 – Antireflective coating. a) ARC going from 1.38 to 2 from air, b) Reflectivity over angle of incidence for this given setup.

2.1.3.3 ARC to waveguide coupling

Light coming from an ARC deposited on a waveguide needs to be coupled into the bound modes of the waveguide. To do this, an intermediate step is required to avoid light from coming back out from the ARC. Evanescent coupling is an example of one of such techniques[10] (Figure 2-5). Evanescent coupling uses a high refractive index material, separated from the lower-index waveguide by a sub-wavelength spacing layer. When phase-matching conditions are met between the evanescent mode of light inside the high-index material and the propagation vector of the allowed waveguide mode, light couples into the waveguide.

Figure 2-5a is a COMSOL simulation of evanescent prism coupling at a wavelength of 500 nm. A 45 degree high index prism (n=2.6) is used to couple light impinging the lateral facet, as shown in the figure, into the asymmetric slab waveguide underneath (n=2.2). Air (n=1) is used as the upper medium while glass (n=1.52) is used as the substrate material. An optional 100 nm index matching fluid (n=1.5) is used in between the prism and the waveguide to improve evanescent coupling efficiency. On Figure 2-5b a real

evanescent prism coupling setup is shown using a titanium dioxide rutile prism (n=2.67) coupling green laser light (n=532 nm) into an aluminum oxide (n=1.66) waveguide on a fused silica substrate (n=1.52). Light internally reflecting from the prism-film interface creates an evanescent wave, which couples into the waveguide, traveling all the way to the edge.

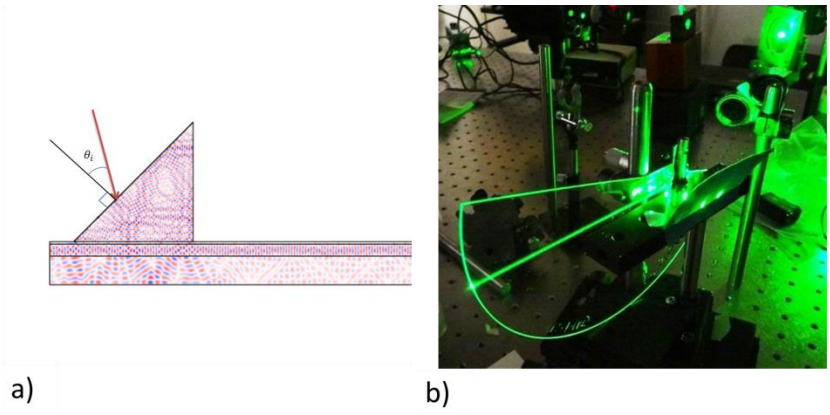

Figure 2-5. Step 3 – a) COMSOL simulation of evanescent prism coupling b) Evanescent coupling setup

2.1.3.4 Waveguide transmission of concentrated light

Once the light is coupled in the waveguide, it needs to propagate laterally. A material with high refractive index is necessary to increase optical confinement, but also needs to retain low optical attenuation (minimum absorption and scattering) to minimize loss. Compounding the complexity, these properties may vary as a function of the wavelengths under consideration (400-1000 nm). We have developed several metal oxide films with a refractive index close to 2 and we are aiming to achieve optical absorption in the $k = 10^{-7} - 10^{-8}$ range over the entire solar spectrum. That would mean $1 - 0.1\ dB/cm$ of absorptance, respectively, according to the Beer-Lambert law. We have deposited such low loss films (measured vertically with ellipsometry), and are now designing a lateral in-film loss measurement setup that will directly show optical attenuation as light propagates through the film. We have deposited several films with different refractive indices and

thicknesses, and measured the number of modes that are accommodated for every wavelength. Figure 2-6a is a simulation of a waveguide with n = 2.1, using air above and thermal silicon oxide below as low index mediums. As the thickness increases, more modes can be fit for a given waveguide. In the figure, a thickness of 1.81 um is marked using a black marker. That combination of refractive index and thickness would fit approximately 10 transverse electric (TE) modes. Figure 2-6b is a study using evanescent prism coupling of a similar structure deposited using pulsed DC magnetron sputtering with RF substrate bias. Every local minimum in the graph represents a mode coupled into the waveguide. There are 10 minimums as well, at different angles, as expected by the mode simulation calculation. The wavelength was 532 nm in both cases. The width of this waveguide will slowly taper to quasi-adiabatically concentrate the light down to the optical fiber width. In the last section of the AOC, the refractive index also changes spatially (in all x, y and z axes) enabling more adiabatic concentration as compared to just tapering the width physically.

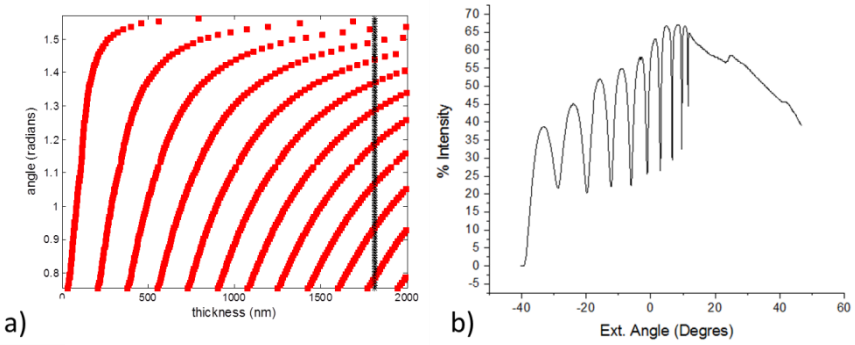

Figure 2-6. Step 4 – Waveguide transmission. a) TE modes propagating along a waveguide made of hafnia (n=2.1) for a given thickness. The marker is at 1.81 um. Upper cladding is air (n~1), lower cladding is thermal oxide (n=1.44) b) Prism coupling characterization of the mode structure of the same waveguide structure. Wavelength is 532 nm at both cases

2.1.3.5 Mode size conversion and optical fiber coupling

The light available in the waveguide must change dimensions from the aperture (several tens of centimeters) down to 300 um, the expected diameter of the optical fiber (Figure 2-

7a). This mode size conversion can be done in different ways[11–13]. The last section of the AOC will have the refractive index changing in all directions. OptiBPM was used to design and simulate the waveguide transmission and mode conversion section (Figure 2-7b). Table 2-1 is a comparison between different refractive index profiles in the mode conversion section (Figure 2-7b). The refractive index was changed from n=1.46 (at the center of the structure in x and y) to n=1.443 (at the edges). The efficiency was calculated measuring the power at the output of the mode conversion section every 100 nm for single modes in the 400-1000 nm range. 3 scenarios are shown in Table 2-1: In scenario 1, the refractive index is kept constant at n=1.46 along the structure, and the coupling efficiency is only 8%. In scenario 2, the refractive index is changed linearly along x from n=1.46 down to n=1.443 at the edge. The refractive index in the y axis is kept constant with thickness. Here, the efficiency went up to 50%. In scenario 3, the refractive index is graded linearly both in the x and y axis, with the maximum at the center of the structure, down to n=1.43 at the edges. The efficiency increased to an average of 96% for wavelengths between 400 and 1000 nm. Preliminary results show that changing the refractive index along x and y axes vary the efficiency of the coupler dramatically, indicating that more efficient concentration can be achieved if the refractive index is changed along x and y. The z axis indicates propagation direction and there is no variation of refractive index along z in this study. It is hypothesized that a graded refractive index will improve conversion efficiency by reducing reflections due to sharp refractive index changes at the edge of the structure, and by allowing the light to be focused at the center of the waveguide structure.

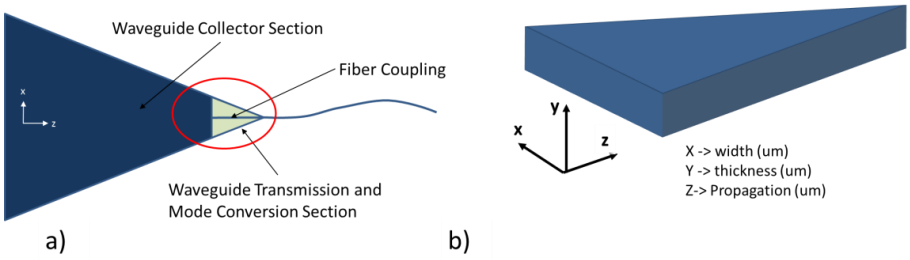

Figure 2-7. Step 5 – Schematic of the mode size conversion section. a)Top view of the waveguide structure in the AOC b) 3D model of the section circled in red in a).

Table 2-1. Comparison of different efficiencies for single modes between 400-1000 nm in the mode conversion section when the refractive index changes linearly.

Scenario	Graded index in x	Graded index in y	Efficiency (400-1000 nm)
1	No	No	8%
2	Linear	No	50%
3	Linear	Linear	96%

2.1.3.6 Cost analysis

Coupler cost was estimated to be $1,500 each for a 25kW capable coupler with an admission aperture of 20cm diameter, necessary to intercept 95% of the rays of a 25 m^2 parabolic tracking dish with a 2 mrad slope error surface. More than half the cost for couplers is due to fabrication with fused silica substrates. The cost of a smaller S2FC for a smaller diameter mirror is estimated to be proportional to the entrance aperture in ration to the 25kW case. Performance of the films for the AR and waveguide coating were estimated to have a loss of up to -1 dB, however much or most of this loss is estimated to be optical. This would allow glass or perhaps plastic substrate to be used, leading to lower device direct cost. Fig 8 shows a comparison between a power tower system and the S2F coupler for a 115 MW solar power plant using the NREL Service Advisory Model (SAM)[14].

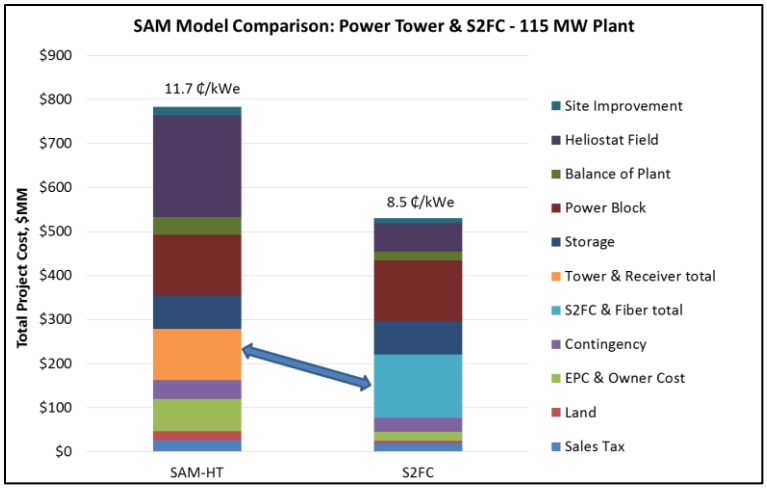

Figure 2-8. Cost analysis of an S2F solar plant compared to a power tower performed with the System Advisor Model (SAM)

2.1.4 Pulsed DC reactive magnetron sputtering with substrate bias

It has been previously shown that amorphous materials are suitable for optical applications[15]. We are able to deposit dense, amorphous, low absorption and low scattering metal oxide alloys with tunable refractive index: the enabling technology for this is a pulsed DC reactive magnetron sputtering system with RF substrate bias. By controlling the power applied to the different sputtering materials, we can reactively co-sputter multiple targets at the same time, to grow binary or ternary oxides or fluorides. This setup gives us fine control of the refractive index in a wide range, starting at values as low as n=1.38 (magnesium fluoride) and going up to titanium oxide (n=2.9 at 532 nm), all the while keeping the optical attenuation (k) below 10^{-5}.

Metal oxides deposited by reactive sputtering tend to yield a columnar microstructure, increasing its optical attenuation. However, by using ion-assisted techniques, fully amorphous films can be grown. We applied a pulsed DC bias across metallic targets, depositing oxides. Simultaneously, an RF bias was applied across the substrate, densifying the films, eliminating the columnar morphology, and increasing the overall

optical qualities of the film. Figure 9a is a picture of the sputtering system we use to deposit low k waveguides. In figure 9b, Transmission Electron Microscopy (TEM) images of a titanium hafnium oxide alloy ($TiHf_xO_y$) are shown with and without substrate bias. There is a clear difference in the nanostructure of the films when using RF bias on the substrate. Figure 9c shows the refractive index of different aluminum titanium oxide alloys in the 230-930 nm range. The refractive index is raised by increasing the ratio of titanium cations present in the films. Therefore, by varying the power applied to the targets during deposition, it is possible to create continuously graded index profiles, useful for applications such as antireflective coatings[16].

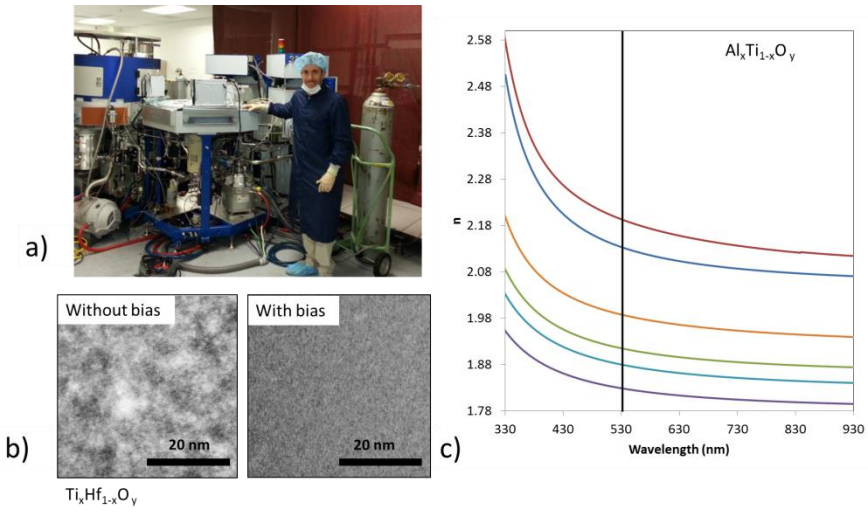

Figure 2-9. a) Sputtering system available at Tango Systems b) TEM images of titanium hafnium oxide with and without bias c) Dispersion data of the refractive index of different aluminum titanium oxide alloys with different cation atomic ratios.

2.1.5 Conclusions

The Adiabatic Optical Coupler (AOC) was designed to achieve secondary concentration of concentrated sunlight into an optical fiber. Modeling shows that it is feasible to achieve 90% efficiency. Cost analysis suggests that the LCOE could be less than a power tower in a solar thermal setup. Metal oxide films with tunable index and low optical attenuation have been deposited, creating continuously graded refractive index profiles and low loss

waveguides. All 5 steps of the AOC have been studied. However, the construction of the device and the synergy of these 5 working parts must be put together in a real device. Completion of this project could change the solar energy conversion paradigm and also enable new technologies such as daylighting or solid state lighting.

2.2 Transparent, high refractive index oxides: Control of the nanostructure of titanium hafnium oxide alloys by variation of the ion energy during reactive magnetron sputtering deposition

2.2.1 Abstract

A range of optical and optoelectronic applications would benefit from high refractive index (*n*), dense and transparent films that guide, concentrate and couple light. However, materials with high *n* usually have a high optical extinction coefficient (κ) which keeps these materials from being suitable for optical components that require long optical paths. We studied titanium hafnium oxide alloy films to obtain high refractive index (*n*>2) with minimum optical extinction coefficients ($\kappa < 10^{-5}$) over the visible and near IR spectrum (380-930 nm). Titanium hafnium oxide alloys were deposited using pulsed DC reactive magnetron sputtering with and without RF substrate bias on silicon dioxide. For a given deposition condition intended for a specific titanium/hafnium molar fraction ratio, the ion energy of deposition species was explicitly controlled by varying the RF substrate bias. Spectroscopic ellipsometry, transmission electron microscopy, energy dispersive x-ray spectroscopy and atomic force microscopy were used to characterize the films. It appears that applying RF substrate bias reduces the nanocrystalline size, changes the surface morphology and increases the refractive index while maintaining comparable titanium/hafnium cation molar fraction. Precise control of the nanostructure of ternary metal oxides can alter their macroscopic properties, resulting in improved optical films.

2.2.2 Introduction

The addition of cations to binary oxides to form ternary and quaternary metal oxides provides flexibility in designing material properties, providing opportunities to optimize material properties exclusive to each other in binaries such as transparency, electrical

conductivity or corrosion resistance [17–19]. A large library of ternary metal oxides has been studied for different applications. For example, aluminum zinc oxide (AZO) and indium tin oxide (ITO) are used as transparent conductive oxides [17,20]. Aluminum titanium oxide films have been studied as novel transparent corrosion barriers [18]. Titanium hafnium oxide alloys have been studied as gate insulators due to their high dielectric constant, low leakage current and good thermal stability [21–24]. Titanium hafnium oxide alloys are also interesting because of their large bandgap and low absorption in the visible spectrum [25]. In our previous study, we compared a number of titanium hafnium oxide alloys with different cation molar fractions [26]. In this paper, we focus on a single cation molar fraction, and study the dependence of microscturcture and optical properties of films on the ion energy controlled by RF substrate bias during sputtering.

High quality optical films require stringent control on their optical and mechanical properties, such as hardness, flexibility, high refractive index and low optical absorption[15]. Optical films with high index (n) and low extinction coefficient (κ) could enable a number of new technologies in such applications as optical concentration and transmission of sunlight. High index optical waveguides could be then created to transport light with minimum loss and increase the number of guided modes for a given thickness and cladding materials. Moreover, by continuously changing the composition of a film, graded refractive index coatings could be deposited to maximize in- and out-coupling of optical devices by minimizing the reflection produced by refractive index mismatch present between the active layer and the surrounding layers, such as the anode or the glass substrate.

Selection and control of a film deposition process has proven to be critical in order to create high quality optical films. A number of chemical and physical vapor deposition techniques have been explored; for instance, studies using ion beam assisted deposition (IBAD) and plasma-enhanced chemical vapor deposition (PECVD) suggested that using

high ion-to-neutral-flux ratio and controlling the ion energy are critical for optical films [15,16]. Hence, it is necessary to use a deposition technique that not only provides a high ion-to-neutral flux ratio at the substrate surface but also controls the energy of the ions impinging the substrate. A physical vapor deposition technique (PVD), reactive sputtering, was used. A pulsed DC power supply and a scanning magnetron were used to increase ion-to-neutral flux ratio and an additional RF power supply was used in the substrate to control the ion energy, resulting in high quality optical films.

2.2.3 Experiment

In this study, we used a pulsed DC magnetron sputtering system to reactively deposit titanium hafnium oxide films with high ion-to-neutral ratio. A schematic of the setup is shown in Figure 2-10. By using a pulsed DC power supply at the target, it is possible to deposit dielectric materials. Moreover, when the pulse is reversed there are a higher number of ions present in the plasma, increasing the ion-to-neutral ratio. In order to control the ion energy at the surface of the film, we used electrical potential (RF substrate bias) provided by an RF power supply connected to the substrate. The RF bias creates a localized glow discharge in the vicinity of the film surface, increasing the ion energy by creating a “self-bias”. By varying the RF substrate bias, it is possible to control the ion energy[27–29]. Two sputtering targets were used in the deposition of titanium hafnium oxide films: 3N hafnium and 3N titanium. Two power-regulated pulsed DC power supplies were used to apply 1.5 kW and 2 kW to the hafnium and titanium targets, respectively. A unipolar DC pulse was supplied to the targets at a frequency of 150 kHz with a 57% duty factor. A scanning magnetron was applied to each of the targets. Reactive sputtering in fully oxidized mode was done with a mixture of ultra high purity (UHP) argon and oxygen at a deposition pressure of approximately 0.67 Pa. Two titanium hafnium oxide (THO) samples were made with and without the RF substrate bias that provided RF power of 500 W (13.56 MHz), referred to as THO-B and THO-U, respectively. 200 mm diameter

silicon (100) wafers covered with a 500 nm of thermal silicon dioxide film were used as substrates for 6000 s long depositions at a revolution speed of 10 revolutions per minute. In both THO-B and THO-U, the analysis was done on a 2 cm^2 piece cleaved from the center of each of the two wafers to minimize variations in thickness and composition uniformity.

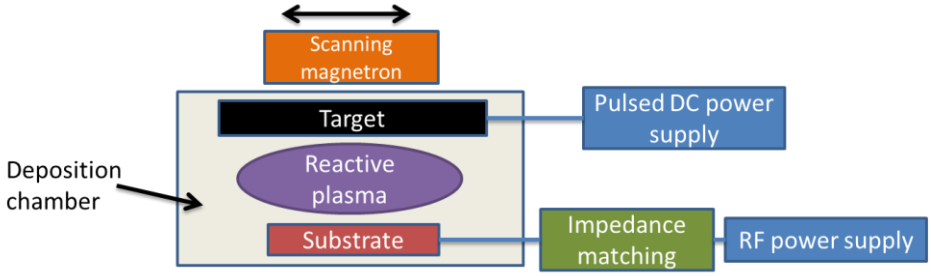

Figure 2-10. Schematic of the pulsed DC magnetron sputtering system with RF substrate bias used for the deposition of titanium hafnium oxide films.

Transmission electron microscopy (TEM, Hitachi H9500), atomic force microscopy (AFM, Veeco Dimension 3000), energy dispersive x-ray spectroscopy (EDS, Oxford INCA) and spectroscopic ellipsometry-reflectometry in the 380-930 nm range (Scientific Computing International FilmTek 2000 PAR-SE) were used to analyze the nanostructure, surface roughness, chemical composition and refractive index of the titanium hafnium oxide films. We will refer to the biased/unbiased samples as “THO-B” or “THO-U”, respectively.

2.2.4 Discussion

THO-B and THO-U were studied to compare their microstructures, surface roughness, chemical composition and refractive index. Table 2-2 lists the cation molar fraction obtained based on the EDS analysis, the pulsed-DC power applied to the targets, the power on the RF substrate bias, and the nominal thickness of THO-B and THO-U The thickness was cross-checked by both ellipsometry and by TEM.

Table 2-2. Sample description

Sample ID	Composition (molar frac.)	Power Ti (kW)	Power Hf (kW)	Power RF bias (W)	Thickness (nm)
THO-B	$Ti_{0.4}Hf_{0.6}O_y$	2	1.5	500	250
THO-U	$Ti_{0.4}Hf_{0.6}O_y$	2	1.5	0	250

2.2.4.1 Film nanostructure

Figure 2-12 shows TEM images of a cross section of the films. THO-B (Figure 2-11a) appears to contain granular features much smaller (diameter 1-2nm) than those (diameter 5-10nm) seen in THO-U (Figure 2-11b), suggesting that applying the RF substrate bias (increasing the ion energy at the substrate surface), reduced the grain size. The small size (less than 10 nm) of the granular features in both films would make these films appear to be amorphous under when studied by conventional x-ray diffraction (XRD). A further study needs to be done, for instance, with high-resolution TEM in conjunction with electron-energy loss spectroscopy to reveal detailed structural characteristics of these two films.

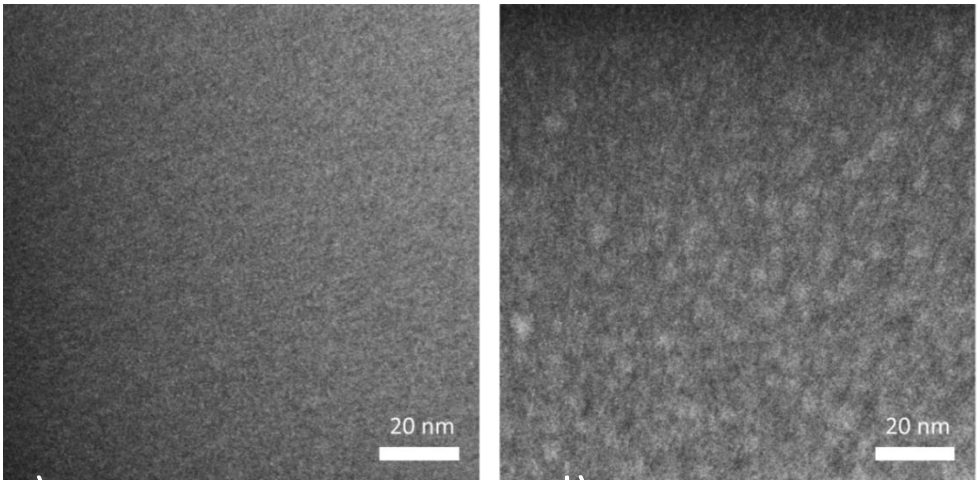

Figure 2-11. Transmission Electron Microscopy (TEM) image of titanium hafnium oxide a) with and b) without RF substrate bias.

2.2.4.2 Surface roughness and grain size

Figure 2-12 shows 3D profiles of 1μm^2 AFM scans: a) THO-B and b) THO-U. The both surfaces have comparable RMS roughness of minimal 0.22 nm for THO-B and 0.29 nm for THO-U. The two AFM images show features following the same trend that the granular features in Figure 2-11; average size of granular features (i.e grain size) seen in Figure 12(a) and (b) were extracted by Gwyddion software[30] that statistically provides average grain size (i.e. average diameter of grains). Grain size of $24 \pm 3\ nm$ and $45 \pm 6\ nm$ were obtained for THO-B (Figure 2-12a) and for THO-U (Figure 2-12b), respectively. The smaller size obtained for THO-B suggests that the extra kinetic energy, provided to the adatoms via ion bombardment, would enhance adatom migration (i.e. adatoms on THO-B have greater surface mobility), as suggested by Martin[15] and Ebert[31].

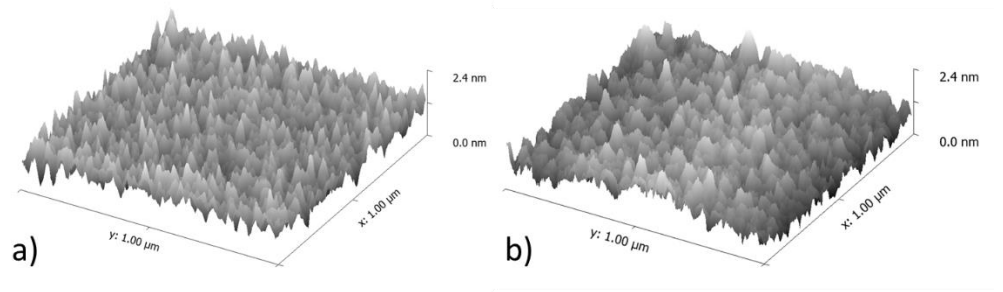

Figure 2-12. Atomic Force Microscopy (AFM) analysis shows smaller grain size on THO-B (a) than on THO-U (b). The scan size is 1μm^2.

2.2.4.3 Chemical composition and refractive index

EDS and spectroscopic ellipsometry-reflectometry were used to obtain chemical composition and refractive index of the films. As shown in Figure 2-13a) careful calibration intended to obtain THO-B and THO-U with comparable chemical composition ensured that the two films have comparable chemical composition: both samples have similar cation molar fraction. (1) is THO-B and (2) THO-U. The $K_{\alpha 1}$ peak of titanium and the $L_{\alpha 1}$ peak of hafnium are present at 4.51 keV and 7.89 keV, respectively. The application of a standard shows that the cation molar fraction is 0.6 Ti – 0.4 Hf for both samples, as stated in Table 2-2. The oxygen cannot be retrieved from EDS due to the low energy at which the oxygen $K_{\alpha 1}$ peak is present.

Dispersion graphs for a wavelength range 380-930 nm are shown in Figure 2-13b), where (1) and (2) represent the refractive indices of THO-B and THO-U, respectively. For a given cation molar fraction of titanium/hafnium, the refractive index is higher for THO-B than for THO-U. There are a number of plausible explanations for our observations: (i) films with higher density show higher refractive index[32]. THO-B deposited with RF substrate bias would have density higher than that of THO-U, (ii) size of internal structures (e.g. grain size) existing in films influences refractive index. This would suggest a dependence of refractive index on grain size (1-10nm) much smaller than the wavelengths (~930nm) used in our study. Moreover, grain boundaries present in THO-U

could increase the spatial fraction of voids and reduce the refractive index, (iii) oxygen-to-cation ratio: cation-rich films would present refractive index higher than that of oxygen-rich films; however, the optical absorption for cation-rich films is expected to be higher, too. In both samples, the extinction coefficient κ was below the detection limit ~10^{-5}. A lateral loss measurement setup is currently being set up to obtain κ much smaller than 10^{-5}, which will give us more insights.

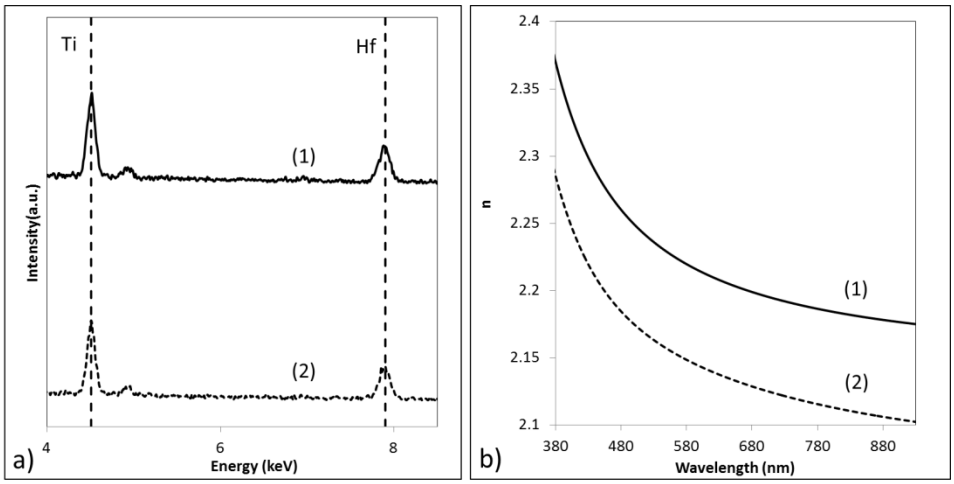

Figure 2-13. The samples have similar chemical composition; however, the sample with substrate bias has refractive index higher than that of the sample without bias. a) Energy Dispersive x-ray Spectroscopy (EDS) analysis. b) Refractive index coefficient n dispersion graph. Samples are: Ti0.6Hf0.4O y (1) with and (2) without RF substrate bias.

2.2.5 Conclusions

Titanium hafnium oxide alloys were deposited using pulsed DC reactive magnetron sputtering with and without RF substrate bias as high refractive index materials. It is demonstrated that, for a given cation molar fraction, by applying RF substrate bias, both the nanocrystalline grain present in the film cross-section and the granular size at the surface were reduced. The refractive index was higher in the sample with substrate bias in the visible spectrum. Control of the nanostructure and macroscopic properties of ternary metal oxides would improve the efficiency of optical and optoelectronic devices.

Further crystallinity and extinction coefficient studies are necessary to fully assess the relationship between the deposition conditions and the optical properties of the films.

2.3 Aluminum titanium oxide alloys: deposition of amorphous, transparent, corrosion-resistant films by pulsed DC reactive magnetron sputtering with RF substrate bias

2.3.1 Abstract

Optically transparent and mechanically flexible encapsulation films are desirable for advanced optoelectronic devices. Among many variations of encapsulation, ternary metal oxide films present good optical and mechanical properties. In this study, aluminum titanium oxide ($Al_{1-x}Ti_xO_y$) films were deposited with a range of Ti/(Ti+Al) molar fractions (*x)* using pulsed DC magnetron sputtering with RF substrate bias. Subsequently, the films were subjected to an Accelerated Weathering Environment (AWE) test at 220 °C, 1.6 atm and ~100% R.H. for 3 hours. Optical, chemical, and morphological analysis revealed that there exists a range of Ti/(Ti+Al) molar fraction (x=0.4-0.7) where films withstood the test, maintaining their optical, chemical, and morphological integrities. The study suggests that encapsulation films with continuously and spatially varying refractive index can be available by varying *x* within this range, forming encapsulation with broadband, wide angle antireflective coatings.

Keywords: amorphous materials, optical properties, reactive sputtering, aluminum titanium oxide, barrier, refractive index

2.3.2 Introduction

In recent years, a wide range of metal oxide thin films have been investigated for developing advanced electronics. For instance, various binary metal oxide thin films such as HfO_2, Al_2O_3, TiO_2 and also ternary alloys including $HfSiO_4$, HfTiAlO or TiAlO have been extensively studied in search of the next generation gate insulator in metal-insulator-semiconductor field effect transistors (MISFETs)[33–36]. Additionally, metal oxide

thin films are used in many optoelectronic devices such as light emitting diodes (LEDs), laser diodes, photodetectors and solar cells[37–40]. In these optoelectronic devices, the optical properties of the metal oxide films are as important as their electrical properties, since overall device performance is governed by efficient in- or out- coupling of light through the films. Furthermore, optoelectronic devices often require robust encapsulation to prevent moisture from entering and degrading the devices. Therefore, ideal metal oxide thin films are those whose optical properties can be reproducibly controlled by manufacturing methods and that exhibit strong structural and chemical durability upon exposure to harsh environment.

Transparent and mechanically flexible moisture/oxygen barriers have been long studied for use in organic LEDs and displays, as well as for food packaging and medical applications. Dielectric films such as metal oxides are practical materials for moisture barriers because of their transparency to visible light and low permeation by a wide range of gases[41]; notably, bulk metal oxides are entirely permeation free for oxygen. However, when metal oxides are deposited as thin films, they allow oxygen to permeate with a rate that is dependent on both the thickness of the film, and the type and volume density of structural defects. These films can have defects with a wide range of sizes; macro-defects (>1 nm), nano-defects (0.3-1nm) and lattice interstitials (<0.3 nm)[42]. The size of these defects determines how readily gas molecules permeate the film. For example, while gas molecules permeating through macro-defects are least inhibited, those permeating through lattice interstitials are highly hindered. The percolation-like dependence of gas permeation on thickness supports the fact that oxygen and water molecules permeate a film through these defects[41,43,44]. Similarly, in multilayer structures, the gas penetration into the film seems to be predominantly driven by the number of defects in any given film volume, even for large thicknesses[41,45]. This defect-driven permeation operates for both polar water molecules and non-polar oxygen molecules,

despite these molecules' having different diffusion mechanisms[42,46,47].

Permeation of oxygen and water molecules can accelerate film degradation, as it allows these contaminants to bond to and damage not only the film surface but also the interior of the film. Defects and grain boundaries present inside of poly-crystalline films, for instance, act as conducting channels for the contaminants, resulting in degradation initiated inside of the films. In contrast, unique characteristics of amorphous thin films, with the absence of these defects, are thought to be beneficial for reducing the permeation[48].

Amorphous materials have the advantage of being without grain boundaries and well-defined crystal structures, which gives them, in general, a greater mechanical hardness and durability[17,49]. Amorphous materials have a number of advantages over their poly-crystalline counterparts; their larger bandgap makes them more optically transparent[17], and, when their chemical bonds are all saturated, their high covalency provides a resistance to corrosion[17,50]. Moreover, the absence of grain boundaries reduces the diffusion of permeating molecules that would occur along them, minimizing chemical and physical interactions with environmental gas molecules[48]. Additionally, from a practical point of view, amorphous materials, in general, allow more scalable and less stringent deposition processes to be implemented[17].

Various metal oxide thin films have been studied to develop robust moisture barriers for optoelectronics. Amorphous aluminum oxide, for instance, is transparent, chemically inert, and has a large band gap (8.7 eV for bulk γ-Al_2O_3).[51] Another example, titanium oxide, presents high corrosion resistance and good substrate adhesion; however, its strong tendency towards crystallization makes its surface very reactive and susceptible to permeation and corrosion[45,46,52], leading to its low density and low mechanical strength and durability[46,50]. Diverse Chemical Vapor Deposition (CVD) techniques, such as Plasma Enhanced (PECVD) and Atomic Layer Deposition (ALD), as well as various

Physical Vapor Deposition (PVD) techniques, such as sputtering and e-beam evaporation, have been used to deposit amorphous oxide and nitride films; however, these films have not been able to achieve the industry-standard moisture and oxygen permeation rate requirements[46,53]. Multilayer organic/inorganic barrier coatings have proven to fulfill these requirements by increasing the path length of the defects, rather than reducing the number of defects. Nevertheless, the manufacturing cost is relatively high, due partly to their complex fabrication processes[44,46,53].

It has been shown that ternary oxides ($A_{1-x}B_xO_y$) have several advantages over binary oxides (AO_y). Mixing two different cations can provide higher crystallization temperature and a very smooth surface[17], good phase stabilization, high mechanical strength and flexible tunability of optical properties[50]. The cation molar fraction (i.e., x in $A_{1-x}B_xO_y$) can be continuously varied within a film to obtain a spatially varying refractive index, which benefits the overall performance of a film as an antireflective coating and as a moisture barrier.

According to Musil et. al[54], the energy delivered to the film by bombarding ions E_{bi}, with both charged (ϕ_i) and neutral (ϕ_n) fluxes can be defined as:

$$E_{bi} \cong E_i \frac{\phi_i}{\phi_n} = \frac{U_s i_s}{a_D} \quad (1)$$

Where E_i is the ion energy, $\frac{\phi_i}{\phi_n}$ is the ion-to-neutral flux ratio, U_s is the substrate bias, i_s is the substrate ion current density and a_D is the film deposition rate. Increasing the ion current density (ion-to-neutral ratio $\frac{\phi_i}{\phi_n}$) results in an increase in refractive index and a decrease in optical absorption of dielectric films.[28,31] It was shown that there is a range of the ratio $\frac{\phi_i}{\phi_n}$ where the formation of columnar morphology is suppressed and the adatom mobility is enhanced, increasing the density of the films at low ion energies E_i[28]. There is a range of ion energies where film density is maximized, and the columnar growth that is

normally promoted with sputtering can be suppressed, turning the films amorphous[29,31]. The suppression of columnar morphology depends also strongly on a_D: a high deposition rate will also create columnar growth [54], Moreover, excessively high ion flux was found to increase grain size and surface roughness in films, which promotes optical scattering.

Pulsed DC magnetron sputtering has proved to increase the ion flux ϕ_i, achieving higher current densities than those obtained in ordinary DC sputtering. Moreover, deposition of dielectrics can be performed by pulsed DC magnetron sputtering. By using RF substrate bias, an additional discharge is generated close to the substrate [29], increasing the ion bombardment effect and the energy of surface atoms, resulting also in enhanced surface diffusion.

Electrical properties of $Al_{1-x}Ti_xO_y$ deposited by PVD have been studied[34,35,55]; however, optical properties have not been extensively assessed. Moreover, it has been shown that ion-bombardment during deposition improves optical and mechanical properties of sputtered films[16]. In this paper, optically tunable aluminum titanium oxide films ($Al_{1-x}Ti_xO_y$) are demonstrated by pulsed DC reactive magnetron sputtering with RF substrate bias, and have been shown to be an effective material for corrosion resistant transparent thin films.

2.3.3 Experiment

$Al_{1-x}Ti_xO_y$ films with varying Ti/(Ti+Al) molar fraction *x* were deposited using a pulsed DC reactive magnetron sputtering system with RF substrate bias. Two sputtering targets used in the deposition: 3N aluminum and 3N titanium. The target surface area was 877cm^2. The chamber volume was 107 l. The target-to-substrate distance was 50 mm. The DC pulse was supplied at a frequency of 150 kHz with a reverse time of 2.9 µs (57% duty factor). The reactive sputtering was done with a mixture of Ultra High Purity (UHP) argon and oxygen supplied at flow rates of 20 and 40 sccm, respectively, at a deposition

pressure of approximately 0.67 Pa. The power applied to the two targets ranged from 0 to 4 kW, depending on the desirable *x*. The RF substrate power was 500 W RF (13.56 MHz) for all samples. Both power supplies were used in power regulation mode. The sputtering power ratio referred to in this paper as *R*, is defined as:

$$R = \frac{P_{Ti}}{P_{Ti} + P_{Al}} \quad (2)$$

where P_{Ti} and P_{Al} are the power supplied to the titanium and aluminum targets, respectively. Four films with different *x* were prepared with four different *R* (*R* = 0, 0.5, 0.75, 0.85) onto 200 mm diameter silicon (100) wafers. The deposition time was 3000 s for all the samples, resulting in a thickness of approximately 100 - 110 nm for all the samples.

To qualitatively assess the samples' ability to withstand gas permeation, an accelerated weathering environment (AWE) test was conducted by subjecting the samples to a high pressure (170 kPa), high temperature (220°C), and high humidity (~100%) environment for a duration of three hours. Tap water was used as the weathering agent.

The samples were analyzed before and after the AWE test by various techniques that were complementary to each other. The analysis was conducted with a visible-light microscope (VLM), a scanning electron microscope (SEM) equipped with Energy Dispersive x-ray Spectroscopy (EDS), and with spectroscopic ellipsometry-reflectometry (Scientific Computing International FilmTek 2000 PAR-SE). A 2 cm^2 sample was cut from the center of each of the wafers covered with the films. A 9-point thickness and refractive index uniformity test was done in the central part with 100 mm diameter of the wafers, showing 3% uniformity in thickness and 1.4% uniformity in refractive index, which can be approximately translated to 0.4% and 0.2% variations in thickness and refractive index across 2 cm^2 samples, ensuring that, within a 2 cm^2 sample, analyses (i.e.

reflectometry/ellipsometry and SEM/EDS) made at any point within a 2 cm^2 sample are acceptable for comparison. The samples were cleaved for cross-sectional SEM.

For simplicity, we refer to the samples before the AWE test as “AlTi-x” with *x* being the Ti/(Ti+Al) molar fraction, and the corresponding samples after the test are referred to as “AlTi-x AWE”.

2.3.4 Results

Table 2-3 shows the four samples under study. The chemical composition of each sample was calculated based on the EDS results before and after the AWE. The “Power Al+Ti” column indicates the individual power applied to the two sputtering targets, and the sputtering power ratio *R* ,as defined in Eq. (1), is also given for each sample. The last column, “AWE test”, states whether the samples passed or failed the AWE test, judged both by visual and optical assessments.

Table 2-3. Sample name, growth conditions and results for the Accelerated Weathering Environment (AWE) test for the four samples under study. The main variation was the power applied to each of the targets during the sputtering process.

Sample ID	Composition as-dep	Composition after AWE	Power Al+Ti (kW)	Power ratio *R*	AWE test
AlTi-0	AlO_y	AlO_y	3+0	0	FAILED
AlTi-0.4	$Al_{0.6}Ti_{0.4}O_y$	$Al_{0.6}Ti_{0.4}O_y$	3+3	0.5	PASSED
AlTi-0.7	$Al_{0.3}Ti_{0.7}O_y$	$Al_{0.3}Ti_{0.7}O_y$	1+3	0.75	PASSED
AlTi-0.8	$Al_{0.2}Ti_{0.8}O_y$	$Al_{0.75}Ti_{0.25}O_y$	0.7+4	0.85	FAILED

Figure 2-14(a) displays EDS profiles collected on the four samples before and after the AWE test. Spectra collected from AlTi-0.4, AlTi-0.7, and AlTi-0.8 show oxygen, aluminum, and titanium while AlTi-0 shows only aluminum and oxygen peaks, as expected.

The AlTi-0 and AlTi-0 AWE spectra suggest that the aluminum peak intensity was maintained during the AWE test. AlTi-0.4 and AlTi-0.7 withstood the AWE test, showing comparable titanium/aluminum peak intensity ratios before and after the test. The EDS spectra of AlTi-0.8 and AlTi-0.8 AWE indicate that the test caused significant chemical changes: the titanium/aluminum peak intensity ratio decreased drastically after the test. The oxygen molar fraction is comparable among all samples before the test.

Figure 2-14(b) shows the refractive index of the four samples before and after the AWE test. Figure 2-14(b) revealed that, over the range of wavelengths investigated in our study, the refractive index changes so that as x in $Al_{1-x}Ti_xO_y$ increases, the refractive index increases as well. This is consistent with chemical composition being the determining factor for refractive index of an AlTiO film. For AlTi-0, the refractive index n at 633 nm is 1.592, which is higher than amorphous aluminum oxides deposited by RF magnetron sputtering (n=1.48-1.58) by Pu et. al[55], but lower than reported amorphous Al2O3 (n=1.65). The measurement indicated that extinction coefficient κ was below the minimum measurable level (i.e. $\kappa < 10^{-5}$) imposed by the measurement system, the thickness of the films and relevant systematic errors across the range of wavelengths we examined; therefore, we concluded that κ for all the films should be below 10^{-5}.

As seen in Figure 2-14(b), the refractive index of AlTi-0.4 and AlTi-0.7 remained unchanged before and after the AWE test, which confirms that the density and chemical integrity of the films were maintained during the test. On the other hand, the refractive index of AlTi-0 and AlTi-0.8 dropped significantly after the AWE test, suggesting the presence of significant change in their chemical characteristics. Judged by the EDS spectra and refractive index spectra, it was concluded that AlTi-0.4 and AlTi-0.7 passed the AWE test.

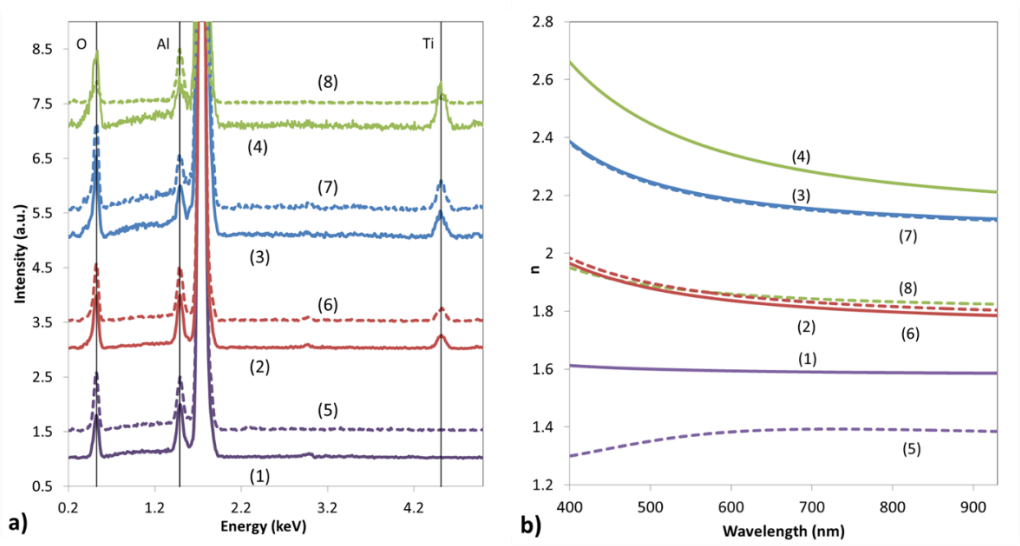

Figure 2-14. Titanium/aluminum ratio and refractive index and directly related. Also, we can see how two films passed the AWE test while the other two failed. (a) Energy Dispersive x-ray Spectroscopy (EDS) and (b) refractive index of the samples under study. Solid lines are the samples before the AWE test, and dotted lines are the samples after the AWE test. In panel (a), the expected peak positions of oxygen (0.525keV), aluminum (1.487keV) and titanium (4.511keV) are indicated with continuous vertical lines. The intense peak at 1.74 keV is associated with the silicon substrate on which the AlTiO films were deposited. (1) AlTi-0 (2) AlTi-0.4 (3) AlTi-0.7 (4) AlTi-0.8 (5) AlTi-0 AWE (6) AlTi-0.4 AWE (7) AlTi-0.7 AWE (8) AlTi-0.8 AWE.

Since AlTi-0.4 and AlTi-0.7 both passed the AWE test and are comparable to each other in terms of their optical characteristics and morphological appearance in SEM and VLM, AlTi-0.7 was selected to further extract intrinsic differences between passed and failed samples. Figure 2-15 shows cross sectional SEM images of AlTi-0, AlTi-0.7 and AlTi-0.8 before and after the AWE test. As seen in Figure 2-15(a)-(c), no films exhibit distinct features before the AWE test. After the AWE test, AlTi-0.7 appears unchanged, while AlTi-0 and AlTi-0.8 underwent significant structural changes. AlTi-0 AWE in (a) displays rough surface features, whereas AlTi-0.8 AWE in (f) shows the presence of two distinct layers: a layer of the original composition on the bottom, and a layer on top that no longer contains Ti. Macroscopic inspection of surfaces of the four samples by a VLM is shown in Figure 2-16. The contrast and brightness of these images were adjusted to reveal unique surface characteristics. As seen in Figure 2-16, all samples appear almost identical before the AWE test. After the test, AlTi-0 AWE in (a) and AlTi-0.8 AWE in (f) show

significant changes in appearance on their surfaces while AlTi-0.7 AWE in (e) appears to be nearly identical to AlTi-0.7 in (b).

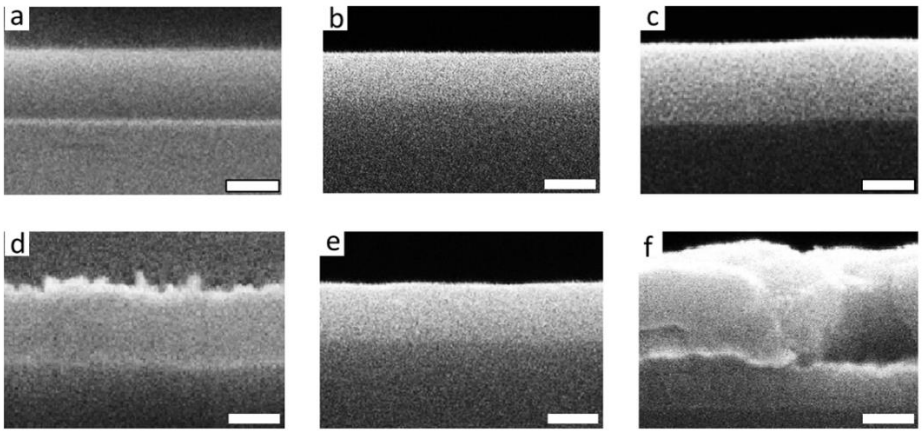

Figure 2-15. A cross sectional SEM (xSEM) study supports our conclusion that AlTi-0 and AlTi-0.8 failed the AWE test, whereas AlTi-0.4 and AlTi-0.7 withstood the AWE. This figure displays xSEM images of the samples before and after the Accelerated Weathering Environment test. (a) AlTi-0 (b) AlTi-0.7 (c) AlTi-0.8 (d) AlTi-0 AWE (e) AlTi-0.7 AWE (f) AlTi-0.8 AWE. The scale bar on all images is 100 nm.

2.3.5 Discussion

The optical properties and corrosion resistance of a thin film depend on its deposition method and also on the materials being used. It is for this reason that we studied aluminum titanium oxide alloys with four different compositions under the same deposition conditions. We used pulsed DC magnetron sputtering with RF substrate bias to increase film density and reduce optical scattering, as stated in the introduction.

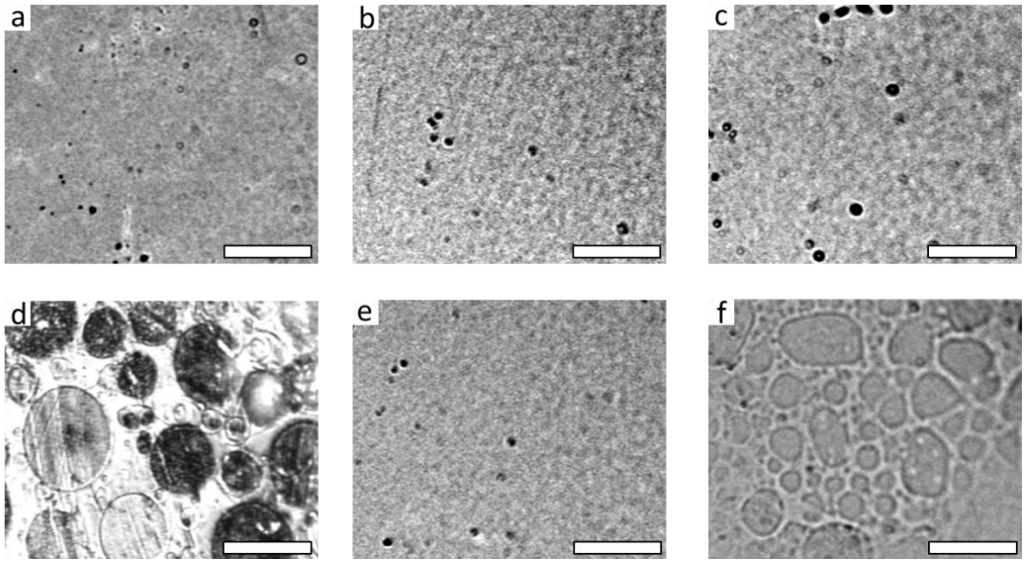

Figure 2-16. Visible Light Microscope (VLM) images before and after the AWE test show similar feature for all films before the AWE test. However, only the middle titanium range withstood the AWE test. The presence of bubble-like features on AlTi-0 AWE (d), indicate delamination due to poor film adhesion. AlTi-0.8 AWE (f) has island-like structures on the surface, due to corrosion damage. (a) AlTi-0 (b) AlTi-0.7 (c) AlTi-0.8 (d) AlTi-0 AWE (e) AlTi-0.7 AWE (f) AlTi-0.8 AWE. . The scale bar on all images is 0.2 mm.

The focus is firstly turned to the good endurance exhibited by AlTi-0.4 and AlTi-0.7 during the AWE test. AlTi-0.4 and AlTi-0.7 passed the AWE test and showed no distinguishable morphological changes after the test, which would suggest Al in the presence of moderate Ti content slowed down the crystallization and maintained these films in the state close to the notion of amorphous. In other words, moderate Ti content (x in the range of 0.4-0.7) in $Al_{1-x}Ti_xO_y$ provides better performance in the AWE test. Both AlTi-0.4 and AlTi-0.7 are ternary metal oxides and made of two binary alloys: aluminum oxide and titanium oxide. Ternary metal oxides have proven to have physical properties advantageous for both optical and moisture barrier applications, as described in the introduction.

As seen in Figure 2-15(a) and Figure 2-16(a), AlTi-0, as-deposited, showed no apparent morphological features (i.e., no grain boundaries, for instance) that could have resulted in significant permeation of water molecules during the AWE test. However, AlTi-0 failed the

AWE test; as seen in Figure 2-14(b), the refractive index of AlTi-0 dropped significantly after the test, which indicates that the film became porous. In addition, distinctive "bubbles", a clear sign of structural degradation, appeared on AlTi-0 AWE in Figure 2-16(b), suggesting the presence of significant structural changes in AlTi-0 after the AWE test. The increase in oxygen peak intensity by 35%, seen in the EDS spectrum of AlTi-0 AWE in Figure 2-14(a), would also indicate that AlTi-0 became porous with a large number of voids, where hydroxyl groups were trapped during the test. It is highly likely that the absence of titanium in AlTi-0 contributed to significant permeation of water molecules in the film: the weak adhesion, due also to the absence of titanium[49], may have contributed to the significant degradation of the film during the AWE test.

AlTi-0.8, $Al_{1-x}Ti_xO_y$ with *x* approximately 0.8, also failed the AWE test, in the sense that substantial changes were observed after the test. It was found that high Ti content (i.e., x~0.8) promotes degradation while moderate Ti content (i.e., *x* in the range of 0.4 ~ 0.7) provides benefits to $Al_{1-x}Ti_xO_y$ films. The substantial decreases in both titanium and oxygen peak intensities in the EDS spectra suggests that significant chemical changes occur after the test. In addition, Figure 2-15(c) displays a continuous, rather homogeneous, film before the test; however, after the test, as seen in Figure 2-15(f), the entire film appears to have disintegrated and swelled as evident in the apparent increase in the overall thickness; a clear sign of degradation. Such significant changes in both chemistry and morphology are a result of the film reacting with the harsh environment provided by the AWE test. Figure 2-16(f) displays a surface with the presence of "domains" not seen in Figure 2-16(c). Figure 2-15(f) suggests that the film reacted from its surface, leaving a thin layer of the original film intact underneath the upper reacted layer.

In the AWE test, surface adhesion and structural integrity of a film are expected to play the main role in determining the level and mode of failure. When the titanium content was

high (x=0.8 in AlTi-0.8), the film failed the test. The plausible clauses include: crystallization at low temperatures, generation of strong residual strain and formation of grain boundaries due to crystallization. All of our samples were deposited at nominally the same temperature, therefore, the finding of Musil et al.[49] supports our results in this regard: amorphous AlTiO has twice the amount of microhardness as its crystalline counterpart, and the crystallization temperature decreases with increasing titanium content. The fact that, in our findings, moderate Ti content caused an improved resistance to permeation and corrosion, while high Ti content caused a decline in resistance to permeation and corrosion, is in agreement with similar studies done on other ternary oxides[56,57]. These studies also attribute the improved performance to reduced stress within the oxide, achieved only within a certain range of cation content ratio in ternary alloys. Detailed structural analysis by analytical transmission microscope that will correlate microstructures with endurance of $Al_{1-x}Ti_xO_y$ films is currently in progress.

It should be noted that further optimization of pulsed DC magnetron sputtering, one of the unique features in our sputtering system, along with RF substrate bias, another unique feature, would widen the range of $Al_{1-x}Ti_xO_y$ alloys suitable for optically tunable moisture barriers. In our set of samples presented here, the substrate bias power was kept constant for all the samples. However, optimizing the substrate bias could further widen the optimal range of $Al_{1-x}Ti_xO_y$ alloys.

2.3.6 Conclusions

In this experiment, aluminum oxide, a smooth, conformal and transparent film, was co-sputtered with titanium to increase its surface adhesion and corrosion resistance, and to control its refractive index. It was found that the sample with no Ti failed the AWE test. Poor adhesion was suggested as the cause of the failure. The film with the highest Ti content also failed the AWE test. Crystallization and associated residual stress were

alleged as the causes. The core finding of this study is the presence of a certain range of Ti/Al content ratio that maximizes the endurance in the AWE test and provides refractive index high enough for various optical applications. It is also suggested that, when using pulsed DC magnetron sputtering with RF substrate bias, the RF substrate power applied in the substrate could be further optimized to widen the range of $Al_{1-x}Ti_xO_y$ alloy compositions suitable for applications where a tunable refractive index and moisture barrier properties are required. The effective range of *x* could be also maximized by using other or additional cations such as hafnium or silicon.

2.4 Aluminum oxide waveguides for improved transmission efficiency in the visible and near-infrared spectrum

2.4.1 Abstract

Transmission of light in the visible and near-infrared wavelength (λ) range is important both for energy (solar light, lighting) and for telecommunication purposes (silicon photonics). Transmission when λ >1000 nm is conveyed by semiconductor-based planar waveguides. In contrast, at shorter λ (350-1000 nm), semiconductors exhibit significant transmission loss. In planar waveguides, controlling optical characteristics such as refractive index *n* and extinction coefficient *k* of the constituent films is critical for the transmission of optical power. In this study, amorphous aluminum oxide (AlOx) was chosen for planar waveguides for the visible spectrum because of its relatively high *n* and low *k* in comparison to those of silica. 1 um thick AlOx films were deposited using pulsed-DC magnetron sputtering with RF substrate bias using different target/substrate power combinations to control ion energy. A set of the samples was annealed at 550 C for one hour in air. Optical properties of the waveguides were calculated using spectroscopic ellipsometry and prism coupling. Results show that by using high power at the target and substrate bias, it is possible to achieve <1 dB/cm transmission loss without post-deposition annealing, improving the ability to fit in low-temperature fabrication processes at high deposition rates.

2.4.2 Introduction

Passive waveguides are used to transport light between places that are apart in space. Depending on the wavelength of interest, waveguides are designed differently. Metallic waveguides are routinely used to transport microwaves (λ = 0.1-100 cm). When the wavelength is reduced to um, the metal' dielectric function changes, decreasing conductivity and increasing electromagnetic absorption. Thus, different waveguide

structures based on dielectric materials are needed. In the infrared range (λ = 1-10 um), semiconductors present low extinction loss; therefore, high refractive index (n) dielectric waveguides made out of semiconductor materials surrounded by low n cladding are used to transport information. When the wavelength is reduced even further to the visible and near-infrared range (VNIR, λ = 360-1000 nm) semiconductors present transmission loss (α) too high for effective transmission (α > 20 dB/cm). Metal oxides can then be used as the dielectric core material for structures surrounded by silica and/or air. Dielectric materials such as aluminum oxide (AlOx) have been traditionally studied for telecommunication wavelengths. AlOx presents a relatively high index (n ~ 1.65) in the visible spectrum.[55] In this work, waveguides with an AlOx core are used for the VNIR spectrum. Transmission loss α is attributed to absorption and scattering processes.

There are various techniques that can be used for thin-film deposition of dielectric waveguides. Examples include sputtering, ion beam deposition or atomic layer deposition (ALD).[58–60] ALD has been successfully used to fabricate AlOx waveguides. Aslan[61] was able to fabricate AlOx waveguides with α = 1.1 dB/cm at λ = 633 nm using ALD at medium temperatures (200/300 C substrate/chamber temperatures). ALD is a promising deposition technique for thin films [refs], but its low deposition rate, r ~ 0.08 nm/s reported as the fastest known deposition rate for ALD[62] is a limiting factor for waveguide fabrication, where thickness are typically 500 nm or more.

In the case of sputtering or e-beam deposition, as-deposited AlOx traditionally presents high transmission loss (α > 25 dB/cm), and annealing is needed to reduce α.[58,59] Smit[58] showed low transmission loss (α = 1 dB/cm) after annealing AlOx at T = 800 C. For some applications, annealing at high temperatures (> 150 C) is not viable. Examples include plastic substrates, organic electronics or electronic packaging, where high temperature (> 150 C) would damage the fabricated structure where an AlOx could be embedded. Pearce[59] used transition mode sputtering with a fast deposition rate (r = 0.128-0.371

nm/s) for the deposition of slab AlOx waveguides. They report on Al_2O_3 with the lowest losses of α = 26 dB/cm at λ = 633 nm for a thickness t = 564 nm, with much lower loss (α < 6dB/cm) as λ was increased to the near infrared region. Arnold[60] reported the deposition of low loss (α < 1 dB/cm) of AlOx waveguides using ion beam deposition while using a lamp to heat up the substrate above 175 C. The deposition rate was r < 0.08 nm/min

A deposition technique achieving high deposition rate r, low temperature T and low transmission loss α in the VNIR spectrum is needed for the possibility of AlOx waveguides to be successful. In this work, pulsed DC power (pDC) magnetron sputtering with radio frequency power (RF) substrate bias was used in transition mode. pDC increases the ion energy of the incoming adatoms. RF substrate bias was applied to the substrate in order to decrease the neutrals present at the surface of the substrate by creating a localized plasma, increasing the ion-to-neutral ratio. All films are subsequently annealed at 550 C. It is shown that, using high target pDC power (10 kW), RF substrate bias (100 W), low loss AlOx waveguides at fast deposition rates (r = 1.28 nm/s, α = 1.55 dB/com at λ = 633 nm) can be fabricated without annealing. Results suggest that using pDC magnetron sputtering with RF substrate bias, single- or multi-cation oxides can be deposited at fast rates and with good optical characteristics at low temperatures, enabling dielectric waveguides and other structures to be simply embedded into existing technologies.

2.4.3 Experiment

2.4.3.1 Sample fabrication

Aluminum oxide films with thicknesses t = 990$\pm$55 nm were deposited on 200 mm Schott Borofloat glass wafers. Prior to deposition, the wafers were chemically cleaned with deionized water and hydrogen peroxide. For deposition, a pulsed DC reactive magnetron

sputtering system with RF substrate bias from Tango Systems (San Jose, CA) was used in transition mode. 3N aluminum was used as a target. The target surface area was 877cm^2. The DC pulse was supplied at a frequency of 60 kHz with a reverse time of 10 us (40% duty factor). The reactive sputtering was done with a mixture of ultra high purity(UHP) argon and oxygen supplied at flow rates of 80 and 44-46 sccm, respectively, at a deposition pressure of approximately 17 Pa. The power applied to the target was either 5 kW or 10 kW. The RF substrate power was 0, 100 or 200W RF (13.56MHz frequency). Both power supplies were used in power regulation mode. Sputtering in transition mode was used to deposit the amorphous AlOx films. After deposition, the aluminum oxide waveguides were annealed at 550 C for one hour in air. A schematic of the deposition system is depicted in Figure 2-10. The sputtering system had a standard deviation of n=0.002 and t = 20.6 nm in the central 100 mm of the wafers.

2.4.3.2 Sample characterization

Polarized reflectometry (4 degree) and spectroscopic ellipsometry (70 degree) measurements (RE) were taken over a 360-838 nm wavelength range using a FilmTek 2000 PAR-SE (Scientific Computing International, Carlsbad, CA). RE measurements have a standard deviation of n=0.0001 and t=0.05 nm within the central 100 mm of the wafers when measured at the same spot. RE measurements were taken at the center (central 10x10 mm^2) of the 200 mm wafers.

A Metricon prism coupler setup with a rutile prism was modified to measure lateral loss in a custom setup. A He-Ne laser (633 nm) laser was used as an excitation source. A rutile prism coupler was chosen to couple the laser light into the waveguide core.

2.4.4 Results and Discussion

AlO_x films were deposited on Schott Borofloat glass, forming asymmetric planar waveguides with AlO_x as the core, and glass (substrate) and air (on top) as cladding.

Optical loss was measured using a prism coupler setup for evanescent coupling.[10] Briefly, laser light was first passed through a polarizer so transverse electric (TE) hit the prism surface. Through evanescent coupling, the light was then coupled to the film, and traveled in the propagation direction that the laser light was carrying – Figure 2-17a and 2b. Lateral propagation could occur via scattering events. Pictures of the transmitted beam over distance were taken and post processed using Matlab. The red pixel intensity of all pixels normal to the propagation direction were added, resulting in such light intensity profiles as Figure 2-17c.

The intensity profile of the coupled light beam propagating through the waveguide was fitted to retrieve attenuation loss α, defined as $\alpha = -\frac{1}{d}\log\left(\frac{I}{I_0}\right)$. Figure 2-17a and 2b show the case when there is no power applied at the substrate before and after annealing (samples 5/0 and 5/0 A), respectively. Qualitatively, in the as-dep sample (Figure 2-17a) the light travels a much shorter length than in the case of 5/0 A (Figure 2-17b), where the light is visible for a longer distance, and the intensity decay is not as pronounced. There are local spots where dust and/or surface scattering produce locally bright or dim spots [refs]. Figure 2-17c and d show intensity profiles of 5/0 and 5/0 A, respectively. Transmission loss fits for the specific intensity profile are shown in red dashed and dash-dotted lines for 5/0 and 5/0 A, respectively. Multiple fits or different profiles (not shown) were averaged to calculate the loss values shown in the panels. Initially, in the as deposited sample 5/0, the light decays rapidly (α=7.65$\pm$0.9 dB/cm), with 50 % of the power lost just after ~0.4 cm. After the sample is annealed, the loss decreases to α=1.54$\pm$0.3 dB/cm, with 50% of the power lost after ~1.9 cm. Under regular sputtering with no substrate bias, annealing reduced optical loss.

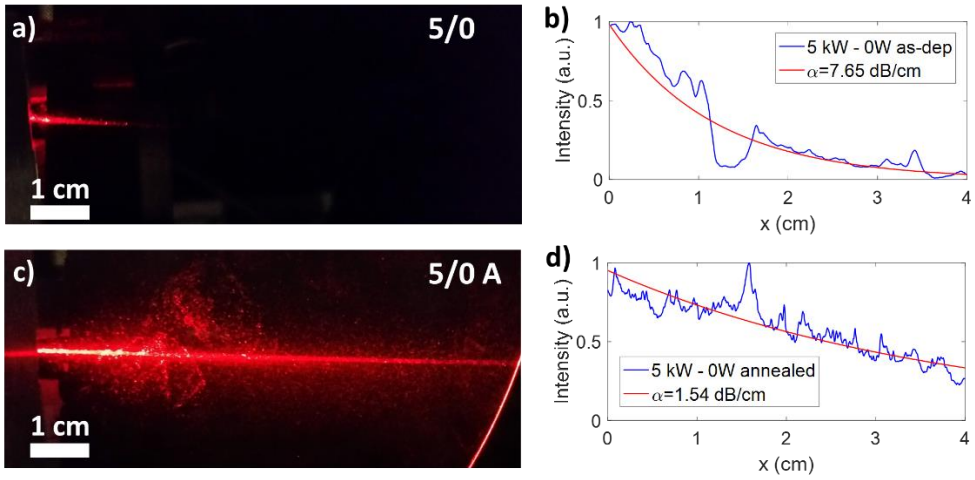

Figure 2-17. With no substrate bias, the propagation loss decreases after annealing. Pictures of the (a) as-deposited and of the (c) annealed samples, along with their respective propagation intensity profiles in (b) and (d).

The deposition conditions where varied to try and reduce optical loss without an extra annealing step. In order to study how the kinetics involving deposition affect the optical characteristics of the resulting films, the power at the target was first fixed to 5 kW, varying the RF substrate bias to 0, 100 and 200 W. Then, the power at the target was changed to 10 kW while the substrate power was fixed to 100 W. All these samples were annealed to 550 C for 1 h in air environment, and compared with their as-deposited counterparts. Annealing at lower temperatures (not shown) brought less significant changes, and Schott Borofloat substrates' limit temperature would not allow us to anneal at a higher temperature than 550 C.[63] Figure 2-18a is a dispersion graph showing the refractive index of the samples under study before and after annealing. The refractive index is higher than reported RF magnetron sputtered and slightly lower than reported amorphous AlOx.[55] The dispersion graphs were calculated using RE measurements and fitting to an SCI model. All the samples show a dispersion in the 360-838 nm range in accordance with amorphous aluminum oxide – no absorption peaks in the visible, with an increasing refractive index as the wavelength decreases to values close to the UV spectrum – aluminum oxide presents a bandgap in the UV (8.7 eV for γ-Al_2O_3).[51] Figure

2-18b shows the refractive index at λ = 633 nm of the studied samples. 5/0 has the highest refractive index n, followed by 10/100 and 5/100. 5/200 has the lowest n. After annealing (A samples), all the samples show a decreased refractive index from their initial values. Figure 2-18c shows the transmission loss associated with each film at λ = 633 nm. After annealing, α for all the samples settled to α ~ 1.4-1.6 dB/cm. However, the as-deposited samples presented a wide range of variation. Without any substrate bias power (sample 5/0), the as-deposited α was 7.65 dB/cm. When the substrate bias power was high – 5/200 – α was high was well, 8.7 dB/cm. 5/100, with intermediate substrate bias power, was found to have an initial lower α of 3.89 dB/cm. When the target power was increased to 10 kW for this intermediate substrate bias power, 10/100, α was found to be 1.63 dB/cm, i.e. a value comparable to the annealed samples.

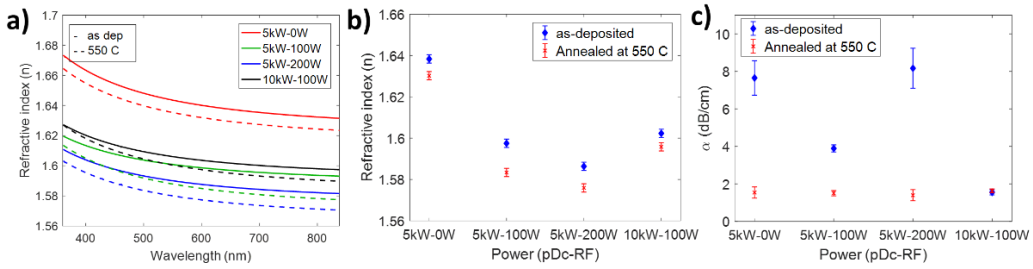

Figure 2-18. Different target/substrate power combinations led to different refractive indices and transmission loss. After annealing, refractive index decreased conformally, whereas optical loss decreased to α ~ 1.4-1.6 dB/cm for all samples. a) is a dispersion graph showing the refractive index over the λ = 360-838 nm wavelength range. b) and c) are the refractive index and transmission loss, respectively, at λ = 633 nm.

The complete set of samples deposited along with their deposition conditions and resulting refractive index and transmission loss measured at λ = 633 nm can be found in Table 2-4. We now hypothesize the relationship between target power, substrate power and annealing with the resulting refractive index, transmission loss and deposition rate. Given the complex kinetics during film growth, the structure zone model (SZM), first published by Movchan and Demchishin[64] attempts to provide general guidelines relating grain growth and grain structure with growth parameters such as substrate temperature,

pressure or ion bombarding energy. Different SZM models have been developed over time,[65–68] where adsorption and diffusion during sputtering have been studied for different species and different deposition conditions during and after thin film growth via sputtering. At low deposition temperatures we find Zone 1, where atomic shadowing causes the film to be microcrystalline. At higher deposition temperatures there is Zone 2 dominated by surface diffusion, where there is columnar growth. In between these two Zones we find Zone T, with dense, poorly defined fibrous grains. Zone T has proven to be mechanically more stable than 1 or 2 and with mixed crystalline phases. Computational models provide further understanding of the kinetics during thin film growth.[69]

Zone 1 would fit with 5/0: high n was produced by pDC, whereas high α was caused by the microcrystalline nature of the film. For 5/200, the ion-bombardment energy was too high, creating microcrystals with high defect densities and high compressive stress.[70] For samples 5/100 and 10/100, repeated renucleaction caused by the low-energy bombardment of an intermediate RF substrate power along with pDC target power provided low α. 10/100 presents higher n than 5/100, lower α and a faster deposition rate due to the fast deposition enabled by higher power at the target. These results agree with previous findings by Musil[54] and Sonderby[71].

Interestingly, all films produced low α when annealed. 5/0 retained the highest n among all of them. If annealing is not a problem, 5/0 is an appropriate choice. It presents the highest n among all the samples and low α after annealing. RF substrate bias power on top of pDC target power is a challenging engineering technique, with a lot of circuitry (RF impedance matching) needed.

Table 2-4. Sample description, with deposition and annealing parameters and resulting optical characteristics.

Sample as-dep (annealed)	Target pDC power (kW)	Substrate RF power (W)	Anneal (C)	n at 633 nm	α at 633 nm (dB/cm)
5/0 (A)	5	10	No (550)	1.638(1.630)	7.65(1.54)
5/100 (A)	5	10	No (550)	1.598(1.583)	3.89(1.5)
5/200 (A)	5	10	No (550)	1.586(1.576)	8.165(1.55)
10/100 (A)	10	10	No (550)	1.602(1.596)	1.55(1.63)

2.4.5 Conclusions

Refractive index n (measured in the VNIR) and transmission loss α (measured at λ = 633 nm) was measured for aluminum oxide (AlOx) waveguides. Pulsed DC magnetron sputtering with RF substrate bias in a range of target/substrate power combinations was used for deposition. With no substrate bias, post-deposition annealing at 550 C reduced the transmission loss from α = 7.65 dB/cm to α = 1.54 dB/cm. A combination of high ion energy and high ion-to-neutral ratio achievable by pulsed DC magnetron sputtering with RF substrate bias was used to deposit high index (n = 1.6) low loss (α = 1.55 dB/cm) AlOx waveguides without post-deposition annealing. The elimination of high temperature processing enables the usability of AlOx waveguides in devices such as organic LEDs, plastic substrates or electronics. Increasing n allows for further light concentration and further efficiency in many optical and optoelectronic devices.

2.5 References

(1) Crabtree, G. W.; Lewis, N. S. Solar energy conversion. *Phys. Today* **2007**, *60* (3), 37–42 DOI: 10.1063/1.2718755.

(2) *Solar Energy Perspectives: Executive Summary*; 2011.

(3) Margolis, R.; Coggeshall, C.; Zubo, J. *SunShot Vision Study*; 2012.

(4) Concentrated Solar Power http://en.wikipedia.org/wiki/Concentrated_solar_power.

(5) Barlev, D.; Vidu, R.; Stroeve, P. Innovation in concentrated solar power. *Sol. Energy Mater. Sol. Cells* **2011**, *95* (10), 2703–2725 DOI: 10.1016/j.solmat.2011.05.020.

(6) Wendelin, T.; Dobos, A.; Lewandowski, A. *SolTrace : A Ray-Tracing Code for Complex Solar Optical Systems SolTrace : A Ray-Tracing Code for Complex Solar Optical Systems*; 2013.

(7) Born, M.; Wolf, E. *Principles of Optics*; Elsevier, 1980.

(8) Haggerty, J. S. *Graded index antireflective coatings for glass*; 1982.

(9) Mahdjoub, A.; Zighed, L. New designs for graded refractive index antireflection coatings. *Thin Solid Films* **2005**, *478* (1–2), 299–304 DOI: 10.1016/j.tsf.2004.11.119.

(10) Ulrich, R.; Torge, R. Measurement of thin film parameters with a prism coupler. *Appl. Opt.* **1973**, *12* (12), 2901–2908.

(11) Klopfenstein, R. W. A Transmission Line Taper of Improved Design. In *Proceedings of the IRE*; 1956; Vol. 38, pp 31–35.

(12) Gordon, J. M. Gradient-index rods as flux concentrators with applications to laser fiber optic surgery. *Opt. Eng.* **2001**, *40* (3), 418 DOI: 10.1117/1.1347998.

(13) Liao, C.-W.; Yang, Y.-T.; Huang, S.-W.; Lee, M.-C. M. Fiber-Core-Matched Three-Dimensional Adiabatic Tapered Couplers for Integrated Photonic Devices. *J. Light. Technol.* **2011**, *29* (5), 770–774 DOI: 10.1109/JLT.2010.2101581.

(14) Gilman, P.; Dobos, A. System Advisor Model , General Description System Advisor Model , General Description. **2012**, No. February.

(15) Martin, P. J. Ion-based methods for optical thin film deposition. *Journal of Materials Science*. Kluwer Academic Publishers 1986, pp 1–25.

(16) Martinu, L.; Hichwa, B.; Rosa, S.; Klemberg-Sapieha, J. E.; Mattox, D. M.; Mattox, V. H. Advances in Optical Coatings Stimulated by the Development of Deposition Techniques and the Control of Ion Bombardment. *SVC Bull.* **2014**.

(17) Hosono, H. Transparent Amorphous Oxide Semiconductors for Flexible Electronics. In *Handbook of Transparent Conductors*; Ginley, D. S., Perkins, J. D., Eds.; Springer US: Boston, MA, 2011; pp 459–587.

(18) Diaz Leon, J. J.; Garrett, M. P.; Zhang, J.; Kobayashi, N. P. Aluminum titanium oxide alloys : Deposition of amorphous , transparent , corrosion-resistant films by pulsed DC reactive magnetron sputtering with RF substrate bias. *Mater. Sci. Semicond. Process.* **2015**, *36*, 96–102 DOI: 10.1016/j.mssp.2015.03.039.

(19) Biluš Abaffy, N.; McCulloch, D. G.; Partridge, J. G.; Evans, P. J.; Triani, G. Engineering titanium and aluminum oxide composites using atomic layer deposition. *J. Appl. Phys.* **2011**, *110* (12), 123514 DOI: 10.1063/1.3667134.

(20) Kim, D. Low temperature deposition of ITO on organic films by using negative ion assisted dual magnetron sputtering system. *Vacuum* **2006**, *81* (3), 279–284 DOI: 10.1016/j.vacuum.2006.04.003.

(21) Fang, Q.; Zhang, J. Y.; Wang, Z. M.; Wu, J. X.; Sullivan, B. J. O.; Hurley, P. K.; Leedham, T. L.; Davies, H.; Audier, M. a.; Jimener, C.; et al. Investigation of TiO 2 -doped HfO 2 thin films deposited by photo-CVD. *Thin Solid Films* **2003**, *428*, 263–268 DOI: 10.1016/S0040-6090(02)01221-X.

(22) Peacock, P. W.; Robertson, J. Band offsets and Schottky barrier heights of high dielectric constant oxides. *J. Appl. Phys.* **2002**, *92* (8), 4712 DOI: 10.1063/1.1506388.

(23) Chen, F.; Bin, X.; Hella, C.; Shi, X.; Gladfelter, W. L.; Campbell, S. a. A study of mixtures of HfO2 and TiO2 as high-k gate dielectrics. *Microelectron. Eng.* **2004**, *72* (1–4), 263–266 DOI: 10.1016/j.mee.2004.01.001.

(24) Von Lim, Y.; Wong, T. I.; Wang, S. Electronic structure and crystallinity of the HfO2–TiO2 thin films. *Thin Solid Films* **2010**, *518* (24), e107–e110 DOI: 10.1016/j.tsf.2010.03.098.

(25) Cisneros-Morales, M. C.; Aita, C. R. Optical absorption at its onset in sputter deposited hafnia-titania nanolaminates. *J. Appl. Phys.* **2010**, *108* (2010) DOI: 10.1063/1.3520678.

(26) Kobayashi, N. P.; Demaray, R. E.; Zhang, J.; Norris, K. J.; Fryauf, D. M.; Diaz León, J. J.; Flores, A.; Mullapdi, R.; Arunagiri, T.; Lu, L. Titanium hafnium oxide alloy films by a novel sub-atomic layer sputtering process for high index and graded index applications. In *MRS Online Proceedings Library*; 2013.

(27) Amin, a; Köhl, D.; Wuttig, M. The role of energetic ion bombardment during growth of TiO 2 thin films by reactive sputtering. *J. Phys. D. Appl. Phys.* **2010**, *43* (40), 405303 DOI: 10.1088/0022-3727/43/40/405303.

(28) Hultman, L. Low-energy (~100 eV) ion irradiation during growth of TiN deposited by reactive magnetron sputtering: Effects of ion flux on film microstructure. *J. Vac. Sci. Technol. A Vacuum, Surfaces, Film.* **1991**, *9* (3), 434 DOI: 10.1116/1.577428.

(29) Musil, J.; Šícha, J.; Heřman, D.; Čerstvý, R. Role of energy in low-temperature high-rate formation of hydrophilic TiO[sub 2] thin films using pulsed magnetron sputtering. *J. Vac. Sci. Technol. A Vacuum, Surfaces, Film.* **2007**, *25* (4), 666 DOI: 10.1116/1.2736680.

(30) Nečas, D.; Klapetek, P. Gwyddion: an open-source software for SPM data analysis. *Centr. Eur. J. Phys* **2012**, *10* (1), 181–188.

(31) Ebert, J. Activated reactive evaporation. *SPIE* **1982**, *325*, 29–38.

(32) Elert, G. *The physics hypertextbook*; 2006.

(33) Robertson, J. High dielectric constant gate oxides for metal oxide Si transistors. *Reports Prog. Phys.* **2006**, *69* (2), 327–396 DOI: 10.1088/0034-4885/69/2/R02.

(34) Shi, L.; Xia, Y. D.; Xu, B.; Yin, J.; Liu, Z. G. Thermal stability and electrical properties of titanium-aluminum oxide ultrathin films as high-k gate dielectric materials. *J. Appl. Phys.* **2007**, *101* (3), 34102 DOI: 10.1063/1.2432401.

(35) Auciello, O.; Fan, W.; Kabius, B.; Saha, S.; Carlisle, J. a.; Chang, R. P. H.; Lopez, C.; Irene, E. a.; Baragiola, R. a. Hybrid titanium–aluminum oxide layer as alternative high-k gate dielectric for the next generation of complementary metal–oxide–semiconductor devices. *Appl. Phys. Lett.* **2005**, *86* (4), 42904 DOI:

10.1063/1.1856137.

(36) Lu, N.; Li, H.-J.; Peterson, J. J.; Kwong, D. L. HfTiAlO dielectric as an alternative high-k gate dielectric for the next generation of complementary metal-oxide-semiconductor devices. *Appl. Phys. Lett.* **2007**, *90* (8), 82911 DOI: 10.1063/1.2396891.

(37) Granqvist, C. G.; Hultaker, A. Transparent and conducting ITO films : new developments and applications. *Thin Solid Films* **2002**, *411*, 1–5.

(38) Gordon, R. G. Criteria for Choosing Transparent Conductors. *MRS Bulliten* **2000**, 52–57.

(39) Fortunato, E.; Ginley, D.; Hosono, H.; Paine, D. C. Transparent Conducting Oxides for Photovoltaics. *MRS Bulliten* **2007**, *32* (March), 242–247.

(40) Hosono, H. Recent progress in transparent oxide semiconductors: Materials and device application. *Thin Solid Films* **2007**, *515*, 6000–6014 DOI: 10.1016/j.tsf.2006.12.125.

(41) da Silva Sobrinho, A. S.; Czeremuszkin, G.; Latrèche, M.; Wertheimer, M. R. Defect-permeation correlation for ultrathin transparent barrier coatings on polymers. *J. Vac. Sci. Technol. A Vacuum, Surfaces, Film.* **2000**, *18* (1), 149–157 DOI: 10.1116/1.582156.

(42) Roberts, A. P.; Henry, B. M.; Sutton, A. P.; Grovenor, C. R. M.; Briggs, G. A. D.; Miyamoto, T.; Kano, M.; Tsukahara, Y.; Yanaka, M. Gas permeation in silicon-oxide / polymer (SiO x / PET) barrier films : role of the oxide lattice , nano-defects and macro-defects. *J. Memb. Sci.* **2002**, *208*, 75–88.

(43) Chatham, H. Review Oxygen diffusion barrier properties of transparent oxide coatings on polymeric substrates. *Surf. Coatings Technol.* **1996**, *78*, 1–9.

(44) Lewis, J. S.; Weaver, M. S. Thin-Film Permeation-Barrier Technology for Flexible Organic Light-Emitting Devices. *IEEE J. Sel. Top. Quantum Electron.* **2004**, *10* (1), 45–57 DOI: 10.1109/JSTQE.2004.824072.

(45) Kang, B.-W.; Kim, W.-S.; Hwang, C.-M.; Moon, D.-Y.; Kim, J.-J.; Park, J.-G.; Park, J.-W. Titanium Oxide Thin Films Prepared by Plasma Enhanced Atomic Layer Deposition Using Remote Electron Cyclotron Resonance Plasma for Organic Devices Passivation. *Jpn. J. Appl. Phys.* **2010**, *49* (8), 08JG05 DOI: 10.1143/JJAP.49.08JG05.

(46) Park, J.-S.; Chae, H.; Chung, H. K.; Lee, S. I. Thin film encapsulation for flexible AM-OLED: a review. *Semicond. Sci. Technol.* **2011**, *26* (3), 34001 DOI: 10.1088/0268-1242/26/3/034001.

(47) Jamieson, E. H. H.; Windle, a. H. Structure and oxygen-barrier properties of metallized polymer film. *J. Mater. Sci.* **1983**, *18* (1), 64–80 DOI: 10.1007/BF00543811.

(48) Chen, S.-W.; Bai, C.-Y.; Jain, C.-C.; Zhan, C.-J.; Koo, C.-H. Durability of Indium Tin Oxide-Silver-Indium Tin Oxide Films against Moisture Investigated Through The Wettability of The Top Oxide Layer. *Mater. Trans.* **2007**, *48* (8), 2230–2234 DOI: 10.2320/matertrans.MER2007038.

(49) Musil, J.; Šatava, V.; Čerstvý, R.; Zeman, P.; Tölg, T. Formation of crystalline Al–Ti–O thin films and their properties. *Surf. Coatings Technol.* **2008**, *202* (24), 6064–6069 DOI: 10.1016/j.surfcoat.2008.07.012.

(50) Bergmann, C. P.; Stumpf, A. *Dental Ceramics: Microstructure, Properties and*

Degradation; Bergmann, C. P., Ed.; Springer Berlin Heidelberg: Berlin, Heidelberg, 2013.

(51) Ealet, B.; Elyakhloufi, M. H.; Gillet, E.; Ricci, M. Electronic and crystallographic structure of γ-alumina thin films. *Thin Solid Films* **1994**, *250* (1–2), 92–100 DOI: 10.1016/0040-6090(94)90171-6.

(52) Leng, Y. X.; Chen, J. Y.; Yang, P.; Sun, H.; Huang, N. Structure and properties of passivating titanium oxide films fabricated by DC plasma oxidation. *Surf. Coatings Technol.* **2003**, *166* (2–3), 176–182 DOI: 10.1016/S0257-8972(02)00780-6.

(53) Burrows, P.; Graff, G.; Gross, M.; Martin, P.; Hall, M.; Mast, E.; Bonham, C.; Bennett, W.; Michalski, L.; Weaver, M.; et al. Gas permeation and lifetime tests on polymer-based barrier coatings. *Proc. SPIE 4105, Org. Light. Mater. Devices IV* **2001**, *4105*, 75–83.

(54) Musil, J.; Poulek, V.; Valvoda, V.; Jehn, H. A. Relation of deposition conditions of Ti—N films prepared by d.c. magnetron sputtering to their microstructure and macrostress. *surfa* **1993**, *60*, 484–488.

(55) Pu, H.; Li, H.; Yang, Z.; Zhou, Q.; Dong, C.; Zhang, Q. Effect of Content Ratio on Solution-Processed High-k Titanium-Aluminum Oxide Dielectric Films. *ECS Solid State Lett.* **2013**, *2* (10), N35–N38 DOI: 10.1149/2.007310ssl.

(56) Ando, E. U.; Miyazaki, M. Moisture resistance of the low-emissivity coatings with a layer structure of Al-doped ZnO/Ag/Al-doped ZnO. *Thin Solid Films* **2001**, *392*, 289–293.

(57) Ando, E. Durability improvement of Ag-based low-emissivity coatings. **1994**, *3093* (94), 0–4.

(58) Smit, M. K.; Acket, G. a. Al2O3 Films for integrated optics. *Thin Solid Films* **1986**, *138*, 171–181 DOI: 10.1016/0040-6090(86)90391-3.

(59) Pearce, S. J.; Charlton, M. D. B.; Hiltunen, J.; Puustinen, J.; Lappalainen, J.; Wilkinson, J. S. Structural characteristics and optical properties of plasma assisted reactive magnetron sputtered dielectric thin films for planar waveguiding applications. *Surf. Coatings Technol.* **2012**, *206* (23), 4930–4939 DOI: 10.1016/j.surfcoat.2012.05.110.

(60) Arnold, S. M.; Cole, B. E. Ion Beam Sputter Depositoin of Low Loss Al2O3 Films for Integrated Optics. *Thin Solid Films* **1988**, *165*, 1–9.

(61) Aslan, M. M.; Webster, N. A.; Byard, C. L.; Pereira, M. B.; Hayes, C. M.; Wiederkehr, R. S.; Mendes, S. B. Low-loss optical waveguides for the near ultra-violet and visible spectral regions with Al2O3 thin films from atomic layer deposition. *Thin Solid Films* **2010**, *518* (17), 4935–4940 DOI: 10.1016/j.tsf.2010.03.011.

(62) Johnson, R. W.; Hultqvist, A.; F, B. S. A Brief Review of Atomic Layer Deposition: From Fundamentals to Applications. *Mater. Today* **2014**, *17* (5), 236.

(63) Schott Borofloat 33. The versatile floated borosilicate glass—with an infinite number of applications. SCHOTT Technical Glass Solutions GmbH 2014.

(64) Movchan, B. A.; Demchishin, A. V. STRUCTURE AND PROPERTIES OF THICK CONDENSATES OF NICKEL, TITANIUM, TUNGSTEN, ALUMINUM OXIDES, AND ZIRCONIUM DIOXIDE IN VACUUM. *iz. Met. Met.* **1969**, *28*, 653–660.

(65) Thornton, J. A. The microstructure of sputter-deposited coatings. *J. Vac. Sci. Technol. A Vacuum, Surfaces, Film.* **1986**, *4* (6), 3059–3065 DOI:

10.1116/1.573628.

(66) Grovenor, C. R. M.; Hentzell, H. T. G.; Smith, D. A. The Development of Grain Structure During Growth of Metallic Films. *Acta Metall.* **1984**, *32* (5), 773–781 DOI: 10.1016/0001-6160(84)90150-0.

(67) Mirica, E.; Kowach, G.; Du, H. Modified Structure Zone Model to Describe the Morphological Evolution of ZnO Thin Films Deposited by Reactive Sputtering. *Cryst. Growth Des.* **2004**, No. 4, 157–159 DOI: 10.1021/CG025596B.

(68) Ellmer, K. Magnetron sputtering of transparent conductive zinc oxide: relation between the sputtering parameters and the electronic properties. *J. Phys. D. Appl. Phys.* **2000**, *33* (4), R17–R32 DOI: 10.1088/0022-3727/33/4/201.

(69) Petrov, I.; Barna, P. B.; Hultman, L.; Greene, J. E. Microstructural evolution during film growth. *J. Vac. Sci. Technol. A Vacuum, Surfaces, Film.* **2003**, *21* (5), S117–S128 DOI: 10.1116/1.1601610.

(70) Musil, J.; Šícha, J.; Heřman, D.; Čerstvý, R. Role of energy in low-temperature high-rate formation of hydrophilic TiO2 thin films using pulsed magnetron sputtering. *J. Vac. Sci. Technol. A Vacuum, Surfaces, Film.* **2007**, *25* (April), 666 DOI: 10.1116/1.2736680.

(71) Sønderby, S.; Aijaz, A.; Helmersson, U.; Sarakinos, K.; Eklund, P. Deposition of yttria-stabilized zirconia thin films by high power impulse magnetron sputtering and pulsed magnetron sputtering. *Surf. Coatings Technol.* **2014**, *240*, 1–6 DOI: 10.1016/j.surfcoat.2013.12.001.

3 A niobium oxide-tantalum oxide selector-memristor self-aligned nanostack

3.1 Abstract

The integration of nonlinear current-voltage selectors and bi-stable memristors is a paramount step for reliable operation of crossbar arrays. In this paper, the self-aligned assembly of a single nanometer-scale device that contains both a selector and a memristor is presented. The two components (i.e. selector and memristor) are vertically assembled via a self-aligned fabrication process combined with electroforming. In designing the device, niobium oxide and tantalum oxide are chosen as materials for selector and memristor, respectively. The formation of niobium oxide is visualized by exploiting the self-limiting reaction between niobium and tantalum oxide; crystalline niobium (di)oxide forms at the interface between metallic niobium and tantalum oxide via electrothermal heating, resulting in a niobium oxide selector self-aligned to a tantalum oxide memristor. A steady-state finite element analysis is used to assess the electrothermal heating expected to occur in the device. Current-voltage measurements and structural/chemical analyses conducted for the virgin device, the electroforming process, and the functional selector-memristor device are presented. The demonstration of a self-aligned, monolithically integrated selector-memristor device would pave a practical pathway to various circuits based on memristors attainable at manufacturing scales.

3.2 Introduction

Memristors are a fundamental passive circuit element [1–3] that can be used to process or store information for the next generation computing [4,5]. In bi-stable operation, the resistance of a memristor can be explicitly programmed to one of the two levels, often

being referred to as high resistance state (HRS) and low resistance state (LRS), by applying a specific switching voltage. Once programmed, the resistance can be retained without supplying external electric power and read out at voltages lower than the switching voltage; hence, memristors can be used as non-volatile memories. When a specific memristor among others arranged in a crossbar array is selected, the so-called sneak path currents flowing through the unselected or partially selected memristors imposes significant challenges in programming or reading operations on the selected memristor [6–8]. This is mainly due to the insufficient nonlinearity of current-voltage (I-V) characteristics of memristors [6]. A device with highly nonlinear I-V characteristics, often referred to as selector, reduces the sneak path current when combined with a memristor, allowing the crossbar array to function correctly by mitigating the sneak path currents. In this paper, we demonstrate a nanometer-scale device in which a memristor and a selector are self-assembled.

A plethora of materials have been used as a switching layer in memristors, with transition metal oxides being the most widely used [5,9]. Among a range of choices for a switching layer, tantalum oxide (TaO_x)-based memristors present reliable switching [10,11]. In addition, niobium oxide (NbO_2) has been widely studied as a selector material, as it presents consistent negative differential resistance (NDR) – a critical enabling property for selectors [12]; therefore, in this paper, tantalum oxide and niobium oxide are chosen as memristor and selector, respectively, to fabricate an integrated selector-memristor (1S1M) cell. In designing NbO_2-TaO_x 1S1M cells, the key is to form the two materials in a simple and reproducible process, which precludes two separate deposition steps for NbO_2 and TaO_x that require careful control on their compositions. However, obtaining a specific composition (i.e. x in NbO_x in this case) for a binary oxide thin film sandwiched by layers of different materials is a daunting task. The composition needs to be tuned for a particular application – selector in this case – and obtaining deposition conditions that

work on a TaO_x surface and that form an appropriate interface with the top electrode (Pt in our case) is a challenge that we try to avoid. A nanoscale selector that is self-assembled into a memristor cell would be highly desirable[13,14].

In this demonstration, a $TaO_{2.2}$ film is first deposited on a TiN via, followed by a blanket metal Nb film deposition, avoiding the deposition of a specific composition of NbO_x. Upon electroforming - using electrical current spatially-confined by a current path defined by a diameter associated with the TiN via - the Nb film is oxidized in the vicinity of the $TaO_{2.2}$ film. As a result, a self-aligned NbO_2 selector and a TaO_x memristor are self-assembled on top of the TiN via, creating an 1S1M self-assembled cell. The electroforming process, a critical step for the successful self-aligned assembly of the 1S1M cell, is discussed in detail, revealing the microscopic picture and mechanism of the formation of a self-assembled selector on top of a traditional memristive material in a nano-1S1M cell by HRTEM combined with simulations.

3.3 Experimental

In designing an NbO_2-TaO_x 1S1M self-assembled cell, 3D electro-thermal modeling was carried out using COMSOL Multiphysics to assess the temperature profile within the device that results from steady-state Joule-heating upon the electroforming. Material parameters used in the modeling were taken from [15,16] for Pt, [17] for Nb, [18,19] for TaO_2, [20,21] for TiN, [17] for W, [22,23] for SiO_2 and [22,23] for Si_3N_4. The device structure used in the modeling is shown in Figure 3-1. A TiN via bottom electrode is represented by the embedded cylinder with a diameter of 75 nm and is connected to a 150 nm thick W layer (i.e. bottom electrode) at the bottom. The TiN via is surrounded by a stack of 20 nm thick SiO_2 and 15 nm thick Si_3N_4 isolation layers. A TaO_2 blanket layer (4 nm thick) placed above the TiN via/isolation layers represents the memristive switching layer. Above the TaO_2 layer, a 30 nm thick Nb and a 10 nm Pt (i.e. top electrode) are present. The temperature at the W bottom electrode was fixed to 293.15 K. The surface of the top

electrode is represented as a diffuse surface through which heat is dissipated to ambient by radiation; the surface emissivity $\epsilon = 0.8$ and an ambient temperature of 293.15 K were used.

The structure used in the modeling was subsequently fabricated with the dimensions provided above on a SiO_2/Si substrate. The substrate was ultrasonically cleaned with acetone and isopropyl alcohol, then reactive ion etched with oxygen plasma for 30 s and finally ion milling etched at 400 W in argon gas for 90 s prior to the bottom electrode deposition. A blanket W layer was deposited by chemical vapor deposition (CVD) on the substrate. Then, SiO_2 and Si_3N_4 layers were deposited, and 75nm via in nanoscale was patterned by a photolithographic process. The standard deviation of the nanovia size was 2.4 nm. After the formation of contact holes, titanium nitride (TiN) via for the bottom electrode were formed by CVD followed by chemical mechanical polishing. A $TaO_{2.2}$ switching layer was deposited by reactive RF sputtering using a $TaO_{2.2}$ target with an argon gas flow of 273 sccm and an oxygen gas flow of 77 sccm. Metallic Nb and Pt top electrode layers were deposited through shadow masks by electron beam deposition at ambient temperature, at a chamber pressure of 2.2 µTorr and a growth rate of 0.1 nm/s.

I-V characteristics were studied using an Agilent 4156c parameter analyzer. The voltage was applied to the Pt top electrode with the W bottom electrode grounded. A logarithmic voltage step and an integration time of 16.7 ms was used for all sweeps. The virgin step consisted of 0-1 V double sweep with current compliance set to 10 nA (68 voltage steps). The electroforming step consisted of 0-2 V double sweep with the current compliance set to 10 mA (48 voltage steps). The continuous switching operation consisted of $\pm$2.5 V double sweeps with a current compliance of 100 µA (96 voltage steps). An FEI NOVA dual beam was used to prepare samples for cross-sectional imaging and analysis in high resolution transmission electron microscopy (HRTEM) and electron energy loss spectroscopy (EELS) using an FEI Titan operated at 300 kV.

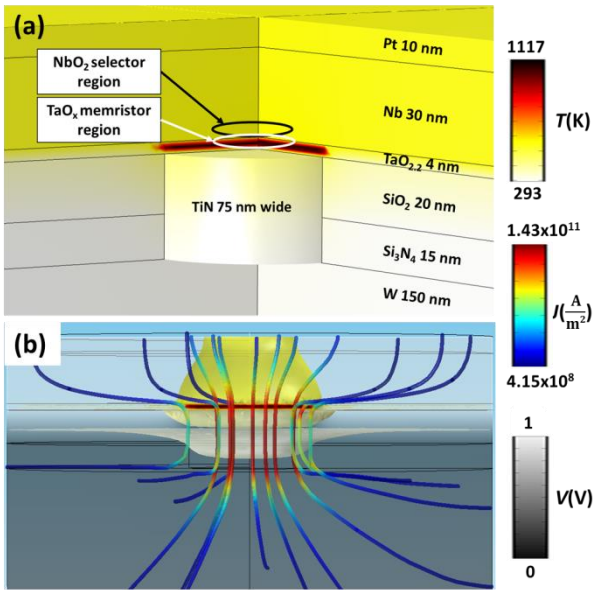

Figure 3-1. Modeling results indicate that, during the electroforming, the local temperature in the Nb/$TaO_{2.2}$ region is high enough to induce IMT in NbO_2. (a) a thermal map showing steady-state temperature in the Nb/$TaO_{2.2}$ region would locally reach ~1117 K during the electroforming. "NbO2 selector" and "TaOx memristor" would result from the electroforming. (b) electrical potential, current density streamlines and temperature isosurfaces are shown. The color bars for these variables are on the right.

3.4 Results and Discussion

Figure 3-1(a) displays a representative temperature map when the applied voltage is set to 1 V, indicating that Joule heat generated during the electroforming locally increases the temperature in the Nb/$TaO_{2.2}$ region. It appears that for 1 V, the local temperature at the $TaO_{2.2}$ layer would reach ~1117 K. Figure 3-1(b) shows three quantities: electrical potential *V*, current density *J* streamlines, and temperature *T* isosurfaces around the Nb/$TaO_{2.2}$ region. Upon the electroforming, it is possible that NbO_x would form at the Nb/$TaO_{2.2}$ interface, creating NbO_x/TaO_x [24,25]. Given the temperature map shown in Figure 3-1 (a), if NbO_2 is present atop the TaO_x layer, the resulting temperature ~1117 K is high enough to cause insulator-to-metal transition (IMT) for NbO_2 ($T_{IMT} = 1070\ K$) in the vicinity of the TiN via [24,26]. This NbO_2 would then show nonlinear I-V characteristics. As seen in Figure 3-1(b), the electrical current is well confined within the TiN via region, so the heating is localized in the vicinity of the TaO_x layer present directly atop the TiN

via. Hence, as the modeling suggests, by fabricating the specific structure shown in Figure 3-1 and performing the electroforming, it should be possible to vertically assemble a self-aligned NbO_2-TaO_x 1S1M cell, which is experimentally confirmed below. After the feasibility of a self-aligned 1S1M structure has been confirmed theoretically, an experimental demonstration is pursued.

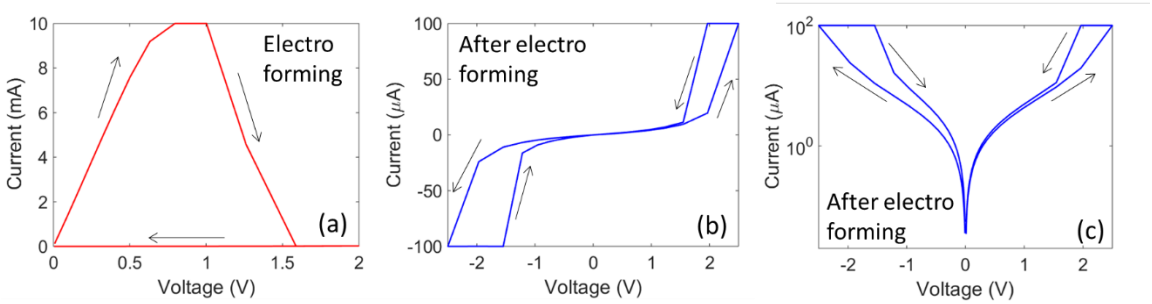

Figure 3-2. Upon electroforming, the device shows a combined, self-assembled 1S1M behavior. I−V of the device in (a) the electroforming state, and the following switching state showing nonlinear and memristive (1S1M) behavior plotted in (b) linear and (c) semi-logarithmic scale.

A series of I-V double sweeps were performed on the as-deposited structure (i.e. the virgin state) and on two acquired states – the electroforming state and the switching state – shown in Figure 3-2(a) and (b), respectively – explicitly established by operating the as-deposited structure. Thus correspondingly, there exist three progressive structural stages: the virgin state, the electroforming state (Figure 3-2(a)) and 1S1M (i.e. switching state) (Figure 3-2(b) and (c)). The quasi-linear I-V characteristics of the virgin state (not shown) indicate the presence of ~100 pA level of electrical current at $\pm 0.5\ V$, with asymmetric characteristics appearing in the positive and negative voltage regions that can be attributed to the two different materials used for the top and the bottom electrodes. Multiple quasi-DC sweeps were applied to electroform the TaOx memristor from virgin state first before the electroforming sweep shown in Figure 3-2(a) was applied to electroform the NbO_x layers. Figure 3-2(a) was collected during the electroforming. The device initially showed low resistance (R_{Low}~$60 - 70\ \Omega$ for the voltage sweep $0 - 1\ V$) followed by negative resistance between 1 and 1.6 V; subsequently, the overall

resistance of the device increased by 4 orders of magnitude (R_{High}~$200 - 300\ k\Omega$ for the voltage sweep 1.6-0 V). This appears to be type II electroforming – crystallization that results in a higher electrical resistance [12]. Once the electroforming step was completed, the device began to show consistent unipolar switching, as seen in Figs. 2(b) and 2(c). The I-V characteristics are highly nonlinear: The device was initially in high resistance or "OFF" state, with their with current increasing only after 2 V for the positive sweep to the low resistance or "ON" state (Fig.2(b)-(c)). At $V_{max}/2$ (1.25 V), the current is ~6 uA, whereas the current at 2.5 V is limited by the compliance limit set to 100 uA. The obtained 1S1M I-V nonlinear switching characteristics is explained as a combination of the NbOx selector providing high resistance at low voltages and the TaOx memristor providing switching between "ON" and "OFF" states. The negative sweep also shows highly nonlinear characteristics. The ON states in the positive and negative sweeps appear to be slightly asymmetric to each other, which could be originated from the asymmetry seen in the virgin state.

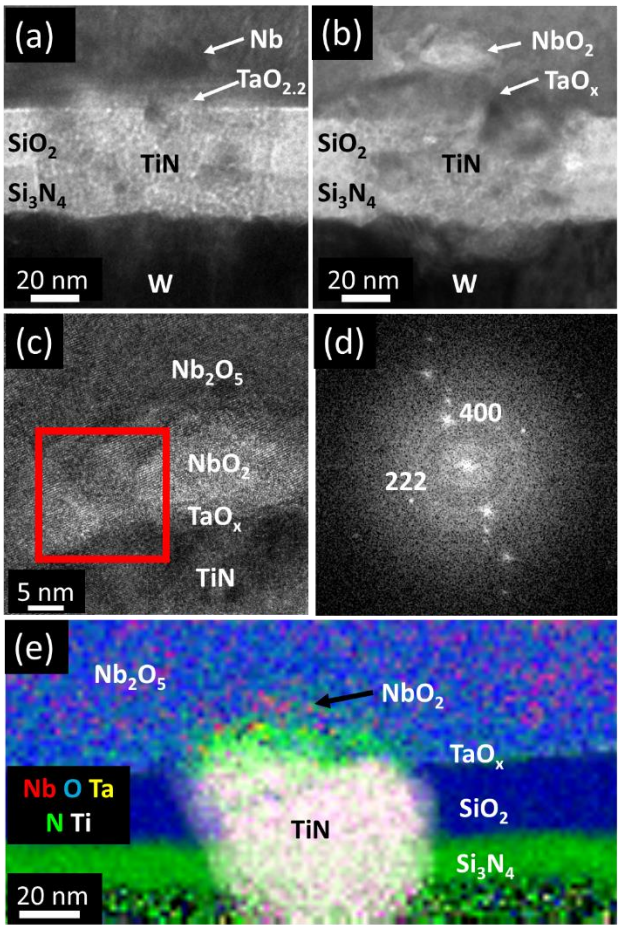

Figure 3-3. HRTEM cross-sectional images of the device (a) before and (b) after the electroforming. (c) shows the device at the OFF state after the electroforming, showing the region of the self-aligned NbO_2-TaO_x 1S1M, (d) a diffraction pattern associated with the red window of the image in (c), indicating the presence of the NbO_2 tetragonal crystalline phase. (e) is an EELS elemental map after the electroforming, indicating the presence of Nb, Ta, N, and O in the OFF state.

HRTEM was used to reveal structural and chemical transformations during the electroforming. Figure 3-3(a)(b) suggest that the device underwent physical changes upon the electroforming. The Nb sitting directly on top of the $TaO_{2.2}$/TiN via was oxidized, leading to increasing electrical resistance of the device (Figure 3-2(a)). The top of the TiN via on which the TaO_x layer sits appears to be swollen in Figure 3-3(b); this region is referred to as "TaO_x memristor region". The area above the TaO_x memristor region shows a brighter contrast; this region is referred to as "NbO_2 selector region". In Figure 3-3(c), at a higher magnification than Figure 3-3(b), the TaO_x memristor region appears to

contain TaO_x between the TiN via and the NbO_2 selector region. The NbO_2 selector region was found to be made of the tetragonal crystalline phase of NbO_2, as indicated in Figure 3-3(d) in which two specific combinations of symmetry and spacing match the (222) and (400) planes of tetragonal NbO_2. The area surrounding the NbO_2 selector region is found to be Nb_2O_5, further confirmed with HRTEM/diffraction pattern (not shown). This Nb_2O_5 region is discontinuous, with some regions replaced by the NbO_2 phase formed by Nb_2O_5 decomposition under high electric field and high temperature. Nb_2O_5 is expected to present linear I-V characteristics and is unintended for this device. A separate study focused on NbO_2 films without the TaO_x memristor layer present confirms thermally induced crystallization[27]. Figure 3-3(e) shows an EELS map for the key elements: Nb, O, Ta, N and Ti. A high N concentration region – a possible N release from the TiN via - is seen underneath the TaO_x memristor region, suggesting the swelling of the TiN via occurred upon the electroforming. Ta (yellow) is hardly noticeable in the TaO_x memristor region due mainly to a specific spatial resolution compared with the size of the device. A mixture of Nb (red) and O (blue) is found in what used to be the Nb layer in the virgin state, confirming the presence of NbO_2 and Nb_2O_5 phases suggested by HRTEM/diffraction pattern. The Nb concentration appears to be higher in the NbO_2 selector region (relatively more red intensity) than in the rest of the oxidized region of the Nb layer, suggesting that NbO_2 dominates the NbO_2 selector region, and Nb_2O_5 is present elsewhere in the Nb layer.

After assessing the electrothermal behavior of the as-deposited structure (Figure 3-1), I-V characteristics of the virgin state, the forming state, and the switching state were experimentally obtained (Figure 3-2), and the presence of an NbO_2 selector region and a TaO_x memristor region atop the TiN via was confirmed (Figure 3-3). Provided these results, an attempt to understand the physical mechanisms behind the electroforming is made as follows. The oxidation process has not been uniquely identified at this point, but

it is plausible that oxygen migrated from the $TaO_{2.2}$ layer vertically and laterally and/or from the outside of the device - the Pt electrode was found to be partially ruptured during the electroforming - contributing to the formation of NbO_x and TaO_x at the early stages of the electroforming (between 0 V and ~ 0.5 V in Figure 3-2(a)). At ~1 V, the temperature in the TaO_x region directly atop the TiN via was higher than T_{IMT} for NbO_2, as suggested by the modeling (Figure 3-1). The NbO_2 present directly atop the TaO_x/TiN via underwent IMT due to the elevated temperature during the electroforming at ~1V (Figure 3-2(b)). In Figure 3-2 (a), the device shows negative resistance starting at ~1 V and up to 1.6 V, in line with type II selector electroforming of crystalline NbO_2, hence creating the NbO_2 selector region [12]. The oxidation of Nb on top of the TaO_x layer with the presence of spatially confined electrical current is a self-aligned assembly process in terms of self-limited composition and self-aligned location. Self-limited composition: The conduction channel in a TaO_x memristor is found to be a Ta-O solid solution with saturated oxygen [28], which is a strong oxidizing agent that can oxidize Nb to its highest order of oxide (i.e., Nb_2O_5). Self-aligned location: Whatever form of Nb oxide exists in the conduction path of the cell needs to be conducting at high temperature induced by Joule heat during the electroforming process, otherwise the Nb oxides will be stressed by high electric field and decompose to a more conducting oxide. Therefore, the part of Nb_2O_5 in the conduction path is further reduced to NbO_2 under electric stress. By increasing voltage and current during the electroforming, NbO_2 present within the NbO_x layer (mainly Nb_2O_5) undergoes IMT due to Joule-heating that leads to temperature above T_{IMT} within the vicinity of the NbO_x/TaO_x interface, naturally creating an NbO_2 nanocap as a selector on top of the memristor conduction channel.

3.5 Conclusion

A self-aligned NbO_2-TaO_x 1S1M cell with self-limited composition based on a Nb-$TaO_{2.2}$ structure was built on top of a TiN via using a self-aligned assembly approach. A 3D

electrothermal simulation was setup to assess the temperature profile of the device upon the electroforming, confirming that the temperature was high enough to induce IMT of NbO_2 directly atop the TaO_x memristor region. The experimental demonstration clearly distinguished unique I-V characteristics of the three states: the virgin state, the electroforming state, and the switching state. Structural and chemical analysis using a combination of HRTEM and EELS confirmed the presence of NbO_2 and TaO_x on a device cross sectioned after the electroforming and switching. The self-aligned assembly of selector-memristor nanostack studied using Nb/TaO_x as an example can be extended to other similar materials systems, opening an alternative avenue to design and fabrication of large memristor crossbar arrays.

3.6 References

(1) Chua, L. O. Memristor—The Missing Circuit Element. *IEEE Trans. Circuit Theory* **1971**, *18* (5), 507–519.

(2) Yang, J. J.; Pickett, M. D.; Li, X.; Ohlberg, D. a a; Stewart, D. R.; Williams, R. S. Memristive switching mechanism for metal/oxide/metal nanodevices. *Nat. Nanotechnol.* **2008**, *3*, 429–433 DOI: 10.1038/nnano.2008.160.

(3) Strukov, D. B.; Snider, G. S.; Stewart, D. R.; Williams, R. S. The missing memristor found. *Nature* **2008**, *453* (May), 80–83 DOI: 10.1038/nature08166.

(4) Wang, Z.; Joshi, S.; Savel'ev, S. E.; Jiang, H.; Midya, R.; Lin, P.; Hu, M.; Ge, N.; Strachan, J. P.; Li, Z.; et al. Memristors with diffusive dynamics as synaptic emulators for neuromorphic computing. *Nat. Mater.* **2016**, *1* (September 2016) DOI: 10.1038/nmat4756.

(5) Yang, J. J.; Strukov, D. B.; Stewart, D. R. Memristive devices for computing. *Nat. Nanotechnol.* **2013**, *8* (1), 13–24 DOI: 10.1038/nnano.2012.240.

(6) Joshua Yang, J.; Zhang, M. X.; Pickett, M. D.; Miao, F.; Paul Strachan, J.; Li, W. Di; Yi, W.; Ohlberg, D. A. A.; Joon Choi, B.; Wu, W.; et al. Engineering nonlinearity into memristors for passive crossbar applications. *Appl. Phys. Lett.* **2012**, *100* (11), 98–102 DOI: 10.1063/1.3693392.

(7) Burr, G. W.; Shenoy, R. S.; Virwani, K.; Narayanan, P.; Padilla, A. Access devices for 3D crosspoint memory. *J. Vac. Sci. Technol. B* **2014**, *32* (4), 40802-1–23 DOI: 10.1116/1.4889999.

(8) Linn, E.; Rosezin, R.; Kügeler, C.; Waser, R. Complementary resistive switches for passive nanocrossbar memories. *Nat. Mater.* **2010**, *9* (5), 403–406 DOI: 10.1038/nmat2748.

(9) Waser, R.; Dittmann, R.; Staikov, C.; Szot, K. Redox-based resistive switching memories nanoionic mechanisms, prospects, and challenges. *Adv. Mater.* **2009**, *21* (25–26), 2632–2663 DOI: 10.1002/adma.200900375.

(10) Yang, J. J.; Zhang, M. X.; Strachan, J. P.; Miao, F.; Pickett, M. D.; Kelley, R. D.; Medeiros-Ribeiro, G.; Williams, R. S. High switching endurance in TaOx memristive devices. *Appl. Phys. Lett.* **2010**, *97* DOI: 10.1063/1.3524521.

(11) Lee, M.-J.; Lee, C. B.; Lee, D.; Lee, S. R.; Chang, M.; Hur, J. H.; Kim, Y.-B.; Kim, C.-J.; Seo, D. H.; Seo, S.; et al. A fast, high-endurance and scalable non-volatile memory device made from asymmetric Ta2O(5-x)/TaO(2-x) bilayer structures. *Nat. Mater.* **2011**, *10* (8), 625–630 DOI: 10.1038/nmat3070.

(12) Gibson, G. A.; Musunuru, S.; Zhang, J.; Vandenberghe, K.; Lee, J.; Hsieh, C. C.; Jackson, W.; Jeon, Y.; Henze, D.; Li, Z.; et al. An accurate locally active memristor model for S-type negative differential resistance in NbOx. *Appl. Phys. Lett.* **2016**, *108* (2), 18–23 DOI: 10.1063/1.4939913.

(13) Díaz León, J. J.; Norris, K. J.; Sevic, J. F.; Kobayashi, N. P. Integration of a niobium oxide selector on a tantalum oxide memristor by local oxidation using Joule heating. *Proc. SPIE* **2016**, *9924* DOI: 10.1117/12.2239609.

(14) Nandi, S. K.; Liu, X.; Venkatachalam, D. K.; Elliman, R. G. Self-assembly of an

NbO2 interlayer and configurable resistive switching in Pt/Nb/HfO2/Pt structures. *Appl. Phys. Lett.* **2015**, *107* (13), 132901 DOI: 10.1063/1.4932096.

(15) Flynn, D. R.; O'Hagan, M. E. O. Measurements of the Thermal Conductivity and Electrical Resistivity of Platinum from 100 to 900 °C. *J. Res. Natl. Bur. Stand.* **1967**, *71C* (4), 255–284.

(16) Arblaster, J. W. The Thermodynamic Properties of Platinum on ITS-90. *Platin. Met. Rev.* **1994**, *38* (3), 119–125 DOI: 10.1595/147106705X54262.

(17) Bobkov, V. P.; Fokin, L. R.; Petrov, E. E.; Popov, V. V.; Rumiantsev, V. N.; Savvatimsky, A. I. *Thermophysical Properties of Materials for Nuclear Engineering: A Tutorial and Collection of Data*; IAEA: Vienna, 2008.

(18) Henager, C. H.; Pawlewicz, W. T. Thermal conductivities of thin, sputtered optical films. *Appl. Opt.* **1993**, *32* (1), 91–101 DOI: 10.1364/AO.32.000091.

(19) Kelley, K. K. The Specific Heats at Low Temperatures of Tantalum Oxide and Tantalum Carbide. *J. Am. Chem. Soc.* **1940**, *62* (4), 818–819 DOI: 10.1007/s13398-014-0173-7.2.

(20) Shackelford, J. F. *CRC materials science and engineering handbook*; CRC Press, 2016.

(21) Pierson, H. O. *Handbook of Refractory Carbides & Nitrides: Properties, Characteristics, Processing and Apps*; William Andrew, 1996.

(22) Sze, S. M. *Physics of Semiconductor Devices*, 2nd ed.; Wiley: New York, 1981.

(23) Grove, A. S. *Physics and Technology of Semicondutor Devices*; Wiley: New York, 1967.

(24) Chudnovskii, F. A.; Odynets, L. L.; Pergament, A. L.; Stefanovich, G. B. Electroforming and Switching in Oxides of Transition Metals: The Role of Metal–Insulator Transition in the Switching Mechanism. *J. Solid State Chem.* **1996**, *122* (122), 95–99 DOI: 10.1006/jssc.1996.0087.

(25) Stormer, H.; Weber, A.; Fischer, V.; Ivers-Tiffee, E.; Gerthsen, D. Anodically formed oxide films on niobium: Microstructural and electrical properties. *J. Eur. Ceram. Soc.* **2009**, *29* (9), 1743–1753 DOI: 10.1016/j.jeurceramsoc.2008.10.019.

(26) Janninck, R. F.; Whitmore, D. H. Electrical conductivity and thermoelectric power of niobium dioxide. *Solid State Commun.* **1966**, *4*, xxv–xxvi DOI: 10.1016/0038-1098(66)90240-7.

(27) Zhang, J.; Norris, K. J.; Gibson, G.; Zhao, D.; Samuels, K.; Zhang, M. M.; Yang, J. J.; Park, J.; Sinclair, R.; Jeon, Y.; et al. Thermally induced crystallization in NbO2 thin films. *Sci. Rep.* **2016**, *6*, 34294 DOI: 10.1038/srep34294.

(28) Miao, F.; Strachan, J. P.; Yang, J. J.; Zhang, M. X.; Goldfarb, I.; Torrezan, A. C.; Eschbach, P.; Kelley, R. D.; Medeiros-Ribeiro, G.; Williams, R. S. Anatomy of a nanoscale conduction channel reveals the mechanism of a high-performance memristor. *Adv. Mater.* **2011**, *23*, 5633–5640 DOI: 10.1002/adma.201103379.

4 Reflectometry-Ellipsometry Reveals Thickness, Growth Rate and Phase Composition in Oxidation of Copper

4.1 Abstract

The oxidation of copper is a complicated process. Copper oxide develops two stable phases at room temperature and standard pressure (RTSP): cuprous oxide (Cu_2O), and cupric oxide (CuO). Both phases have different optical and electrical characteristics that make them interesting for applications such as solar cells or resistive switching devices. For a given application, it is necessary to selectively control oxide thickness and cupric/cuprous oxide phase volume fraction. The thickness and composition of a copper oxide film growing on the surface of copper widely depend on the characteristics of as-deposited copper. In this paper, two samples - copper films prepared by two different deposition techniques, electron-beam evaporation and sputtering - were studied. As the core part of the study, the formation of the oxidized copper was analyzed routinely over a period of 253 days using spectroscopic polarized reflectometry-spectroscopic ellipsometry (RE). An effective medium approximation (EMA) model was used to fit the RE data. The RE measurements were complemented and validated by using x-ray photoelectron spectroscopy (XPS), atomic force microscopy (AFM) and x-ray diffraction (XRD). Our results show that the two samples oxidized under identical laboratory ambient conditions (RTSP, 87% average relative humidity) developed unique oxide films following an inverse-logarithmic growth rate with thickness and composition different from each other over time. Discussion is focused on the ability of RE to simultaneously extract thickness (i.e. growth rate) and composition of copper oxide films and on plausible physical mechanisms responsible for unique oxidation habits observed in the two copper

samples. It appears that extended surface characteristics (i.e. surface roughness and grain boundaries) and preferential crystalline orientation of as-deposited polycrystalline copper films control the growth kinetics of the copper oxide film. Analysis based on a non-contact and non-destructive measurement such as RE to extract key material parameters is beneficial for conveniently understanding the oxidation process that would ultimately enable copper oxide-based devices at manufacturing scales.

4.2 Introduction

Copper oxide is one of the most studied metal oxides [1]. Oxidation of copper upon exposure to air at room temperature and standard pressure (RTSP oxidation) produces copper oxide referred to as native oxide, resulting in two stable copper oxide phases: cuprous oxide and cupric oxide [2–5]. Cuprous oxide (Cu_2O) is a p-type semiconductor with a direct band gap of 2.17 eV and an optical gap of 2.62 eV at 300 K [1,6,7], which makes it an interesting material for solar cells and light emitting diodes [8,9]. Cupric oxide (CuO) is also a p-type semiconductor with an indirect band gap ranging from 1.2 eV to 1.9 eV at 300 K [1,6,7]. CuO is widely used in applications such as gas sensors and catalysts [9–11]. Recently, copper oxide has shown promising results for resistive switching devices due to the different electrical properties offered by CuO and Cu_2O [12–14].

Structural variations in as-deposited copper films lead to different copper oxide formation mechanisms. For instance, variations in thickness and composition of copper oxide depend on properties of the as-deposited copper film such as thickness, crystalline morphology, deposition conditions, and surface roughness [15–17]. In addition, oxidation of copper has been studied and reported in different temperature regimes [7,17–20], pressures [5,20] and environments[21]. In the specific case of RTSP oxidation, the most common method to analyze the oxidation progressing over time is X-Ray Photoelectron Spectroscopy (XPS) to obtain both thickness and composition[2,5,21–25]. While an array of optical methods including reflectometry and ellipsometry [2,16,17,26] have been used to

merely extract oxide film thickness, obtaining composition using optical methods remains unexplored, mainly because of the similar refractive index of cuprous and cupric oxide in visible wavelengths [27]. Attempts to distinguish different copper oxide phases using RE have been done using stratified models [28].

With increased interest in high performance memory device development in materials science[29], the opportunity for simple, inexpensive, scalable device fabrication using existing common materials such as Cu and SiO_2 is extremely attractive. If a functional memory device is realized with an active switching copper oxide layer that can be fabricated from a reasonable amount of ambient environment exposure to a copper bottom contact, then the careful understanding of copper native oxidation will drive industrial device development. Moreover, controlling the oxide layer formation on copper interconnects can improve their resistivity and stability[30].

In this paper, first, we briefly present a Cu/SiO_2/Cu (i.e. Cu bottom electrode/SiO_2 dielectric film/Cu top electrode) resistive switch with volatile switching, which is referred to as volatile conductive bridge (VCB). During the fabrication of this resistive switch, the bottom Cu electrode was intentionally oxidized by RTSP oxidation for 1 to 7 days before depositing the SiO_2 film. Two findings are: the resulting copper oxide film enables the formation of a VCB through the SiO_2 film and the electrical behavior of the VCB (e.g. leakage current, low and high resistance states) critically depends on RTSP oxidation time. These two findings and the fact that both the switching and the oxidation involve the transport of Cu atoms motivated us to conduct the study - oxidation of copper by RTSP oxidation - described as the core part of this paper. Subsequently, we present a study on the RTSP oxidation of copper films deposited on Si (100) using two different deposition methods: electron beam evaporation and sputtering, to understand the oxidation processes by studying how thickness and composition of the oxide change over time. We create a fitting model for RE that provides reliable thickness and oxide volume fraction

continuously changing over time. Obtained results are compared with those obtained by XPS for validation. AFM and XRD are used to assess the results from the RE measurements and to further understand the characteristics of the as-deposited copper films and their influences to the oxide formation.

4.3 Experiment

4.3.1 Copper oxide-based volatile conductive bridge fabrication and characterization

A volatile conductive bridge (VCB) device was fabricated in cross bar format. The bottom electrode (BE) was formed by evaporating 2 nm Ti followed by 15 nm Cu through a shadow mask on a thermal SiO_2 film formed on a silicon substrate. Ti acts as an adhesion film between the SiO_2 and the Cu films. A blanket SiO_2 film 15 nm thick was sputtered on the Cu film by RF magnetron sputtering using a SiO_2 target in a Leybold sputtering system. The top electrode was Cu 10 nm/Pt 20 nm, evaporated through a shadow mask.

Current-voltage (I-V) DC measurements of the VCB were performed with an Agilent 4156C Precision Semiconductor Parameter Analyzer. The voltage was swept from 0 V to 0.6 V and then back from 0.6 V to 0 V. The current compliance range was set to 30 μA. The voltage was applied to the top electrode, keeping the bottom electrode grounded.

The nominal device stack is Cu/SiO_2/Cu. However, due to air exposure between the surface of the copper bottom electrode and the silicon oxide film, the presence of copper oxide between the bottom electrode and silicon dioxide can be expected. The RTSP oxidation of copper enabled volatile conductive bridge formation. In order to address the nature of the switching, copper samples were prepared to study the thickness and oxide phase composition of copper oxide over RTSP oxidation time.

4.3.2 Copper thin film deposition – sample preparation

In preparing two types of as-deposited copper film samples, copper was deposited on 100 mm diameter Si (100) substrates covered with native oxide. A Leybold electron-beam evaporation system was used for one sample referred to as “e-beam”. A Leybold sputtering system was used for the other sample referred to as “sputter”. For both samples, the thickness of the copper films was 32±2 nm. 10x10 mm^2 coupons from the center of the samples were used for characterization. Copper oxide was formed under laboratory conditions in Santa Cruz, California, USA: temperature ~300 K, pressure ~0.1 MPa, and average relative humidity ~87%.

4.3.3 Copper oxide characterization with RE

Polarized reflectometry (light incident angle of 4 degrees) and spectroscopic ellipsometry (light incident angle of 70 degrees) measurements were routinely taken over a 296-938 nm wavelength range (0.47 nm step size) for 253 days using a FilmTek 2000 PAR-SE (Scientific Computing International, Carlsbad, CA). A fitting model used to extract optical properties of copper oxide formation on the two samples consists of a silicon substrate covered with a silicon dioxide (2.48 nm thick) film, followed by a copper film and a copper oxide film. The top two films (i.e. the copper and copper oxide films) were modeled as two different films, each of which is described by the effective medium approximation (EMA) Landau-Lifshitz model, with a screening number of 0.3333, which models different media as spheres [31–33]. The root mean squared error (RMSE) over all studied wavelengths was minimized to fit the collected spectra. $\Delta = \lambda_{i+1} - \lambda_i$ was chosen to be 0.47 nm in the model. The choice of an EMA model was motivated by the comparable thickness of the oxide film and the surface roughness. In the description of the EMA model, the copper film was modeled as a mixture of copper and void, and the copper oxide film was modeled as a mixture of cuprous oxide, cupric oxide and void. Only cuprous oxide and cupric oxide were assumed to be present as they are the two stable

phases of copper oxide at RTSP[1]. The optical constants – refractive index and extinction coefficient – for all the constituent materials were fixed to those found in Palik[27] and thus, the thickness and volume fraction of the copper and copper oxide films were used as fitting parameters. The systematic error of these measurements was obtained by taking multiple measurements at the geometrical center of the 10x10 mm2 coupons for all data points appearing in Figs 2 and 3. The standard deviation σ was found to be 0.04 nm and 1.6% for the copper oxide thickness and the copper oxide volume fraction, respectively. σ for each data point is represented by an error bar.

4.3.4 Complementary copper oxide characterization with XPS

An XPS study of the copper films was undertaken to determine oxidation states of copper and correlate film deposition conditions with surface chemistry after 220 days of RTSP oxidation. Specific attention was given to the change in the relative amounts of Cu_2O and CuO present within a growing oxide. The analysis was done using a Thermo K-Alpha XPS spectrometer with an X-ray beam focused on a ~600 um diameter spot size at a standard 45 degree angle to the detector. A combination of survey scans, valence band, high resolution C(1s), O(1s), Cu($2p_{3/2}$), N (1s) scans, and Cu Auger LMM, were taken for this study.

The collected XPS spectra were curve-fitted to identify oxidation states and assign specific chemical elements to revealed peaks in the spectra. A 40 eV scan of the copper LMM Auger region was used to identify the oxidation states of Cu - specifically Cu_2O and CuO - to derive atomic percentage for the two samples.

4.3.5 Copper oxide characterization with AFM and XRD

An atomic force microscope (AFM) in non-contact tapping mode operated under ambient conditions (Bruker AFM) was used to scan the surface of the sputter and e-beam samples on the day of the deposition and after 268 days of RTSP oxidation. The AFM

scans were taken over a 500x500 nm^2 area at a 2Hz scan rate. All the scans were collected on the same day and with the same tip for consistency (i.e. fresh samples were re-deposited after 268 days of RTSP oxidation).

Grazing incidence x-ray diffraction (Rigaku SmartLab x-ray diffractometer with a Cu kα source operated at 40 kV and 44 mA in parallel beam mode) was used to study crystallographic properties of the two types of as-deposited copper films. The incident angle was 0.5 degrees, the scan speed was 1 degree/min, and the scan range was 20-80 degrees (2-theta).

4.4 Results

4.4.1 Copper oxide volatile conductive bridge

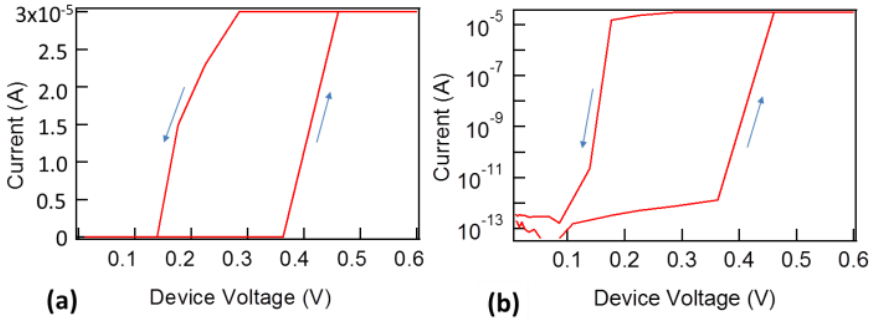

Figure 4-1. The VCB shows an 8 order of magnitude difference between the high-resistance and the low-resistance state. I-V curve under DC sweep of a copper oxide-based volatile conductive bridge (VCB) in a) linear and b) semi-logarithmic scale.

Current-voltage (I-V) DC measurements of the VCB were performed to assess the resistance value. Figure 4-1(a) shows an I-V curve from the device with two-wire measurement under double sweep. Figure 4-1(b) is a semi-logarithmic plot of Figure 4-1(a). As shown in the figure, under DC sweep from 0 to 0.6 V, the device was in high resistance state (HRS, with device current about 1 pA) until about 0.37 V at which the device switched to low resistance state (LRS, with device reaching current compliance 30 μA). During the return sweep from 0.6 V to 0 V, the device remained at LRSuntil about

0.15 V, at which point the device switched back to high resistance state (device current under 1 pA). The device switching mechanism is volatile. Although VCB operation mechanism is still under investigation, we propose an explanation involving both ionic and electronic transport. With voltage bias, copper ions migrate along the existing electric field and are aligned with one another to form a conductive bridge within the oxide matrix. Subsequently, electrons flow through the conductive bridge to bring the device to LRS. When the voltage bias is reduced or removed, the conductive bridge dissolves and loses its continuity, partly due to the high surface tension experienced by the bridge surrounded by the oxide matrix, diminishing the electron conductive path, and hence bringing the device back to HRS.

4.4.2 Copper oxide thickness measured with RE over time

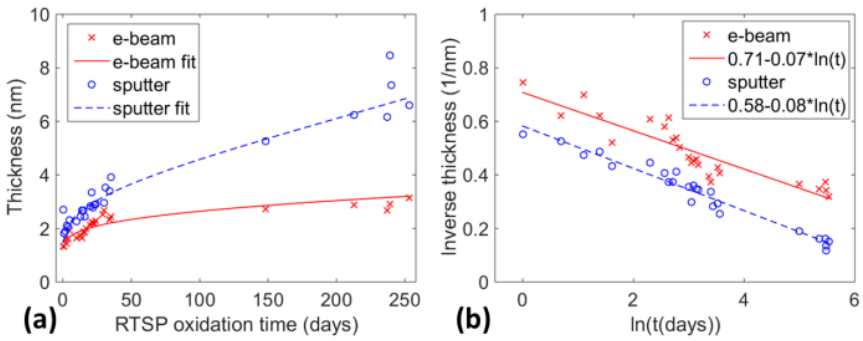

Figure 4-2. E-beam and sputter samples present an inverse-logarithmic growth rate trend with different initial thicknesses and growth rates. The dependence of total thickness of copper oxide on RTSP oxidation time is shown: (a) the total oxide thickness plotted as a function of oxidation time for the e-beam and sputter Cu samples and (b) the inverse of the total oxide thickness plotted as a function of the natural logarithm of RTSP oxidation time.

RE data was collected routinely over a period of 253 days to extract thickness and composition of the oxide film upon RTSP oxidation. Figure 4-2(a) shows the total oxide thickness of the e-beam and sputter samples plotted as a function of RTSP oxidation time (Note: The calculated standard deviation of 0.04 nm is smaller than the dot size representing a data point in Figure 4-2). The total oxide thickness was obtained by fitting the collected RE data with an EMA model with a mixture of cuprous oxide, cupric oxide

and void, as described in the Experiment section. After 1 day of RTSP oxidation, the e-beam sample presents an initial oxide thickness (1.34 nm) smaller than that of the sputter sample (1.81 nm). The thickness after 253 days of RTSP oxidation time is also smaller for the e-beam sample (3.13 nm) than that for the sputter sample (6.59 nm). The growth rate of the oxide film for both samples is not linear over 253 days, and it appears to be higher at the beginning of the studied time period of the RTSP oxidation with a decreasing trend over time.

Cabrera and Mott[34] showed that a thin native copper oxide follows an inverse-logarithmic growth rate: $\frac{1}{d} = A - B \cdot \ln(t)$, where *d* is the thickness at time *t*, *A* is the inverse initial thickness, and *B* is the inverse growth rate. Figure 4-2(b) shows an inverse total oxide thickness plotted as a function of natural logarithm of RTSP oxidation time of the two samples, clearly showing the inverse-logarithmic dependency on both samples as suggested by Cabrera and Mott[34]. The thickness and coefficients *A* and *B* in the Cabrera-Mott description were extracted from the plot and found to be different between the e-beam and the sputter samples as shown in Figure 4-2(b). The initial inverse thickness *A* of the e-beam sample (*A* = 0.71 nm^{-1}) is higher than that of the sputter sample (*A* = 0.58 nm^{-1}). This translates to the e-beam sample having a smaller initial oxide thickness than that of the sputter sample as seen in Figure 4-2(a). The inverse growth rate *B* for the e-beam sample (*B* = 0.07 $(nm \cdot \ln(days))^{-1}$) is smaller than that of the sputter sample (*B* = 0.08 $(nm \cdot \ln(days))^{-1}$), which indicates that the oxide grows at a slower rate on the e-beam sample compared to the sputter sample.

A number of publications have shown an inverse-logarithmic growth dependency for copper during RTSP oxidation with a range of *A* and *B* values [2,4,18,25]. For a metal oxide film that keeps forming on a metal surface, metallic elements (e.g. metal ions) need to be continuously supplied through the metal-metal oxide interface. Furthermore, the metallic elements need to be transported to the oxide-air interface through the growing metal

oxide. Copper ions do not gain thermal energy large enough to diffuse through the copper oxide films at room temperature (i.e. during RTSP oxidation). However, in very thin oxide films (less than 10 nm), a built-in electric field established between the copper cations at the copper metal-copper oxide interface and the oxygen anions at the copper oxide-air interface causes copper ions to leave the metal-metal oxide interface. As a result, copper ions migrate through the growing metal oxide film to reach the oxide-air interface [34,35]. This electric field decreases as oxide growth continues over time (i.e. as the oxide thickness increases). The drift velocity - the velocity of the moving copper ions - shows a decaying exponential dependence with respect to the electric field. Thus, the growth rate presents an inverse-logarithmic trend, decreasing until it stops at a certain thickness at which the electric field is no longer strong enough to sustain the growth of the oxide[34].

4.4.3 Copper oxide phase composition over time measured with RE

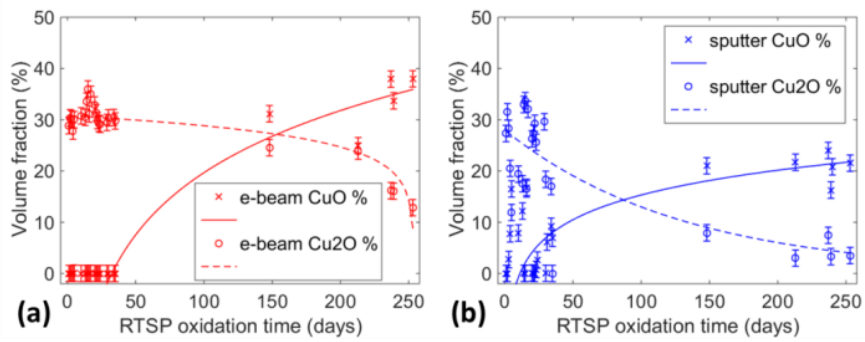

Figure 4-3. Copper oxide composition derived from the RE measurements shows that (a) e-beam and (b) sputter samples have different CuO and Cu2O volume fraction over RTSP oxidation time. The solid and dotted lines are guides to show apparent trends.

Data acquired using RE and fitted with an EMA model (described in the Experiment section) was used to calculate the CuO and Cu_2O volume fraction of the oxide film that change over time. Figure 4-3 shows the calculated volume fraction of CuO and Cu_2O for the (a) e-beam and (b) sputter samples. In both samples, the dominant phase is Cu_2O at the beginning of the RTSP oxidation, followed by CuO that starts forming later (after ~40

days) in the e-beam sample when compared with the sputter, where CuO formation appears to begin from the first measurement after deposition (within ~1 day). We define R_{CuO} as the ratio of the volume fraction of CuO to the sum of the volume fraction of CuO and that of Cu_2O: $R_{CuO} = \frac{CuO(v)}{Cu_2O(v) + CuO(v)}$ (%). It appears that the cross point where $R_{CuO} = 50\%$ (the point where $CuO\%$ and $Cu_2O\%$ trend lines cross) occurs later in the e-beam sample (after ~140-150 days) than in the sputter sample (after ~70-80 days), leading to a lower R_{CuO} in the e-beam sample after 253 days of RTSP oxidation.

To elucidate the observed oxide composition change shown in Figure 4-3, a simple thermodynamic assessment for the three phases, cuprous oxide, cupric oxide and copper is conducted as follows. The formation of Cu_2O on Cu with a source of oxygen (either H_2O or O_2) is more energetically favorable than that of CuO during the RTSP oxidation. Enthalpies of formation ΔH_f^0 for Cu_2O and CuO on Cu are $-40.8 \pm 0.5\ kcal/mol$ and $-37.7 \pm 0.5\ kcal/mol$, respectively. This is qualitatively consistent with Figure 4-3 indicating that Cu_2O will primarily form if there is an available Cu supply, near the Cu surface and during the early stages of the Cabrera-Mott's inverse-logarithmic growth, with copper ions drifting through the existing oxide. In addition, CuO appears to preferentially form on Cu_2O in the later stages of the RTSP oxidation as seen in Figure 4-3. This is qualitatively consistent with the enthalpy of formation of CuO on Cu_2O being $\Delta H_f^0 = -33.63 \pm 0.05\ kcal/mol$ under the circumstance that once Cu_2O is formed on Cu, further oxidation takes place from the surface of Cu_2O into CuO provided a less efficient Cu supply and more efficient O supply. All thermodynamic data has been gathered from JANAF tables [36].

4.4.4 Complementary copper oxide composition measured with XPS

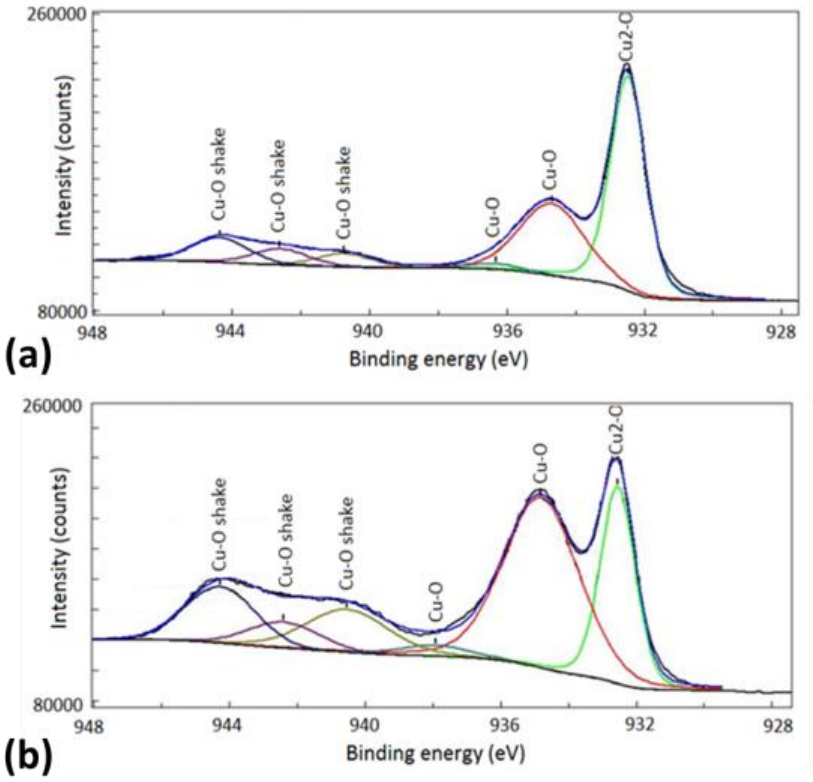

Figure 4-4. XPS after 220 days of RTSP oxidation time confirms a lower CuO/Cu2O ratio for the (a) e-beam sample when compared to the (b) sputter sample, with similar values to those obtained with RE.

XPS of the e-beam and sputter samples was collected after 220 days of RTSP oxidation time to validate the RE data and to further understand the nature of the native oxides present in the samples. Figure 4-4 shows the copper $2p_{3/2}$ spectra of (a) e-beam and (b) sputter samples collected using XPS. The copper $2p_{3/2}$ spectral region provides information about the chemical bonding states of copper, specifically copper bound as copper metal (Cu^0), cuprous oxide - Cu_2O (Cu^+) and cupric oxide - CuO (Cu^{2+}). The Cu $2p_{3/2}$ spectra show three primary features: Cu as Cu_2O (~932.5 eV), Cu as CuO (~934.7 eV), and satellite peaks from 940 to 945 eV. Satellite peaks are associated with Cu^{2+} atoms where d-orbitals participate in an excitation that removes energy from the exiting photoelectron. The area under each of these peaks is directly proportional to the number

of copper atoms bound in that state in the information volume of the top 4-6 nm (where most of the signal comes from). The measurements from e-beam and sputter samples are quite distinct. In the e-beam sample seen in Figure 4-4(a), roughly 50% of the copper atoms are present as Cu^{+} (cuprous oxide or even copper metal), with 30% of the signal coming from Cu^{2+} (cupric oxide or copper carbonate). A minimal amount of signal comes from the satellite shakeup peak, consistent with a smaller amount of cupric oxide (Cu^{2+}). The sputter sample seen in Figure 4-4(b) shows less cuprous oxide (Cu^{+}) and significantly more cupric oxide (Cu^{2+}) in comparison to the e-beam sample. Separating the cuprous oxide peak (23%) and adding the volume of satellite shakeup peaks to the cupric oxide peak intensity yield 77% Cu^{2+} atoms. We define X_{CuO} as the ratio of the atomic ratio of CuO to the sum of the atomic ratio of CuO and that of Cu_2O. Both samples appear to be a mixture of oxides; e-beam contains a similar amount of cuprous and cupric oxide ($X_{CuO} = 51\%$), whereas sputter presents less cuprous and more cupric oxide ($X_{CuO} = 77\%$). These results, while being atomic percentage, are in good agreement with the volume phase fraction calculated using RE after 220 days of RTSP oxidation.

4.4.5 Copper and copper oxide surface morphology measured with AFM

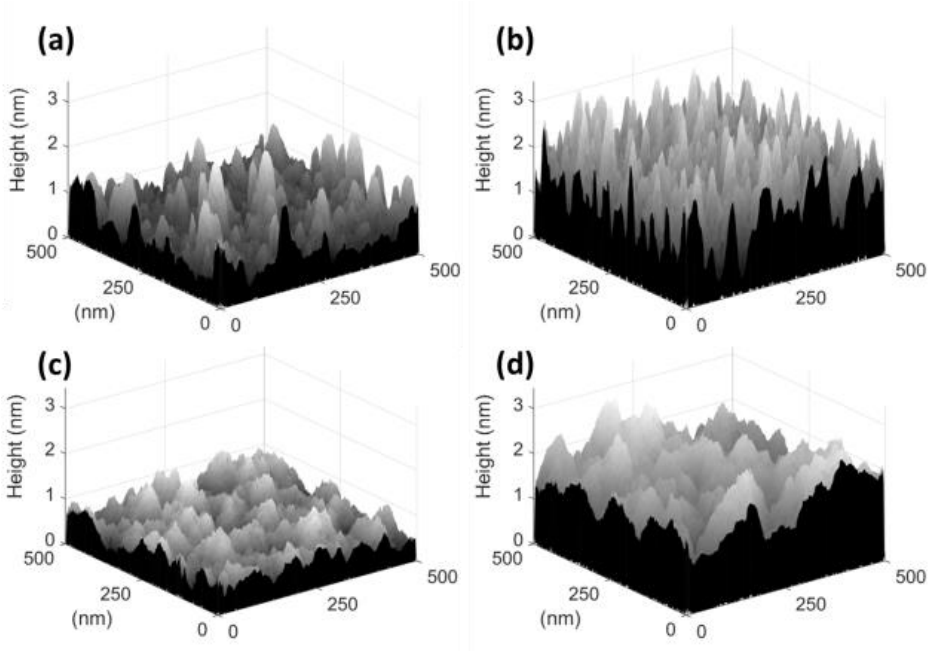

Figure 4-5. The surface morphology of the as-deposited copper films affects the thickness and composition of the oxide growth. 3D representative AFM graphs of a) same day deposited e-beam, b) same day deposited sputter, c) e-beam sample oxidized for 268 days and d) sputter sample oxidized for 268 days. Z-scale height of all graphs is 3.2 nm.

In order to assess (1) the relationship between surface morphology and RTSP copper oxidation kinetics and (2) the evolution of the surface morphology upon RTSP oxidation, AFM was used to scan arbitrary representational areas of the surface of the same day deposited and the 268 days oxidized samples. AFM 2D scans in Figs. 5(a) and (b) show surface morphology of same day deposited Cu samples by the two deposition methods, e-beam and sputter, respectively. Corresponding 268 days oxidized Cu surfaces at RTSP conditions are shown in Figs. 5(c) and (d). For both e-beam and sputter samples, the two same day deposited Cu samples show surface morphology rougher than that on their respective 268 days oxidized films. The average feature size (~20-50 nm) that characterizes the surface morphology of the same day deposited Cu samples, which we describe as low frequency features, represents the average size of Cu grains which are unique to each of the two types of same-day deposited copper samples. The Cu film deposited by e-beam in Figure 4-5(a) exhibits a smoother surface and larger average

grain size when compared to the sputtered Cu film in Figure 4-5(b). Correspondingly, the 2D scans of the 268 days oxidized films in Figs. 5(c) and 5(d) appear to preserve the average grain size and lower frequency features from their respective as-deposited Cu surfaces. However, both 268 days oxidized e-beam (Figure 4-5(c)) and 268 days oxidized sputter (Figure 4-5(d)) samples exhibit smaller structures (~5-10 nm), which we describe as high frequency features, in superposition with the original low frequency features associated with Cu grains. The smaller high frequency features of the 268 days oxidized samples can be associated with the morphology and roughness of the oxide formation over time. Oxide formation on both samples results in a smoother surface than as-deposited copper for both deposition techniques. However, the same day deposited e-beam sample exhibits a smoother surface and therefore lower average roughness than the same day deposited sputter sample, and the corresponding 268 days oxidized e-beam sample is also smoother with lower average roughness than the aged sputter sample. Average surface roughness of same day deposited Cu samples and oxidized samples are listed in Table 4-1. Because the same day deposited scans were taken shortly after Cu deposition, we assume that the surface morphology closely matches the as-deposited Cu film surface. It is worth noting that average Cu grain sizes derived from AFM scans of the same day deposited Cu surfaces are qualitatively useful for discussing the relative differences between the Cu surface characteristics of each sample. However, we rely on the more quantitatively precise average crystallite size from XRD measurements using Scherrer's equation [37] to compare crystalline morphology of the two samples.

4.4.6 Copper crystalline morphology measured with XRD

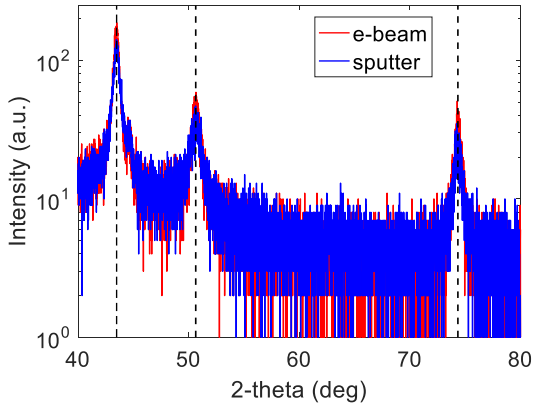

Figure 4-6. X-ray diffraction (XRD) shows different crystallite size on e-beam and sputtered copper films.

X-ray diffraction (Figure 4-7) was used to assess crystallographic characteristics of the Cu films. All the Cu films were found to be polycrystalline. Scherrer's analysis [37] was used to calculate average crystallite size (standard deviation $\sigma = \pm 0.6$ nm). It was found that the e-beam Cu film has an average crystallite size (15.8 nm) larger than that of the sputter (11.0 nm) Cu film, which is consistent with the qualitative observations on the difference in average Cu grain size indicated in AFM scans from Figure 4-5. A comparison made on peak intensities *I(hkl)* – diffraction peak intensity of a copper *hkl* plane - associated with specific crystallographic planes indicates that both *I(200)/I(111)* ratio and *I(200)/I(220)* ratio are higher in the sputter sample than in the e-beam sample as summarized in Table 4-1.

4.5 Discussion

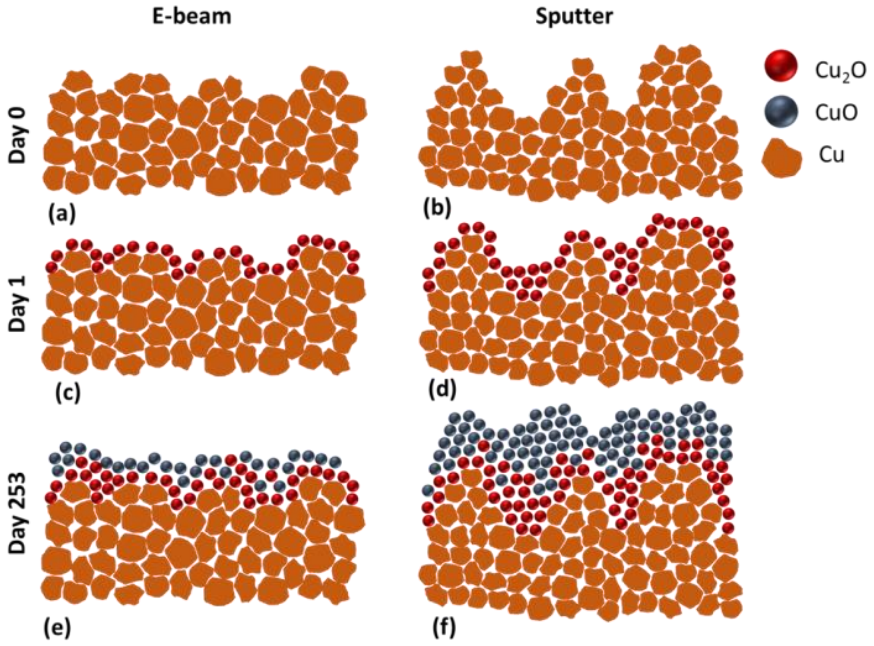

Figure 4-7. The e-beam sample, initially smoother and with a larger grain size, developed a thinner oxide at a slower growth rate over time, with less cupric oxide volume fraction than the sputter sample. The illustrations schematically represent e-beam/sputter samples (a)/(b)as-deposited, (c)/(d) after 1 day and (e)/(f) after 253 days of RTSP oxidation.

Our results clearly suggest that the thickness, composition and surface morphology of the resulting copper oxide films are related to surface morphology and crystallinity of the as-deposited copper films. Figure 4-7 schematically compiles all our findings: the e-beam sample, with a larger crystallite size, smaller surface roughness, lower *I(200)/I(111)* ratio and lower *I(200)/I(220)* ratio, developed a thinner copper oxide after 253 days of RTSP oxidation at a slower growth rate than the sputter sample (Figure 4-2). CuO started developing later on the e-beam sample (after ~40 days) than on the sputter sample (within ~1 day), and the cupric oxide volume fraction ratio R_{CuO} of the e-beam sample was lower even after 150 days at which the e-beam sample reached $R_{CuO} = 50\%$ (Figure 4-3). Furthermore, the surface roughness was found to decrease over time both in the e-beam sample and in the sputter sample after oxide growth. Notably, the volume fraction R_{CuO} calculated based on the RE measurements is in good agreement with the XPS

atomic ratio X_{CuO}. The structural and chemical quantities for the as-deposited copper films and for the copper oxide films are summarized in Table 4-1.

Table 4-1. Reflectometry-ellipsometry (RE) measurements over time show that copper oxide thickness and composition depend on roughness and crystallinity of the as-deposited copper film. The additional results obtained by the complementary characterization methods (i.e. XRD, AFM, XPS) support those obtained solely with RE.

		E-beam	Sputter	Characterization technique
Copper	Average crystallite size (nm)	15.8±0.6	11.0±0.6	XRD
	I(200)/I(111) ratio	0.29	0.33	XRD
	I(200)/I(220) ratio	1.26	1.84	XRD
	Surface roughness (nm)	0.222	0.374	AFM
Copper oxide	Surface roughness after 268 days (nm)	0.144	0.302	AFM
	Inverse growth rate $(nm)^{-1}$	0.71-0.07·ln(t)	0.58-0.08·ln(t)	RE
	Oxide thickness after 253 days (nm)	3.13±0.04	6.59±0.04	RE
	R_{CuO} after 220 days (%)	51±5	73±5	RE
	X_{CuO} after 220 days (%)	51±10	77±10	XPS

An effort is made to understand the relationship between the as-deposited copper film and the formation of copper oxide by RTSP oxidation. Preferential surface orientation (i.e. the dominant crystallographic plane) and extended surface characteristics (e.g. surface roughness and grain boundaries) are expected to control the growth kinetics of the formation of copper oxide on polycrystalline copper under a given thermodynamic driving force. In other words, in our experiments, two factors are: 1) the role played by the extended surface characteristics of the as-deposited copper in the nucleation of copper oxide in the early stage of the RTSP oxidation and 2) the thermodynamic evolution of a specific copper oxide phase within a growing copper oxide. Grain boundaries and other extended defects on Cu surfaces are known to provide nucleation sites for oxide islands [38]. More effective surface area present within a unit area on rough surfaces receives an

increased amount of metal and oxygen species. In addition, depending on their size, grains that appear on a copper surface can also contribute to variations in surface energy by providing grain boundaries that act as excess energy sources (e.g. mechanical strain and localized electric field along grain boundaries). Larger grain size is associated with a slower oxide growth rate [39], suggesting that smaller grains promote faster oxidation as seen in the sputter sample (Table 4-1). Furthermore, the extent to which oxidation is promoted is expected to depend on a specific environment provided by different crystalline planes. Studies on single crystal copper films show that (100) crystalline surface has a faster oxide growth rate than that on (111) or (110) [17]. This preferential growth of oxide on the (100) surface also applies to polycrystalline films – as-deposited Cu films used in our experiment - making (111) and (110) surfaces more resistant to oxidation [39]. As shown in Table 4-1, the sputter sample with higher *I(200)/I(111)* and *I(200)/I(220)* ratios developed an initially thicker copper oxide film and grew at a faster rate over the rest of RTSP oxidation. From thermodynamics, both cuprous and cupric oxide phases are expected to form concurrently; however, the formation of Cu_2O appears to be preferred at the beginning when a kinetic view - the copper ions diffusing through the oxide film – is added and driven by the fact that the formation of Cu_2O is energetically more favorable than that of CuO on the Cu surface. Once the diffusion of Cu ions through the oxide film slows down, the Cu_2O growth slows down correspondingly, and the formation of CuO directly on the Cu_2O surface becomes predominant for given oxidation conditions. In other words, when the Cu_2O growth rate falls below a certain critical point, the formation of CuO on the Cu_2O surface through the oxidation of Cu_2O is expected to be energetically preferred, further suppressing down the Cu_2O growth (Figure 4-3). Isshiki[16,39] studied RTSP oxidation on two different sputtered copper samples with different initial structural characteristics obtained by tuning substrate bias during the deposition. After 53 days of RTSP oxidation, the unbiased Cu film with a relatively smaller crystalline size, more surface defects, rougher surface morphology and

with apparent columnar structures when compared to the biased Cu film developed a thicker copper oxide film with a higher R_{CuO} ratio than that of the biased Cu film. These results qualitatively agree with our results, and we believe that if an oxidation time much longer than 53 days was used in the Isshiki's experiment[16,39] (note: the RTSP oxidation time was 253 days in our experiment), they would have eventually seen the development of CuO on the biased film. Clarke[26] also suggests that the voids and thicker Cu regions present in single crystal copper films provide extra copper surfaces for oxidation, which seems to be consistent with the assertion derived from our study, as well as the observations by Zhou[38], in that, grain boundaries and other extended defects promote oxide growth. Furthermore, the presence of extended surface defects would increase oxygen dissociation from O_2 or H_2O on Cu and on Cu_2O surfaces.

4.6 Conclusions

The formation of copper oxide film under RTSP oxidation (i.e. the change in thickness and composition of the oxide over time) on two polycrystalline copper films with different crystallinity and surface morphology was studied using reflectometry and ellipsometry (RE) measurements fitted with an EMA model. The thickness followed an inverse logarithmic growth rate, showing good agreement with what was suggested by Cabrera and Mott [34], and confirmed by different studies [2,4,18,25]. The cupric (Cu_2O) and cuprous (CuO) oxide volume fraction on the resulting copper oxides was obtained using only RE measurements fitted with an EMA model. XPS was used to validate the analysis solely based on RE. These suggest that RE measurements fitted with an EMA model is a reliable method to obtain details of the progress in oxidation of copper (i.e. thickness, growth rate and composition). Combined with AFM and XRD, the RE measurements revealed that the crystalline characteristics and surface morphology of as-deposited copper films primarily determine the thickness and composition of the resulting copper oxide films. Explicit control on the initial characteristics of as-deposited copper films

would allow us to actively design the oxidation to obtain a desired copper oxide film in terms of its thickness and R_{CuO} ratio required for a specific device.

4.7 References

(1) Gattinoni, C.; Michaelides, A. Atomistic Details of Oxide Surfaces and Surface Oxidation: The Example of Copper and Its Oxides. *Surf. Sci. Rep.* **2015**, *70* (3), 424–447 Doi: 10.1016/J.Surfrep.2015.07.001.

(2) Platzman, I.; Brener, R.; Haick, H.; Tannenbaum, R. Oxidation of Polycrystalline Copper Thin Films at Ambient Conditions. *J. Phys. Chem. C* **2008**, *112* (4), 1101–1108 Doi: 10.1021/Jp076981k.

(3) Keil, P.; Lützenkirchen-Hecht, D.; Frahm, R. Investigation of Room Temperature Oxidation of Cu in Air by Yoneda-XAFS. *Aip Conf. Proc.* **2007**, *882*, 490–492 Doi: 10.1063/1.2644569.

(4) Suzuki, S.; Ishikawa, Y.; Isshiki, M.; Waseda, Y. Suzuki_1997 Native Oxide Layers Formed on the Surface of Ultra High Purity Iron and Copper Investigated by Angle Resolved XPS. *Materials Transactions-Jim*. 1997, Pp 1004–1009.

(5) Zuo, Z.; Li, J.; Han, P.; Huang, W. XPS and DFT Studies on the Autoxidation Process of Cu Sheet at Room Temperature. *J. Phys. Chem. C* **2014**, 140820142744004 Doi: 10.1021/Jp504977p.

(6) Tahir, D.; Tougaard, S. Electronic and Optical Properties Of Cu, CuO And Cu2O Studied by Electron Spectroscopy. *J. Phys. Condens. Matter* **2012**, *24* (17), 175002 Doi: 10.1088/0953-8984/24/17/175002.

(7) Shanid, N. A. M.; Khadar, M. A. Evolution of Nanostructure, Phase Transition and Band Gap Tailoring in Oxidized Cu Thin Films. *Thin Solid Films* **2008**, *516* (18), 6245–6252 Doi: 10.1016/J.Tsf.2007.11.119.

(8) Sankaranarayanan, S. K. R. S.; Kaxiras, E.; Ramanathan, S. Atomistic Simulation of Field Enhanced Oxidation of Al (100) Beyond the Mott Potential. *Phys. Rev. Lett.* **2009**, *102* (9) Doi: 10.1103/Physrevlett.102.095504.

(9) Zoolfakar, A. S.; Rani, R. A.; Morfa, A. J.; O'mullane, A. P.; Kalantar-Zadeh, K. Nanostructured Copper Oxide Semiconductors: A Perspective on Materials, Synthesis Methods and Applications. *J. Mater. Chem. C* **2014**, *2* (27), 5247 Doi: 10.1039/C4tc00345d.

(10) Prasad, R.; Singh, P. A Novel Route of Single Step Reactive Calcination of Copper Salts Far Below Their Decomposition Temperatures for Synthesis of Highly Active Catalysts. *Catal. Sci. Technol.* **2013**, No. 1, 3326–3334 Doi: 10.1039/C3cy00626c.

(11) Yin, M.; Wu, C.-K.; Lou, Y.; Burda, C.; Koberstein, J. T.; Zhu, Y.; O'brien, S. Copper Oxide Nanocrystals. *J. Am. Chem. Soc.* **2005**, *127* (26), 9506–9511 Doi: 10.1021/Ja050006u.

(12) Dong, R.; Lee, D. S.; Xiang, W. F.; Oh, S. J.; Seong, D. J.; Heo, S. H.; Choi, H. J.; Kwon, M. J.; Seo, S. N.; Pyun, M. B.; Et Al. Reproducible Hysteresis and Resistive Switching in Metal-CuxO-Metal Heterostructures. *Appl. Phys. Lett.* **2007**, *90* (4), 042107 Doi: 10.1063/1.2436720.

(13) Yang, W. Y.; Kim, W. G.; Rhee, S. W. Radio Frequency Sputter Deposition of Single Phase Cuprous Oxide Using Cu2O as a Target Material and Its Resistive Switching Properties. *Thin Solid Films* **2008**, *517* (2), 967–971 Doi:

10.1016/J.Tsf.2008.08.184.

(14) Wang, S.-Y.; Huang, C.-W.; Lee, D.-Y.; Tseng, T.-Y.; Chang, T.-C. Multilevel Resistive Switching in Ti/CuXO/Pt Memory Devices. *J. Appl. Phys. Appl. Phys* **2010**, *108* (102), 114110–194101 Doi: 10.1063/1.2802990.

(15) Jun-Bo, G.; Wei-Le, D.; Ru-Cheng, D. Thickness Dependence of the Optical Constants of Oxidized Copper Thin Films Based on Ellipsometry and Transmittance ∗. *Chinese Phys. B* **2014**, *23* (8), 1–5 Doi: 10.1088/1674-1056/23/8/087802.

(16) Iijima, J.; Lim, J. W.; Hong, S. H.; Suzuki, S.; Mimura, K.; Isshiki, M. Native Oxidation of Ultra High Purity Cu Bulk and Thin Films. *Appl. Surf. Sci.* **2006**, *253* (5), 2825–2829 Doi: 10.1016/J.Apsusc.2006.05.063.

(17) Young, F. W.; Cathcart, J. V.; Gwathmey, A. T. The Rates of Oxidation of Several Faces of a Single Crystal of Copper as Determined with Elliptically Polarized Light. *Acta Metall.* **1956**, *4* (2), 145–152 Doi: 10.1016/0001-6160(56)90132-8.

(18) O'reilly, M.; Jiang, X.; Beechinor, J. T.; Lynch, S.; Dheasuna, C. N.; Patterson, J. C.; Crean, G. M. Investigation of the Oxidation Behaviour of Thin Film and Bulk Copper. *Appl. Surf. Sci.* **1995**, *91* (1-4), 152–156 Doi: 10.1016/0169-4332(95)00111-5.

(19) Ramanandan, G. K. P.; Ramakrishnan, G.; Planken, P. C. M. Oxidation Kinetics of Nanoscale Copper Films Studied by Terahertz Transmission Spectroscopy. *J. Appl. Phys.* **2012**, *111* (12), 1–6 Doi: 10.1063/1.4729808.

(20) Subramaniyan, A.; Perkins, J. D.; O'hayre, R. P.; Lany, S.; Stevanovic, V.; Ginley, D. S.; Zakutayev, A. Non-Equilibrium Deposition of Phase Pure Cu2O Thin Films at Reduced Growth Temperature. *Apl Mater.* **2014**, *2* (2) Doi: 10.1063/1.4865457.

(21) Apen, E. X-Ray Photoelectron Spectroscopy Characterization of the Oxidation of Electroplated and Sputter Deposited Copper Surfaces. *J. Vac. Sci. Technol. A Vacuum, Surfaces, Film.* **1998**, *16* (3), 1227 Doi: 10.1116/1.581264.

(22) Suzuki, S.; Ishikawa, Y.; Isshiki, M.; Waseda, Y. Native Oxide Layers Formed on the Surface of Ultra High-Purity Iron and Copper Investigated by Angle Resolved XPS. *Materials Transactions-Jim*. 1997, Pp 1004–1009.

(23) Tahir, D.; Tougaard, S. Electronic and Optical Properties of Cu, CuO and Cu2O Studied by Electron Spectroscopy. *J. Phys. Condens. Matter* **2012**, *24* (17), 175002 Doi: 10.1088/0953-8984/24/17/175002.

(24) Chawla, S. K.; Rickett, B. I.; Sankarraman, N.; Payer, J. H. An X-Ray Photo-Electron Spectroscopic Investigation of the Air-Formed Film on Copper. *Corros. Sci.* **1992**, *33* (10), 1617–1631.

(25) Timalsina, Y. P.; Washington, M.; Wang, G.-C.; Lu, T.-M. Slow Oxidation Kinetics in an Epitaxial Copper(100) Film. *Appl. Surf. Sci.* **2016**, *363* (2016), 209–216 Doi: 10.1016/J.Apsusc.2015.12.003.

(26) Clarke, E. G.; Czanderna, A. W. Optical Transmittance and Microgravimetric Studies of the Oxidation of (100) Siingle Crystal Films on Copper. *Surf. Sci.* **1975**, *49*, 529–536 Doi: 10.1017/Cbo9781107415324.004.

(27) Palik, E. D. *Handbook Of Optical Constants Of Solids, Vol. 3*; Academic Press,

1998.

(28) Van Wijk, R.; Gijzeman, O. L. J.; Geus, J. W. Ellipsometric Studies of the Oxidation Kinetics of Cu Particles Supported on Oxidised Si(100). *Appl. Surf. Sci.* **1996**, *93* (3), 237–245 Doi: 10.1016/0169-4332(95)00338-X.

(29) Strukov, D. B.; Snider, G. S.; Stewart, D. R.; Williams, R. S. The Missing Memristor Found. *Nature* **2008**, *453* (May), 80–83 Doi: 10.1038/Nature08166.

(30) Platzman, I.; Saguy, C.; Brener, R.; Tannenbaum, R.; Haick, H. Formation of Ultrasmooth and Highly Stable Copper Surfaces Through Annealing and Self-Assembly of Organic Monolayers. *Langmuir* **2010**, *26* (1), 191–201 Doi: 10.1021/La902006v.

(31) Landau, L.; Bell, J.; Kearsley, M.; Pitaevskii, L.; Lifshitz, E.; Sykes, J. *Electrodynamics of Continuous Media*; 1984.

(32) Spanier, J.; Herman, I. Use of Hybrid Phenomenological and Statistical Effective-Medium Theories of Dielectric Functions to Model the Infrared Reflectance of Porous Sic Films. *Phys. Rev. B* **2000**, *61* (15), 10437–10450 Doi: 10.1103/Physrevb.61.10437.

(33) Theiss, W. The Use of Effective Medium Theories in Optical Spectroscopy. *Adv. Solid State Phys. 33* **1993**, *33*, 149–176.

(34) Cabrera, N.; Mott, N. F. Theory of the Oxidation of Metals. *Reports Prog. Phys.* **1949**, *12* (1), 163 Doi: 10.1017/Cbo9781107415324.004.

(35) Gattinoni, C.; Michaelides, A. Atomistic Details of Oxide Surfaces and Surface Oxidation: The Example of Copper and Its Oxides. *Surf. Sci. Rep.* **2015**, *70* (3), 424–447 Doi: 10.1016/J.Surfrep.2015.07.001.

(36) Chase, M. W. Nist-Janaf Thermichemical Tables for Copper. *J. Phys. Chem. Ref. Data Monogr. 9* **1998**, 1005–1027.

(37) Scherrer, P. Estimation of the Size and Internal Structure of Colloidal Particles by Means of Röntgen. *Nachr. Ges. Wiss. Göttingen* **1918**, *2*, 96–100.

(38) Zhou, G.; Wang, L.; Yang, J. C. Effects of Surface Topology on the Formation of Oxide Islands on Cu Surfaces. *J. Appl. Phys.* **2005**, *97* (6) Doi: 10.1063/1.1861147.

(39) Lim, J. W.; Iijima, J.; Zhu, Y.; Yoo, J. H.; Choi, G. S.; Mimura, K.; Isshiki, M. Nanoscale Investigation of Long-Term Native Oxidation of Cu Films. *Thin Solid Films* **2008**, *516* (12), 4040–4046 Doi: 10.1016/J.Tsf.2007.12.159.

5 Conclusions and future directions

5.1 Conclusions

Throughout this thesis, we have explored several different applications where oxidation kinetics play a key role for device fabrication, degradation and even as a characterization technique for moisture barriers. The combination of design, fabrication and characterization was used to successfully create structures for specific applications such as antireflective coatings, waveguides, mode size converters, memristors and selectors. Conclusions and future directions from every chapter are presented in the following paragraphs. After that, general future directions for oxidation kinetics are discussed.

5.2 Chapter 2

Multi-cation oxides for solar energy applications were designed, fabricated and characterized for the S2F project. Funding for the S2F project ended before completion of the AOC device; however, we learned several concepts that could be applied in the future.

Continuously graded antireflection coatings were designed to minimize reflections for a large range of wavelengths and angles in the solar spectrum; fabrication was demonstrated, but it was stopped before a set of samples large enough was characterized to draw any substantial conclusions. Depositing ARCs with multi-cation oxides and/or fluorides could achieve very low reflection and be used for applications where a high index is present. Semiconductor lasers suffer from loss between the gain medium and its surrounding medium,[1] OLEDs present high reflectivity hindering external quantum efficiency between the transparent conductive electrode, the substrate and the active layer present in an OLED structure.[2] All these and many other applications would benefit from continuously graded ARCs. Deposition with sputtering or atomic layer deposition is possible with monolayer precision.

Multi-cation oxides were deposited using a pDC magnetron sputtering system with RF substrate bias. Titanium hafnium oxide alloys showed an increased refractive index and a decreased grain size when RF substrate bias power was used. After the enhancement in optical properties and density with RF substrate bias was demonstrated, multi-cation oxides deposited using this same technique were then studied as moisture barriers. Aluminum titanium oxide alloys were deposited with a range of molar fractions, from aluminum oxide, through different $Al_xTi_{1-x}O_y$ combinations, showing how intermediate molar fractions were better moisture barriers that their single-cation counterparts. From these studies, it appears that the combination of a deposition system producing high ion-to-neutral flux and multiple cations leads to more dense, lower loss dielectrics that can be used for optical and optoelectronic applications in need of materials in this refractive index range.

Low loss waveguides in the visible and near-infrared (VNIR) spectrum could enable innovative technologies to be used at the VNIR range, since traditional dielectrics used for telecommunications wavelengths present high transmission loss when the wavelength decreases. The combination of pDC magnetron sputtering target power and RF substrate bias reduced loss without annealing, increasing the integration capabilities of dielectric waveguides in organic substrates or silicon photonics.[3,4] Furthermore, these waveguides were deposited in transition-mode sputtering, with deposition rates as high as 1.28 nm/s. AlOx waveguides with n=1.6 were fabricated with α=1.55 dB/cm without annealing. New oxides such as HfO_x or multi-cation oxides such as $AlTi_xO_y$ or $SiTi_xO_y$ can be deposited with a desired refractive index to match the refractive index of specific applications.

5.3 Chapter 3

In this chapter, it was shown how a combination of simulations and fabrication led to a functional device using oxidation kinetics. A selector-memristor structure showed a nonlinear memristive I-V behavior after electroforming. After successfully developing a

self-aligned selector-memristor structure we realized that the electroforming via Joule heating step requires further investigation. Time-dependent simulations are now studied to understand this process better. Once this is understood and all the physical parameters that we know of are introduced, the materials' properties can be tuned to improve this process. Anisotropic materials with different axis-dependent thermal and electrical properties can be used to reduce device scale and further optimize nonlinearity and memristive the I-V behavior. Moreover, the demonstration of this devices remains a laboratory experiment; there is much work to be done until the repeatability of this process becomes consistent enough to be used in an industrial environment.

5.4 Chapter 4

Chapter 4 is devoted to a classical mechanism, oxidation of room temperature and pressure of copper. Reflectometry-ellipsometry (RE) is used in conjunction with an effective medium approximation (EMA) model for data fitting. As a result, thickness and phase composition can be routinely monitored over large areas for a period of 253 days. Results show how copper oxide follows an inverse-logarithmic growth rate, and how Cu_2O seems to form first, and then CuO grows on top of Cu_2O afterwards, agreeing with thermodynamic assessments. The initial thickness, growth rate and phase composition appear to be related to grain size and surface roughness of the initial thin-film copper, deposited by e-beam evaporation or sputtering. Following this experimental study, MD simulations of this material system would extract which parameters affect oxide growth. A parametric study could predict the optimal surface and grain size copper to slow down copper oxide growth (which would benefit copper oxide interconnects) or to control the oxide such that a precise thickness and Cu_2O/CuO ratio could be achieved just by letting copper sit in an ambient environment. The thickness that can be achieved for this process is very limited (~10 nm), so fabricating thick copper oxide structures (such as solar cells) is out of the scope of this work. Copper oxide presents ionic growth, so a

fundamental study regarding this process could lead to a better understanding of volatile conductive bridge (VCB) formation for nonlinear I-V devices.

5.5 Future directions

For future directions, exploration of computational/theoretical models seem fitting to further understand the fundamental physics behind oxidation kinetics. Given the continuously changing states of the material(s) under study, numerical simulations can be a useful tool. Molecular dynamics (MD) are currently being studied to understand copper oxidation following De Souzas's work.[5] MD combined with Monte Carlo (MC) could provide further insights into how pDC magnetron sputtering combined with substrate bias interact during deposition. For longer times (ms) and larger structures (10-100s of nm), MD and MC are too computationally costly to be used. Thus, regarding device fabrication using oxidation kinetics, the NECTAR group is currently running time-dependent partial derivative equation (PDE) studies to understand and optimize electroforming of nonlinear I-V devices. In materials science and engineering, understanding a device from the atomic scale all the way up to the electrical and optical output will further optimize existing devices and enable the fabrication of novel structures for energy and bioengineering applications.

5.6 References

(1) Eisenstein, G.; Stulz, L. W.; Van Uitert, L. G. Antireflection coatings on semiconductor laser facets using sputtered lead silicate glass. *J. Light. Technol.* **1986**, *LT-4* (9), 1373–1375.

(2) Saxena, K.; Mehta, D. S.; Rai, V. K.; Srivastava, R.; Chauhan, G.; Kamalasanan, M. N. Implementation of anti-reflection coating to enhance light out-coupling in organic light-emitting devices. *J. Lumin.* **2008**, *128* (3), 525–530 DOI: 10.1016/j.jlumin.2007.09.028.

(3) Briggs, R. M.; Grandidier, J.; Burgos, S. P.; Feigenbaum, E.; Atwater, H. A. Efficient coupling between dielectric-loaded plasmonic and silicon photonic waveguides. *Nano Lett.* **2010**, *10* (12), 4851–4857 DOI: 10.1021/nl1024529.

(4) Rinne, S. A.; García-Santamaría, F.; Braun, P. V. Embedded cavities and waveguides in three-dimensional silicon photonic crystals. *Nat. Photonics* **2008**, *2* (1), 52–56 DOI: 10.1038/nphoton.2007.252.

(5) Genreith-Schriever, A. R.; De Souza, R. A. Field-enhanced ion transport in solids: Reexamination with molecular dynamics simulations. *Phys. Rev. B* **2016**, *94* (22), 224304 DOI: 10.1103/PhysRevB.94.224304.